

The Physics of Spatially Twisted Nematic Liquid Crystals

by

Alicia Sit

Thesis submitted in partial fulfillment
of the requirements for
Doctorate in Philosophy degree in Physics

Department of Physics
University of Ottawa
Ottawa, Canada

© Alicia Sit, Ottawa, Canada, 2023

Abstract

When nematic liquid crystals are placed between parallel glass plates with differing alignment directions, the bulk will twist in order to match the boundary conditions. This phenomenon of a twisted cell has been used extensively for the development of everyday liquid-crystal displays. However, there has been limited study of the twisted cell beyond the 90° twist case. In this thesis, I explore the behaviour of inhomogeneous liquid-crystal devices where the front and back alignment layers are uniquely and spatially patterned. This creates a non-symmetric device which can act on light differently depending on the orientation of the device and an externally applied voltage. The effect on the polarization of light is theoretically modelled using Jones matrices, and elastic continuum theory is employed to fully understand how the twist and tilt distributions of the liquid crystals change with field strength. Different pattern configurations were fabricated, tested, and characterized, revealing the complex behaviour that occurs with an applied electric field. Liquid-crystal devices provide a bespoke way of tailoring the spatial distribution of light and photons. A set of quantum key distribution experiments through underwater channels, leveraging these devices to encode information on structured photons, is also presented.

Acknowledgements

I wish to thank my supervisor, Prof. Ebrahim Karimi, for his continuous support throughout the course of my PhD degree. I acknowledge the financial support of the Canada Research Chairs (CRC) program, and of the Natural Sciences and Engineering Research Council of Canada (NSERC). I would also like to thank the entire Structured Quantum Optics (SQO) group; in particular, a huge thank you goes to Francesco Di Colandrea for his timely help of coding the genetic algorithms, without which this thesis would be an incomplete story. While not included in this thesis, I am thankful to Prof. Ebrahim Karimi and Prof. Jeff Lundeen, as well as my collaborators from NRC (Frédéric Bouchard, Khabat Heshami, Denis Guay, Duncan England, Phil Bustard, Ben Sussman), for giving me the opportunity to get the JCEP lab at NRC up and operational and being its lab ‘manager’. Last but not least, I would like to thank my parents, family, and husband for their generosity and support from the beginning.

This PhD was carried out during what can only be described as unprecedented and interesting times. For about a year starting in the spring of 2020, there was little to no lab access due to the pandemic. In this time, I could not further any progress in my experimental quantum cryptography projects, and so eventually, I pivoted to exploring the theory of twisted nematic liquid crystals. I finally returned back to the lab environment in the fall of 2021, taking up the responsibility of managing the JCEP lab at NRC. I was also able to start fabricating and testing various structured twisted liquid-crystal elements—only to be puzzled by the results I was getting and having to do a deep dive into the intriguing physics of liquid crystals.

While the past four years are certainly not how I had envisioned my PhD to go—especially with the added struggle of personal and medical issues—it’s the one I got. “Make the best use of what is in your power, and take the rest as it happens,” Epictetus, *Discourses*.

To Morgan, my guiding light through trying times,
and to Zerida, my ever-present feline companion.

Table of Contents

Abstract	ii
Acknowledgements	iii
List of Publications	viii
Statement of Originality and Contributions	x
List of Figures	x
1 Introduction	1
1.1 Overview	1
1.2 Transverse spatial modes	2
1.2.1 Paraxial wave equation	2
1.2.2 Generation techniques	6
1.3 Polarization	8
1.3.1 Jones calculus	8
1.3.2 Poincaré sphere	10
1.4 Structured light	11

2	Liquid Crystals	13
2.1	A brief history	13
2.2	Mesophases	15
2.3	Physical and Optical properties	17
2.3.1	Bulk and boundary effects	17
2.3.2	Birefringence	18
2.4	Pancharatnam–Berry optical elements	21
3	Non-Symmetric Inhomogeneous Liquid-Crystal Devices	23
3.1	Twisted nematics	23
3.2	Dual-plates	27
3.3	Fabrication and characterization	29
3.4	Experimental results and discussion	32
4	Electric field-induced effects	40
4.1	Elastic continuum theory	40
4.1.1	Fundamental equation	41
4.1.2	Fréedericksz transition	43
4.2	Twisted nematic cell	46
4.2.1	Field-free case	46
4.2.2	Field-induced effects	47
4.3	Numerical approach	50
4.3.1	Genetic algorithm	50
4.3.2	Jones matrix method	54
4.4	Results and discussion	54
4.4.1	β – θ_m	54
4.4.2	Tilt and twist distributions	58
4.4.3	Polarization effects	61

5 Underwater Quantum Cryptography	65
5.1 Quantum key distribution	65
5.2 Underwater channel	69
5.2.1 Optical properties	69
5.2.2 Turbulence	70
5.3 Publication: Characterization of an underwater channel for quantum communications in the Ottawa River	75
5.4 Publication: Investigation of underwater quantum channels in a 30 meter flume tank using structured photons	84
6 Conclusion	92
References	94
APPENDICES	102
A Experimental Data	103
B Elastic continuum theory	110
B.1 Derivation of free-energy density distortion terms	110

List of Publications

PhD

1. **A. Sit**, F. Di Colandrea, A. D’Errico, E. Karimi, A genetic algorithm for the response of twisted nematic liquid crystals to an applied field. *in preparation* (2023).
2. **A. Sit**, F. Di Colandrea, A. D’Errico, E. Karimi, Non-symmetric inhomogeneous liquid-crystal devices. *in preparation* (2023).
3. M. F. Ferrer-Garcia, A. D’Errico, H. Larocque, **A. Sit**, E. Karimi, “Polychromatic electric field knots,” *Physical Review Research* **3**, 033226 (2021).
4. **A. Sit**, F. Hufnagel, E. Karimi, “Chapter 6: Quantum cryptography with structured photons,” in *Nanophotonics, Structured Light for Optical Communication*, Elsevier, 139–176 (2021).
5. F. Bouchard, **A. Sit**, Y. Zhang, R. Fickler, F. M. Miatto, Y. Yao, F. Sciarrino, E. Karimi, “Two-photon interference: the Hong–Ou–Mandel effect,” *Reports on Progress in Physics* **84**, 012402 (2020).
6. F. Hufnagel, **A. Sit**, F. Bouchard, Y. Zhang, D. England, K. Heshami, B. J. Sussman, E. Karimi, “Investigation of underwater quantum channel in a 30-meter flume tank using structured photons,” *New Journal of Physics* **22**, 093074 (2020).
7. F. Hufnagel, **A. Sit**, F. Grenapin, F. Bouchard, K. Heshami, D. Englang, Y. Zhang, B. J. Sussman, R. W. Boyd, G. Leuchs, E. Karimi, “Characterization of an underwater channel for quantum communications in the Ottawa River,” *Optics Express* **27**, 26346–26354 (2019).

MSc

8. F. Bouchard, F. Hufnagel, D. Koutný, A. Abbas, **A. Sit**, K. Heshami, R. Fickler, and E. Karimi, “Quantum process tomography of a high-dimensional quantum communication channel,” *Quantum* **3**, 138 (2019).
9. F. Nejdassattari, Y. Zhang, F. Bouchard, H. Larocque, **A. Sit**, E. Cohen, R. Fickler, and E. Karimi, “Experimental realization of wave-packet dynamics in cyclic quantum walks,” *Optica* **6**, 174 (2019).
10. Y. Zhang, **A. Sit**, F. Bouchard, H. Larocque, F. Grenapin, E. Cohen, A. C. Elitzur, J. L. Harden, R. W. Boyd, and E. Karimi, “Interaction-Free Ghost-Imaging of Structured Objects,” *Optics Express* **27**, 2212 (2019).
11. **A. Sit**, R. Fickler, F. Alsaïari, F. Bouchard, H. Larocque, P. Gregg, L. Yan, R. W. Boyd, S. Ramachandran, and E. Karimi, “Quantum cryptography with structured photons through a vortex fiber,” *Optics Letters* **43**, 4108 (2018).
12. F. Bouchard, **A. Sit**, F. Hufnagel, A. Abbas, Y. Zhang, K. Heshami, R. Fickler, C. Marquardt, G. Leuchs, and E. Karimi, “Quantum cryptography with twisted photons through an outdoor underwater channel,” *Optics Express* **26**, 22563 (2018).
13. F. Bouchard, **A. Sit**, K. Heshami, R. Fickler, and E. Karimi, “Round-Robin Differential Phase-Shift Quantum Key Distribution with Twisted Photons,” *Physical Review A* **98**, 010301(R) (2018).
14. M. T. Runyon, C. H. Nacke, **A. Sit**, M. Granados-Baez, L. Giner, and J. S. Lundeen, “Implementation of nearly arbitrary spatially varying polarization transformations: an in-principle lossless approach using spatial light modulators,” *Applied Optics* **57**, 5769 (2018).
15. **A. Sit**, F. Bouchard, R. Fickler, J. Gagnon-Bischoff, H. Larocque, K. Heshami, D. Elser, C. Peuntinger, K. Günther, B. Heim, C. Marquardt, G. Leuchs, R. W. Boyd, and E. Karimi, “High-dimensional intracity quantum cryptography with structured photons,” *Optica* **4**, 1006 (2017).

Statement of Originality and Contributions

To the best of her knowledge, the author states that the work described in this PhD thesis constitutes original research in the field of physics. Below, we provide the collaborative contributions of each participant for every chapter.

E. Karimi initiated the work of Chapter 3. A. Sit analyzed and extended the theory. A. Sit and A. D’Errico fabricated the liquid-crystal devices. A. Sit experimentally characterized the samples, and compared the results to the theory.

A. Sit initiated the work of Chapter 4. F. Di Colandrea developed the genetic algorithm for numerically calculating the liquid crystal twist and tilt distributions. A. Sit numerically calculated the tilt and twist distributions for a wide range of initial conditions using the genetic algorithm, as well as analyzing its effect on polarized light. A. Sit and A. D’Errico fabricated the liquid-crystal devices. A. Sit experimentally characterized the samples, and compared the results to theory.

E. Karimi initiated the work of Chapter 5. For [1], A. Sit, F. Hufnagel, and F. Grenapin performed the experiment. F. Hufnagel, A. Sit, and F. Bouchard wrote the paper. A. Sit analyzed the data for the polarization probability-of-detection matrix. For [2], K. Heshami, D. England, and B. J. Sussman provided access to the NRC’s steel wave flume research facility. A. Sit organized and led the day-to-day operations of the experiment. A. Sit, F. Hufnagel, and F. Bouchard performed the experiment. F. Hufnagel and F. Bouchard analyzed the data. F. Hufnagel, F. Bouchard, and A. Sit wrote the paper.

List of Figures

1.1	Laguerre–Gauss modes. Phase profiles modulated by the intensity profiles of LG modes with $\ell = -2, -1, 0, 1, 2$ and $p = 0, 1, 2$	5
1.2	Polarization representations. a. Convention used for the six cardinal polarizations from the point of view of the source. b. Depiction of a general polarization state on the Poincaré sphere given its Stokes vector $\mathbf{S}(\phi, \theta)$	9
1.3	Vector vortex beams. a. Radially polarized light. b. Azimuthally polarized light. c. Vector vortex mode with $ \ell = 2$. d. Vector vortex mode with $ \ell = 3$	12
2.1	Liquid crystal mesophases. a. Nematics with average director direction $\hat{\mathbf{n}}$. b. Smectics, specifically type A, with liquid layers of spacing d . c. Columnar phases with tubes of liquid along structure lattice vectors $\{\hat{1}, \hat{2}, \hat{3}\}$	15
2.2	Bulk distortions. When nematic liquid crystals are placed between two glass plates with a particular alignment direction (denoted by the arrows), they can exhibit a. splay, b. twist, and c. bend distortions to conform with the boundary conditions.	18
2.3	Refractive index ellipsoid of uniaxial crystal. a. For light propagating at an angle θ , the eigenpolarizations will be given by the blue vectors. b. The effective refractive index n_θ experienced by one of the eigenpolarizations.	20
2.4	q-plate patterns. The optical axis distributions for topological charges a. $q = \pm 1/2$, b. $q = \pm 1$, and c. $q = \pm 2$. The topological charge is determined by the number of times (half-integer or integer) that the local axis turns about the center singularity, as shown by going around the red circle. NB: Line discontinuities are plotting artifacts; only the center singularities have an undefined axis.	22

3.1	Twisted nematic liquid-crystal cell. a. Illustration of liquid crystals twisting between two glass plates, uniformly aligned at 0° and α for the front and back layers, respectively, spaced apart by a distance of d . The action of this configuration is shown on the Poincaré Sphere given a horizontally polarized input state (black dot) for varying twist angles α between $-\pi/2$ and $+\pi/2$, with a birefringence of b. $\Gamma = \pi$, and c. $\Gamma = 1001\pi$ in the adiabatic following regime.	25
3.2	Example of multi-q-plate. a. Disclination patterns for the front ($\Phi_f(\varphi) = \varphi$) and back ($\Phi_b(\varphi) = 3\varphi$) alignment layers. b. The resulting twist distribution $\alpha(\varphi) = 2\varphi$. c. The induced global phase distribution with phase jumps located where the twist distribution could be either $\pm\pi/2$	27
3.3	Experimental setups a. Setup to pattern the glass plates for fabricating liquid-crystal devices. The inset shows the cross-section of the constructed LC cell b. Setup to characterize the fabricated samples. DMD = digital micromirror device, PBS = polarizing beamsplitter, FG = function generator.	30
3.4	Fabricated samples. False colour images of a. discretized DP(0,1/2), and b. DP(1,2) between crossed polarizers under a microscope illuminated with white light. The topological patterns on each glass plate is also shown. Note that the $q = 1/2$ pattern is discretized into 16 slices for the patterning process.	32
3.5	Polarization tomography of discretized DP(0,1/2). a. Alignment patterns on the front and back glass plates. b. Example of recorded intensity distribution for an input of \mathbf{A}_H projected on \mathbf{A}_V . The white lines denote the border between each slice, and the small blue square is an example area over which the output polarization is averaged. c. Reconstructed output polarization ellipse distributions for the six cardinal input polarizations. Green = right-hand elliptical ($S_3 > 0$); red = left-hand elliptical ($S_3 < 0$); black = linear ($S_0 = 0$).	33
3.6	Stokes vectors of discretized DP(0,1/2). a. Alignment patterns on the front and back glass plates. b. Reconstructed average Stokes vectors in each of the 16 slices (coloured points) for the cardinal input states (black points), and theoretical fit (line) using the TNLC Jones matrix with $\Gamma_{\text{fit}} = 51.7$. Percentages are the average state overlap with all 16 average Stokes vectors.	35

3.7	Polarization tomography of discretized DP(1/2,0). a. Alignment patterns on the front and back glass plates. b. Example of recorded intensity distribution for an input of \mathbf{A}_H projected on \mathbf{A}_V . The white lines denote the border between each slice, and the small blue square is an example area over which the output polarization is averaged. c. Reconstructed output polarization ellipse distributions for the six cardinal input polarizations. Green = right-hand elliptical ($S_3 > 0$); red = left-hand elliptical ($S_3 < 0$); black = linear ($S_0 = 0$).	36
3.8	Stokes vectors of discretized DP(1/2,0). a. Alignment patterns on the front and back glass plates. b. Reconstructed average Stokes vectors in each of the 16 slices (coloured points) for the cardinal input states (black points), and theoretical fit (line) using the TNLC Jones matrix with $\Gamma_{\text{fit}} = 51.7$. Percentages are the average state overlap with all 16 average Stokes vectors.	37
3.9	Polarization tomography of DP(1,2). a. Reconstructed output polarization ellipse distributions for the six cardinal input polarizations. b. Theoretically predicted polarization distributions with $\Gamma_{\text{fit}} = 52.4$. Green = right-hand elliptical ($S_3 > 0$); red = left-hand elliptical ($S_3 < 0$); black = linear ($S_0 = 0$).	38
3.10	Polarization tomography of DP(2,1). a. Reconstructed output polarization ellipse distributions for the six cardinal input polarizations. b. Theoretically predicted polarization distributions with $\Gamma_{\text{fit}} = 52.4$. Green = right-hand elliptical ($S_3 > 0$); red = left-hand elliptical ($S_3 < 0$); black = linear ($S_0 = 0$).	39
4.1	Fréedericksz transition. a. Sample patterning and field configurations for electric-field-induced i. splay ii. twist, and iii. bend Fréedericksz transitions. b. Plot of the maximum tilt angle $\theta_m(E/E_T)$ as a function of field strength. c. Tilt distributions $\theta(z)$ for reduced voltage $V_r \leq 1$, $V_r = 1.2, 2, 4$.	44
4.2	Threshold field conditions for 6CHBT. As a function of the total twist angle ϕ_m , a. the threshold voltage V_T , and b. the integration constant at threshold β_T .	50
4.3	Integration constant $\beta(\phi_m, V)$. The dots correspond to the numerically calculated values for maximum twist angles $\phi_m = 90^\circ, 67.5^\circ, 45^\circ, 22.5^\circ, 0^\circ$. The vertical gradient line is the analytical $\beta_T(\phi_m)$ values from Eq. 4.33, whereas the cascading solid-coloured lines are the lines of best using Eq. 4.42.	55

4.4	Maximum tilt angle $\theta_m(\phi_m, V)$. The dots are the numerically calculated values for maximum twist angles $\phi_m = 90^\circ, 67.5^\circ, 45^\circ, 22.5^\circ, 0^\circ$. In the bottom inset, the gradient line is the theoretical $V_T(\phi_m)$ from Eq. 4.32. The dashed lines in both insets merely connect the dots for visual ease.	56
4.5	Fits for $\theta_m(\phi_m, V)$. Using the ansatz in Eq. (4.43), fits are produced using the $\phi_m = 0^\circ, 45^\circ, 90^\circ$ data sets. Each fit is then used to produce the $\theta_m(\phi_m, V)$ curves for other ϕ_m values, as shown in each subplot.	57
4.6	GA results for $\phi_m = 45^\circ$. a. Twist and b. tilt distributions for $V_{pp} = 4, 6, 8, 12$ V. c. Phase retardation distribution $\Gamma(z)$ computed using $L = 35 \mu\text{m}$	58
4.7	GA results for 1.2 V. a. Twist, b. tilt, and c phase retardation distributions for $\phi_m = 0^\circ, 22.5^\circ, 45^\circ, 67.5^\circ, 90^\circ$ with $L = 35 \mu\text{m}$	59
4.8	GA results for different maximum twist angles. a. $V = 1.061$ V, b. $V = 2.0$ V, c. $V = 4.0$ V.	60
4.9	Comparison of output states generated via the approximated tilt and twist distributions (colored lines) based on $\phi(45^\circ, V, z)$ and $\theta(45^\circ, V, z)$ versus the numerically calculated distributions for each ϕ_m (colored dots). A horizontally polarized input was used.	61
4.10	Externally applied voltage on DP(0,1/2). a. Reconstructed polarization distributions from a horizontally polarized input for voltages of $V_{pp} = 3.00, 6.00, 8.00,$ and 12.00 V. b. The experimental data (dots) are the output Stokes vectors. Numerical approximations (gradiated solid line) were obtained by scaling the twist distribution for $\phi_m = 45^\circ$	62
4.11	Externally applied voltage on DP(1/2,0). a. Reconstructed polarization distributions from a horizontally polarized input for voltages of $V_{pp} = 3, 6, 8,$ and 12 V. b. The experimental data (dots); numerical approximations (gradiated solid line) were obtained by scaling the twist distribution for $\phi_m = 45^\circ$. c. Numerical (experimental) results at $V_{pp} = 3$ V (3.5 V), 5.5 V (6 V), 7.5 V (8 V), and 11.5 V (12 V).	63
5.1	BB84 secret key rate plots for $d = 2, 4, 8, 16$	68
5.2	Absorption spectrum of water in the visible regime. Source: data from [3].	69
5.3	Phase profiles of Zernike polynomials.	73

Chapter 1

Introduction

1.1 Overview

When nematic liquid crystals are placed between parallel glass plates with differing alignment directions, the bulk will twist in order to match the boundary conditions [4]. This phenomenon of a twisted nematic liquid crystal (TNLC) cell—in particular with 90° twists—has been used extensively for the development of everyday liquid-crystal displays [5–7]. With properly chosen birefringent liquid crystals and fabrication techniques, incident linearly polarized light will rotate through the cell, following the twist structure. When a sufficiently strong voltage is applied across the cell, the twist structure disappears as the liquid crystals are aligned in the field direction, negating any polarization rotation. However, there has been limited study of the twisted cell beyond the 90° -twist case for general polarization manipulation [8, 9].

On the other hand, in the context of experimental optics, spatially patterned liquid-crystal-based devices are an efficient and compact method for structuring the polarization and spatial degrees of freedom of light, but studies have been limited to symmetric elements, i.e., the front and back patterns on the alignment layers are identical. For example, q -plates—part of the general class of Pancharatnam–Berry phase optical elements (PBOE)—are such that the liquid-crystal layer is aligned to have a semi-integer topological charge of q . This allows for the coupling of spin to orbital angular momentum. q -plates have found applications in both classical and quantum optics [10], in particular STED microscopy [11], metrology [12], high-dimensional classical [13] and quantum communication [14], and quantum simulations [15]. For the case of non-symmetric spatially patterned devices, there have been only a few implementations, including polarization con-

verters which convert linear polarization into vector vortex modes [16]—a functionality still achievable via standard q -plates [17]. However, these spatially twisted elements operate with no externally applied field. Recently, there has been a work that observes the voltage-dependent behavior of non-symmetric devices patterned with different gratings [18].

This thesis aims to bridge the above gaps by investigating the behaviour of liquid crystals with the full range of possible twist angles from -90° to 90° , under the influence of various externally applied electric fields. By creating non-symmetric devices, one can selectively manipulate light based on the device orientation and external voltage application. Dual-plates (DP), as I will call them, thus promise a switch-like capability between phase distributions. The polarization of light is theoretically modeled using Jones matrices, while elastic continuum theory provides insights into the changes in the twist and tilt distributions of liquid crystals under varying field strengths. I present a numerical analysis for the modified tilt and twist distributions, obtained via genetic algorithms. Through the fabrication, testing, and characterization of different pattern configurations, we uncover the complex behaviors that emerge when an electric field is applied. This research not only contributes to the fundamental understanding of liquid-crystal devices but also explores their potential for tailoring the spatial distribution of light and photons.

The conventions and notations for the pertinent photonic degrees of freedom will be defined for consistency in the rest of this chapter. In Chapter 2, the physics of liquid crystals will be introduced, covering the basics of the different phases, optical properties, as well as the debut of liquid-crystal-based optical elements for the purpose of structuring light. Chapter 3 and Chapter 4 detail the theoretical and experimental exploration of twisted liquid-crystal devices, with the former laying out the model in a field-free system, while the latter extends this to the response due to an applied field with the help of genetic algorithms. Quantum cryptography is one use of structured light, which can be generated via liquid-crystal optics. A set of experiments exploring the feasibility of using structured photons for quantum key distribution through an underwater channel will be discussed in Chapter 5. Closing remarks and future questions to investigate will be given in Chapter 6.

1.2 Transverse spatial modes

1.2.1 Paraxial wave equation

It goes without saying that Maxwell's equations are fundamental to uniquely describing light as an electromagnetic (EM) field with field vectors \mathbf{E} and \mathbf{B} . The four rules that are

necessary and sufficient that all EM waves must obey are governed by the divergence and curl of its respective electric and magnetic fields, given here in vacuum,

$$\nabla \cdot \mathbf{E} = \frac{\rho}{\epsilon_0}, \quad (1.1)$$

$$\nabla \cdot \mathbf{B} = 0, \quad (1.2)$$

$$\nabla \times \mathbf{E} = -\frac{\partial \mathbf{B}}{\partial t}, \quad (1.3)$$

$$\nabla \times \mathbf{B} = \mu_0 \mathbf{J} + \mu_0 \epsilon_0 \frac{\partial \mathbf{E}}{\partial t}, \quad (1.4)$$

where ρ and \mathbf{J} are the charge and current densities present, respectively, which are taken to be zero in free-space; ϵ_0 and μ_0 are the permittivity and permeability of vacuum. As we see, Maxwell's equations in vacuum consist of a set of differential equations that couple the electric to magnetic field. It is extremely useful to decouple these two fields in order to gain insights into their physical nature and behaviour. For the electric field, this is simply done by taking the curl of Eq. (1.3), and substituting in Eq. (1.1) and (1.4) with $\rho = 0$, $\mathbf{J} = 0$; the magnetic field can be similarly obtained by instead starting with the curl of Eq. (1.4). Recall that we have the additional condition of transversality where \mathbf{E} and \mathbf{B} lie in a plane orthogonal to the direction of propagation, dictated by $\nabla \cdot \mathbf{E} = 0$ and $\nabla \cdot \mathbf{B} = 0$. This results in Helmholtz's wave equations,

$$\left(\nabla^2 - \mu_0 \epsilon_0 \frac{\partial^2}{\partial t^2} \right) \Psi(\mathbf{r}) = 0, \quad (1.5)$$

where $\Psi(\mathbf{r})$ is either the electric or magnetic field, and we can associate the speed with which these waves travel at to be $c = (\mu_0 \epsilon_0)^{-1/2}$, and ∇^2 is the Laplacian operator.

Traditionally, the solutions of these wave equations are given as ansatz for different symmetries, for example, Cartesian, cylindrical, elliptic-cylindrical, or spherical; we obtain, respectively, plane waves, Bessel beams, Mathieu beams, and spherical waves. While these forms mathematically represent solutions to the wave equation—corresponding to light beams with amplitude and phase profiles—their intensity is non-normalizable, resulting in beams that carry an infinite amount of energy. Obviously, such beams are not truly physical and cannot be fully generated in the lab. This is mainly due to the fact that the beam will undergo truncation due to any type of aperture, giving rise to diffraction and various propagation effects which are not present in the aforementioned solutions.

The paraxial wave equation, derived from the Helmholtz's wave equation, appropriately describes physical light beams which can be readily produced in the lab with lasers. To obtain this equation, we first make the assumption of separation of variables in spatial and

temporal coordinates such that the field is formulated as $\psi(\mathbf{r}, t) = \tilde{\psi}(\mathbf{r})e^{ikz}e^{-ikt}$. Since the deviation of the wave vector away from the optical axis is very small as is the case for collimated light beams, we can make use of the paraxial approximation, i.e., the slowly varying amplitude approximation to arrive at the paraxial wave equation,

$$\left(\nabla_{\perp}^2 + 2ik\frac{\partial}{\partial z}\right)\tilde{\psi}(\mathbf{r}) = 0, \quad (1.6)$$

∇_{\perp}^2 is the transverse Laplacian operator.

Much like Helmholtz's wave equation, the solutions to Eq. (1.6) can be determined in different symmetries to give the transverse complex amplitude $\tilde{\psi}(\mathbf{r})$. In Cartesian coordinates (x, y, z) , typically found in optical resonators, we get the Hermite–Gauss modes [19],

$$\begin{aligned} \text{HG}_{n,m}(x, y, z) &= \frac{C_{n,m}}{w(z)} \exp\left(-ik\frac{(x^2 + y^2)}{2R(z)}\right) \exp\left(-\frac{(x^2 + y^2)}{w(z)^2}\right) \times \\ &\times H_n\left(\frac{x\sqrt{2}}{w(z)}\right) H_m\left(\frac{y\sqrt{2}}{w(z)}\right) \exp(i\Phi_{nm}(z)). \end{aligned} \quad (1.7)$$

Here, n is a positive integer for the x index, and m is a positive integer for the y index; $C_{n,m}$ is the normalization constant; $w(z) = w_0(1 + (z/z_R)^2)^{1/2}$ is the beam radius with beam waist w_0 at $z = 0$, and Rayleigh range $z_R = \pi w_0^2/\lambda = k\omega_0^2/2$. The second term describes the expanding curvature of the mode with radius of curvature $R(z) = z(1 + (z/z_R)^2)$. The third, fourth, and fifth terms together give the Hermite polynomials $H_n(\cdot)$, $H_m(\cdot)$ modulated by a Gaussian that scales with distance. Finally, the sixth term is the effect of the mode-dependent Gouy phase $\Phi(z) = (n + m + 1)\arctan(z/z_R)$.

More pertinent to this thesis is the solution set in cylindrical coordinates (r, ϕ, z) , which consist of the Laguerre–Gauss (LG) modes [20],

$$\begin{aligned} \text{LG}_{\ell,p}(r, \phi, z) &= \frac{C_{\ell,p}}{w(z)} \left(\frac{r\sqrt{2}}{w(z)}\right)^{|\ell|} \exp\left(-ik\frac{r^2}{2R(z)}\right) \exp\left(-\frac{r^2}{w(z)^2}\right) \times \\ &\times L_p^{|\ell|}\left(\frac{2r^2}{w(z)^2}\right) \exp(i\Phi_{\ell p}(z)) \exp(i\ell\phi). \end{aligned} \quad (1.8)$$

Here, $C_{\ell,p} = (2p!/(\pi(p + |\ell|)!))^{1/2}$. The second term is associated with a scaling that expands upon propagation. The third and fourth terms together give the generalized Laguerre polynomials $L_p^{|\ell|}(\cdot)$ modulated by a Gaussian that scales with distance. The sixth term is the effect of the mode-dependent Gouy phase $\Phi(z) = (2p + |\ell| + 1)\arctan(z/z_R)$.

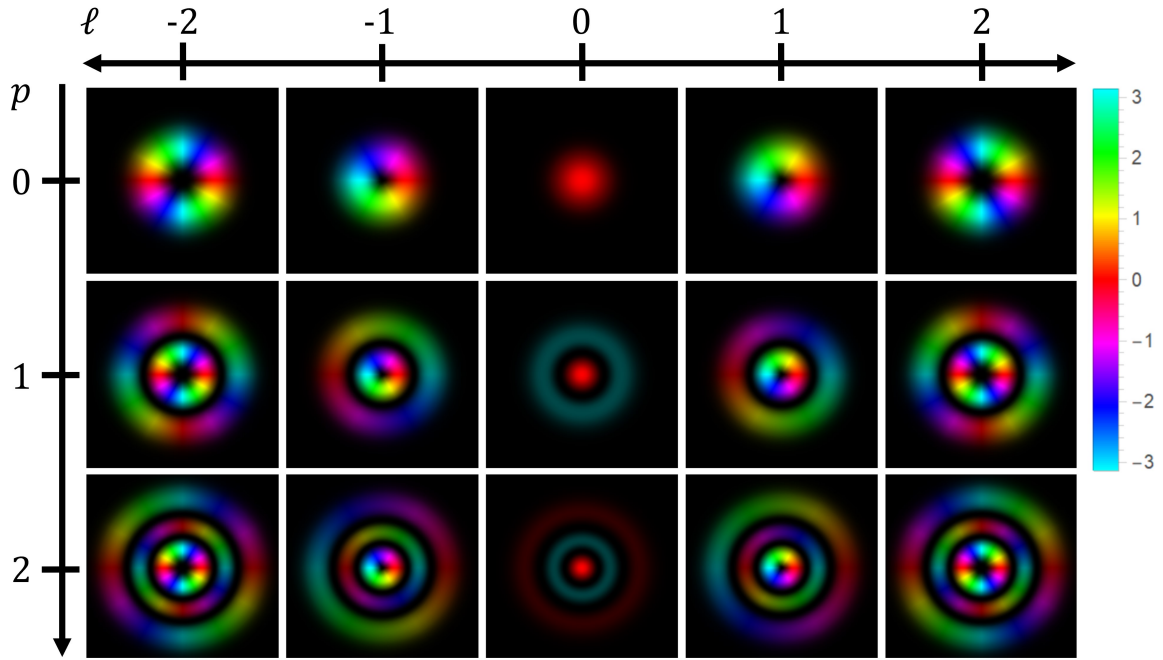


Figure 1.1: **Laguerre–Gauss modes.** Phase profiles modulated by the intensity profiles of LG modes with $\ell = -2, -1, 0, 1, 2$ and $p = 0, 1, 2$.

And finally, the seventh and most useful term is $e^{i\ell\phi}$, which is an azimuthally varying phase factor attributed to $\ell\hbar$ units of orbital angular momentum (OAM).

OAM is associated with the wavefront of light, whereas spin angular momentum (SAM) is associated with its vectorial nature—i.e., polarization, which will be described in the next section. For LG modes, the $e^{i\ell\phi}$ factor manifests as $|\ell|$ intertwined helical contours of constant phase in the wavefront. The handedness of these helices is given by the sign of ℓ . In the intensity profile, this structure is exhibited as a doughnut-like form, with a null along the propagation axis due to the presence of a phase singularity. The radial index p , on the other hand, adds p extra rings, π out of phase with each other, see Fig. 1.1 for examples. Generally, we are not concerned with modes with $p \neq 0$, and refer to modes with $p = 0$ as pure OAM states. In Dirac notation, a quantum state carrying $\ell\hbar$ units of OAM will be written as $|\ell\rangle$.

Laguerre–Gauss modes were first experimentally demonstrated to carry a well-defined orbital angular momentum by Allen *et al.* in 1992 [20]. Since then, OAM has found numerous application in a variety of fields, including high-dimensional quantum communication

to improve the security and quantum bit error rate [21], stimulated emission depletion (STED) microscopy to improve imaging resolution [22], and coronagraphy for detecting exoplanets [23] to name a few. Of course, LG modes are not the only modes of light to possess OAM; for example, Bessel–Gauss, which are non-diffracting, and Hypergeometric–Gauss modes also may possess OAM.

1.2.2 Generation techniques

Generating light with a particular OAM value boils down to how the $e^{i\ell\phi}$ phase factor can be imprinted. The most straightforward method is to use a spiral phase plate [24], which as the name implies, is a transparent medium with a base thickness of d_0 and an azimuthally dependent thickness profile above it,

$$d(\phi) = \frac{\ell\lambda}{2\pi(n - n_0)}\phi = \frac{d_{step}}{2\pi}\phi, \quad (1.9)$$

where n and n_0 are the refractive indices of the spiral phase plate and surrounding medium, respectively, and d_{step} is the step height above the base at $\phi = 0$. This will consequently imprint an azimuthal phase $\delta = \frac{2\pi}{\lambda}(n - n_0)d(\phi) = \ell\phi$, based on the optical path difference by construction.

The next method to generate OAM modes is to use what is called a mode converter based on cylindrical lenses [25]. This method relies on the fact that Hermite–Gauss modes can be decomposed into Laguerre–Gauss modes, and *vice versa*. This is particularly useful since the output of most lasers is in a Hermite–Gauss mode due to the nature of the cavity geometry. The construction of the mode converter is a pair of identical cylindrical lenses with focal length f separated by a distance of $\sqrt{2}f$ for a $\pi/2$ -converter. A $\pi/2$ -converter will transform HG to LG modes of the same order, where their mode order is $N = n + m$ and $N = 2p + |\ell|$, respectively.

Arguably the most useful and versatile method for generating OAM modes, or any transverse spatial mode in general, is with a spatial light modulator (SLM) using holography. A phase-only SLM consists of an array of liquid-crystal cells, with the ability to apply a different voltage to each cell. The theory and physics of liquid crystals will be explained in detail later in this thesis. For the time being, these liquid crystal cells act as pixels, wherein the grayscale displayed (changing the applied voltage) corresponds to a different phase that is imparted on incident light. Typically, a phase is only imprinted on horizontally polarized light. Some SLMs are transmissible, though most operate in reflection. Not all types of SLMs can impart a phase from 0 to 2π or more by strictly displaying

the desired phase in grayscale, which could greatly hinder the generation of certain modes. Additionally, we can only structure the phase profile and not the amplitude profile in this way.

This is where holography comes in, which gives the ability to simultaneously tailor both the phase and intensity of incident light [26]. The principle behind holography is that when two beams of light with identical polarizations but different wave vectors are superimposed, they will form an interference pattern at the plane of intersection; for this example, consider the reference beam as a Gaussian, the other as a desired spatial mode. However, this interaction can be done in reverse. If a hologram is created according to this interference pattern, either in amplitude or phase, an incident Gaussian beam will be diffracted into different orders; the zeroth and first are in the Gaussian and spatial mode used originally for interference. Thus the phase of the desired spatial mode is imprinted on the incident beam. An amplitude hologram modifies the intensity, so a phase hologram is more desirable as it is less lossy. However, we don't have the correct control over the amplitude profile using only the direct interference pattern as a hologram; for this, we should include intensity masking.

Consider the desired output field of $E(x, y) = A(x, y)e^{i\Phi(x, y)}$, where $A(x, y) = |E(x, y)|$ and $\Phi(x, y) = \text{Arg}(E(x, y))$ are the amplitude and phase, respectively, at the $z = 0$ plane. Then the hologram to imprint only phase is given by,

$$\Psi(i, j) = \text{Mod}[\Phi(i, j) + 2\pi \sin(\theta_x)i/\Lambda + 2\pi \sin(\theta_y)j/\Lambda, 2\pi], \quad (1.10)$$

where i, j are the pixel coordinates in the x and y directions, and θ_x and θ_y are the diffraction angles of the first order in the x and y directions. The shape of the fringes given by this formulation is a blazed grating with period Λ , which has been shown to optimize the efficiency of diffraction into the first order where the desired output field resides. For a phase-only hologram that also modulates the intensity, the form is modified to,

$$\Psi(i, j) = \mathcal{M}(i, j)\text{Mod}[\mathcal{F}(i, j) + 2\pi \sin(\theta_x)i/\Lambda + 2\pi \sin(\theta_y)j/\Lambda, 2\pi], \quad (1.11)$$

$$\mathcal{M}(i, j) = 1 + \frac{1}{\pi}\text{sinc}^{-1}(A(i, j)), \quad (1.12)$$

$$\mathcal{F}(i, j) = \Phi(i, j) - \pi\mathcal{M}(i, j). \quad (1.13)$$

Note the presence of $\text{sinc}^{-1}(\cdot)$ which is the inverse function of $\text{sinc}(x) = \sin x/x$ in the interval of $[-\pi, 0]$. This can be a computationally heavy function to calculate, so programs typically use a lookup table for faster operation. Since $0 \leq \mathcal{M} \leq 1$, then $0 \leq \Psi \leq 2\pi$. Indeed, the displayed hologram only relies on the relative values of grayscale that each pixel displays as opposed to the phase that a specific gray value would impart. Therefore,

using holograms to generate spatial modes is suitable for any phase-only SLM. I wrote a custom interface in Python that connects to a SLM and allows the user to display and manipulate the holograms for various spatial modes—available upon request.

Other types of liquid-crystal optical elements, such as q -plates [10, 27], can be used to generate spatial modes; however, these will be discussed in Sec. 2.4.

1.3 Polarization

1.3.1 Jones calculus

In free-space and under the paraxial regime discussed above, light is an electromagnetic wave with an electric and magnetic field oscillating in the plane transverse to its propagation direction. Here, the direction of propagation will be along the z -axis in the positive direction, and the transverse plane will be in the x - y plane. The polarization of light is given by the manner in which the electric field oscillates, describing its vectorial nature. The electric field for a monochromatic plane wave of wavelength λ will thus be defined as [28],

$$\mathbf{E}(z, t) = \text{Re}\{\mathbf{A}e^{i(\omega t - kz)}\}, \quad (1.14)$$

with ω the angular frequency of the light, and $k = 2\pi/\lambda$ the wavenumber. The normalized complex Jones vector representing polarization is given as $\mathbf{A} = A_x\hat{\mathbf{x}} + A_y\hat{\mathbf{y}}$, or equivalently,

$$\mathbf{A}(\Delta, \delta) = a_x e^{i\delta_x} \hat{\mathbf{x}} + a_y e^{i\delta_y} \hat{\mathbf{y}} = e^{i\delta_x} (a_x \hat{\mathbf{x}} + a_y e^{i\delta} \hat{\mathbf{y}}) = \cos \Delta \hat{\mathbf{x}} + \sin \Delta e^{i\delta} \hat{\mathbf{y}}, \quad (1.15)$$

where $\delta = (\delta_y - \delta_x) \in [-\pi/2, \pi/2]$ is the relative phase between the horizontal and vertical components, and $a_x^2 + a_y^2 = 1$, with it being convenient to take $a_x = \cos \Delta$ and $a_y = \sin \Delta$, $\Delta \in [0, \pi]$. The global phase of $e^{i\delta_x}$ can be safely ignored. The six cardinal polarization—horizontal (H), vertical (V), diagonal (D), anti-diagonal (A), right-hand circular (R), and left-hand circular (L)—are then, respectively,

$$\mathbf{A}_H = \hat{\mathbf{x}} = \begin{bmatrix} 1 \\ 0 \end{bmatrix}, \mathbf{A}_V = \hat{\mathbf{y}} = \begin{bmatrix} 0 \\ 1 \end{bmatrix}, \quad (1.16)$$

$$\mathbf{A}_D = \frac{1}{\sqrt{2}} \begin{bmatrix} 1 \\ 1 \end{bmatrix}, \mathbf{A}_A = \frac{1}{\sqrt{2}} \begin{bmatrix} 1 \\ -1 \end{bmatrix}, \quad (1.17)$$

$$\mathbf{A}_R = \frac{1}{\sqrt{2}} \begin{bmatrix} 1 \\ i \end{bmatrix}, \mathbf{A}_L = \frac{1}{\sqrt{2}} \begin{bmatrix} 1 \\ -i \end{bmatrix}. \quad (1.18)$$

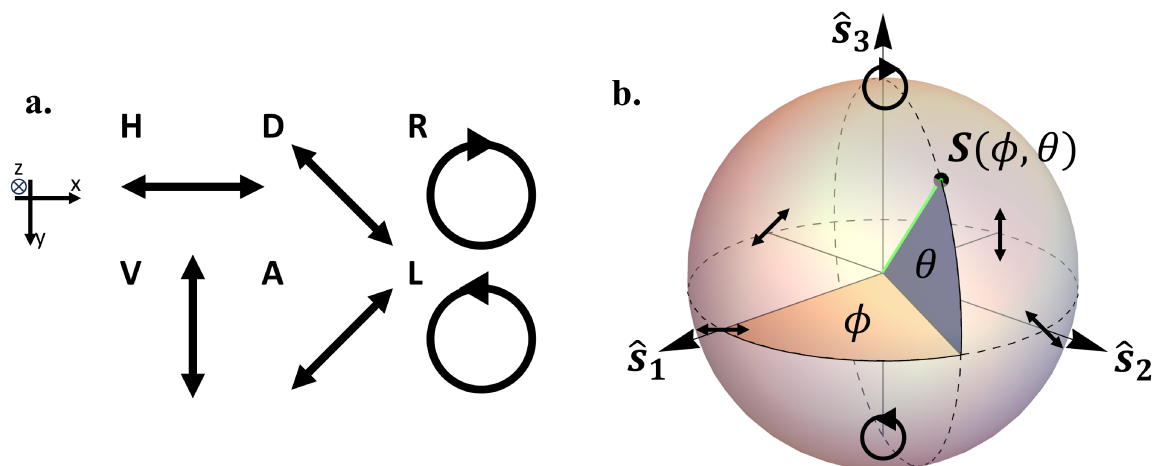


Figure 1.2: **Polarization representations.** a. Convention used for the six cardinal polarizations from the point of view of the source. b. Depiction of a general polarization state on the Poincaré sphere given its Stokes vector $\mathbf{S}(\phi, \theta)$.

In general, any linear polarization can be created by taking $\delta = 0$ and varying the amplitude weights. As we see above, the circular polarizations occur when $a_x = a_y$ (i.e., $\Delta = \pi/4$) and $|\delta| = \pi/2$. For general elliptical polarizations, the sign of δ dictates the handedness, with positive (negative) corresponding to right-(left-)handedness. There is now the matter convention as to how these states are visually represented, as this can be inconsistent in the literature. The two equivalent conventions comes down to whether the polarization is seen from the point of view of the source (towards positive z) or receiver (towards negative z). For this thesis, I will take the convention from the point of view from the source [28], as if we are riding on the beam of light as it propagates through space, facing what is to come. In this way, right-hand circularly polarized light, which rotates always in the right-hand sense with respect to propagation, is seen as rotating clockwise; conversely, left-hand circularly polarized light rotates counter-clockwise. Similarly, diagonally polarized light oscillates from the top-left quadrant to the bottom-right, and anti-diagonal from the bottom-left to top-right. This convention is shown in Fig. 1.2a for visual ease.

Operations performed on the Jones vector is done through matrix multiplication. Linear optical elements are represented by 2×2 matrices, with unitaries, such as waveplates and phase retarders, belonging to the $SU(2)$ group. Note, only fully polarized light will be considered here, as Jones calculus cannot be applied to partially or randomly polarized

light. The relevant matrices for here are the rotation matrix,

$$\mathbf{R}(\cdot) = \begin{bmatrix} \cos(\cdot) & \sin(\cdot) \\ -\sin(\cdot) & \cos(\cdot) \end{bmatrix}, \quad (1.19)$$

as well as the Jones matrix for a waveplate of phase retardation Γ with its fast axis along the x -axis,

$$\mathbf{W}_0(\Gamma) = \begin{bmatrix} e^{-i\frac{\Gamma}{2}} & 0 \\ 0 & e^{i\frac{\Gamma}{2}} \end{bmatrix}. \quad (1.20)$$

An arbitrarily rotated waveplate, or optical element in general, can be obtained through the transformation $\mathbf{W}_\xi(\Gamma) = \mathbf{R}(-\xi)\mathbf{W}_0(\Gamma)\mathbf{R}(\xi)$,

$$\mathbf{W}_\xi(\Gamma) = e^{-i\frac{\Gamma}{2}} \begin{bmatrix} \cos^2 \xi + e^{i\Gamma} \sin^2 \xi & (1 - e^{i\Gamma}) \cos \xi \sin \xi \\ (1 - e^{i\Gamma}) \cos \xi \sin \xi & \sin^2 \xi + e^{i\Gamma} \cos^2 \xi \end{bmatrix}. \quad (1.21)$$

Note that matrix multiplication is performed right to left, with the rightmost matrix being the first operation or optical element in a set, and the leftmost the last.

The phase retardation is defined as $\Gamma = 2\pi(n_e - n_o)d/\lambda$, where d is the thickness of the waveplate, λ is the wavelength of the incident light, and n_e and n_o are the refractive indices along the extraordinary and ordinary axes of the constituent birefringent uniaxial material. The materials considered here are assumed to have positive birefringence, i.e., $\Delta n = n_e - n_o > 0$. The extraordinary and ordinary axes are equivalently termed the slow and fast axes of the material, respectively, as the electric field traveling along the higher effective refractive index (in this case, n_e) will have a slower phase velocity. Then Γ denotes the phase by which the electric field along the slow axis is delayed in comparison to the field along the fast axis. For example, half-wave plates (HWP) have $\Gamma = \pi$, while quarter-wave plates (QWP) have $\Gamma = \pi/2$. With just these two types of waveplates, it is possible to arbitrarily and generally transform a polarization state [29].

1.3.2 Poincaré sphere

As a complex 2D spinor, completely polarized states can also be represented as a point on the surface of a unit sphere. This Poincaré sphere (PS) is the polarization equivalent of the Bloch sphere for spin-1/2 or other two-level systems. Note for partially polarized light, the state will lie within the unit sphere, on a sphere with a radius equal to the

degree of polarization. A polarization state's position on the PS is determined through the corresponding (normalized) Stokes parameters from its Jones vector as follows [30],

$$S_0 = |\mathbf{A}_H|^2 + |\mathbf{A}_V|^2 = A_x A_x^* + A_y A_y^* = a_x^2 + a_y^2 = 1, \quad (1.22)$$

$$S_1 = |\mathbf{A}_H|^2 - |\mathbf{A}_V|^2 = A_x A_x^* - A_y A_y^* = a_x^2 - a_y^2 = \cos \phi \cos \theta, \quad (1.23)$$

$$S_2 = |\mathbf{A}_D|^2 - |\mathbf{A}_A|^2 = A_x A_y^* + A_y A_x^* = 2a_x^2 a_y^2 \cos \delta = \sin \phi \cos \theta, \quad (1.24)$$

$$S_3 = |\mathbf{A}_R|^2 - |\mathbf{A}_L|^2 = i(A_x A_y^* - A_y A_x^*) = 2a_x^2 a_y^2 \sin \delta = \sin \theta, \quad (1.25)$$

such that its Stokes vector is $\mathbf{S} = S_1 \hat{\mathbf{s}}_1 + S_2 \hat{\mathbf{s}}_2 + S_3 \hat{\mathbf{s}}_3 = [S_1, S_2, S_3]$, and $\phi \in [0, 2\pi)$ and $\theta \in [-\pi/2, \pi/2]$ are the azimuthal and polar angles of the PS, respectively. The Stokes vector can alternatively be expressed in terms of the spherical coordinates as $\mathbf{S}(\phi, \theta)$, with the angles defined as,

$$\phi = \arctan\left(\frac{S_2}{S_1}\right), \quad (1.26)$$

$$\theta = \arctan\left(\frac{S_3}{\sqrt{S_1^2 + S_2^2}}\right). \quad (1.27)$$

In particular, we have that $\phi = 2\Delta$ for $\delta = \pi/2$, and $\theta = \delta$ for $\phi = \pi/2$ in relation to Eq. (1.15). Figure 1.2b shows an example of a general polarization state on the PS. The three axes correspond to the three pairs of cardinal polarizations: horizontal and vertical are at the positive and negative ends of the $\hat{\mathbf{s}}_1$ axis, respectively; diagonal and anti-diagonal for $\hat{\mathbf{s}}_2$; and right-handed and left-handed circular for $\hat{\mathbf{s}}_3$. As such, all linear states are along the equator of the PS, and orthogonal states are positioned at antipodal points.

1.4 Structured light

The beauty of light is its potential to be shaped and *structured* to the whims of the user. Light need not be strictly ascribed to one spatial mode or one polarization—it may be put into a coherent superposition of different spatial modes, different polarizations, and even different frequencies. This results in complex distributions for the polarization in the spatial and temporal domain. The concept of structuring light is equally valid for its constituent photons, adding the potential to play with different photon numbers. For our purposes here, we only concern ourselves with a single frequency component, as well as single-photon states when in the quantum regime.

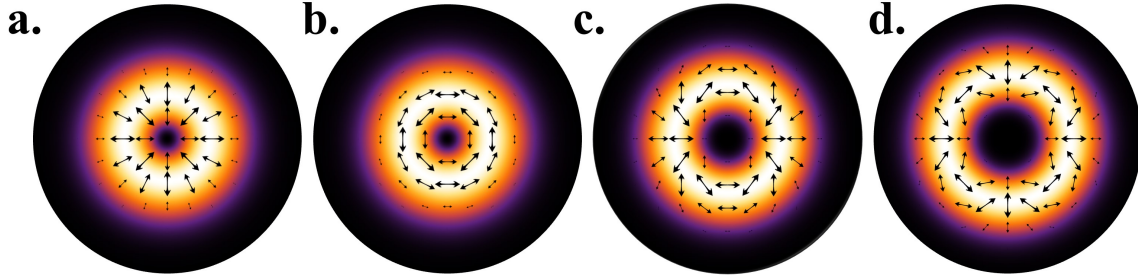


Figure 1.3: **Vector vortex beams.** a. Radially polarized light. b. Azimuthally polarized light. c. Vector vortex mode with $|\ell| = 2$. d. Vector vortex mode with $|\ell| = 3$.

A very general structured light mode may be represented as,

$$\mathbf{U}(\mathbf{r}) = \sum_{\pi, \ell, p} c_{\ell, p}^{\pi} \text{LG}_{\ell, p}(\mathbf{r}) \mathbf{A}_{\pi}, \quad (1.28)$$

where π is polarization, and $c_{\ell, p}^{\pi}$ are the coefficients. Here, the Laguerre–Gauss modes were chosen as the spatial modes, but Hermite–Gauss or any other complete set could have been chosen. The most trivial structured modes are those with a single spatial mode and single polarization; for example, $\text{LG}_{0,0} \mathbf{A}_H$ is a horizontally polarized Gaussian beam. The dependency on \mathbf{r} has been dropped for ease of notation. A slightly more interesting class of structured modes are vector vortex beams of the form $(\text{LG}_{\ell,0} \mathbf{A}_R + \text{LG}_{-\ell,0} \mathbf{A}_L) / \sqrt{2}$. The polarization distribution of vector vortex beams consists of only linear polarizations; for example, $(\text{LG}_{1,0} \mathbf{A}_R + \text{LG}_{-1,0} \mathbf{A}_L) / \sqrt{2}$ is a radially polarized beam, whereas $(\text{LG}_{1,0} \mathbf{A}_R - \text{LG}_{-1,0} \mathbf{A}_L) / \sqrt{2}$ is azimuthally polarized. Some examples are given in Fig. 1.3. An even more interesting type of structured light is polarization knots, where upon propagation, knotted lines of circular polarization occur within a certain volume [31].

Chapter 2

Liquid Crystals

2.1 A brief history

For a long time, there were thought to be three states of matter: solid, liquid, gas. Of course, we now know there to be a few more, including plasma, Bose–Einstein condensates, and the matter at hand here, liquid crystals. This latter state has the fluidity of liquids, but also the ordered arrangement of solid crystals. The history behind the state of matter known as liquid crystals is quite a fascinating one, spanning all the way back to the end of the 19th century. In the space I have here, I would not be able to do justice in recounting its story. However, there is a wonderful compendium, *Crystals that Flow* [32], which I highly recommend the interested reader to peruse as the authors have included commentary and translations for the original classic papers in chronological order. I thus present here only a small glimpse into the history of liquid crystals.

The first observations of this strange phenomenon were made by Austrian botanist Friedrich Reinitzer in 1888, who discovered that cholesteryl benzoate—which he had extracted from carrots—showed two melting points, suggesting the existence of a new state of matter [33]. The solid melted into a cloudy liquid at 145.5°C, then suddenly became a clear liquid at 178.5°C, with strong colour shifts around each transition; it was also a reversible process. This second melting point was later termed the ‘clearing point’. Reinitzer shared his findings with German crystallographer Otto Lehmann, hoping his experience in polarization microscopy would shed some light on the situation. Lehmann did indeed observe crystallites in the intermediate cloudy liquid, and it displayed birefringent properties. He continued to investigate the coexistence of liquidity and crystallinity for several decades.

In 1904, Lehmann coined the term “liquid crystal” to describe the state of matter he had observed, publishing his extensive findings in his similarly named book [34].

From this point, chemists were able to synthesize various types of liquid crystals; however, an adequate theoretical model to describe their behaviour was severely lacking. Emil Bose attempted to develop a model using van der Waals’ theory of fluids, introducing the idea of molecular swarms (*Molekülschwärmen*) wherein swarms of molecules pointed roughly in the same direction [35]. While it did not correctly provide a good molecular theory for liquid crystals, it was the overarching accepted idea even as late as 1957 [36]. For many years, the study of liquid crystals was confined to the realm of curiosity. However, it wasn’t until the 1960s that liquid crystals began to be used in practical applications, such as in digital displays. Richard Williams, then working at RCA Laboratories, New Jersey, discovered that applying an electric field across a thin layer of nematic liquid crystals caused stripe patterns to form [37]. This phenomenon was termed *Williams’ domains*, which led his colleague George Heilmeier in 1968 to develop the first practical flat liquid-crystal-based display (LCD) [38]. Since then, liquid crystals have become an integral part of many electronic devices, including televisions, computer monitors, calculators, and mobile phones. They have also found applications in a wide range of other fields, such as medicine, cosmetics, and materials science, forming the multi-billion dollar industry we have today.

As for the molecular theory of liquid crystals, in particular their transitions between different phases, this mystery was finally put to rest by French physicist Pierre-Gilles de Gennes between 1968 and 1972 [4, 39]. de Gennes introduced the concept of the order parameter—a tensor quantity—which describes the degree of alignment of the molecules in a liquid crystal. From this, he constructed the Landau-type free-energy expansion in terms of invariant powers of the order parameter and of its gradients, establishing a link between liquid crystals and other ordered systems where the Landau theory of phase transitions is applicable. He also developed a theory to describe the behavior of nematic liquid crystals, which are liquid crystals in which the molecules are oriented in a particular direction but are not fixed in place. In 1991, de Gennes was awarded the Nobel Prize in Physics “for discovering that methods developed for studying order phenomena in simple systems can be generalized to more complex forms of matter, in particular to liquid crystals and polymers.”

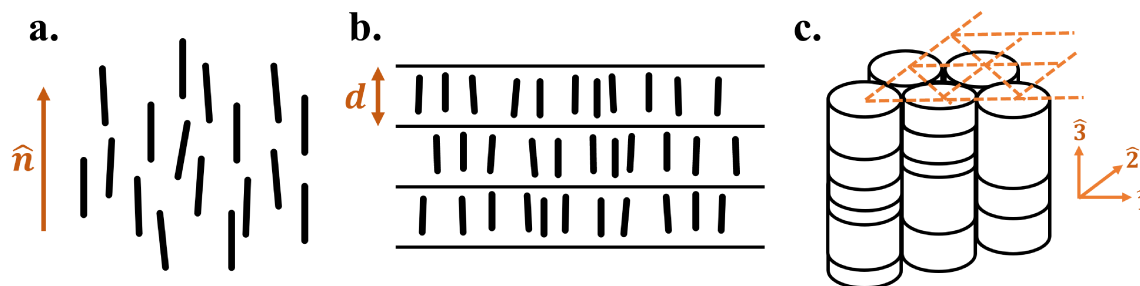


Figure 2.1: **Liquid crystal mesophases.** a. Nematics with average director direction \hat{n} . b. Smectics, specifically type A, with liquid layers of spacing d . c. Columnar phases with tubes of liquid along structure lattice vectors $\{\hat{1}, \hat{2}, \hat{3}\}$.

2.2 Mesophases

From its intermediary nature, a more apt name for liquid crystals is *mesomorphic* state of matter, or *mesophase* for short. Of course, we now must ask the question, what *is* a liquid crystal? What causes its simultaneous liquidy and crystalline properties? This unique behavior boils down to the order, shape, and transition mechanism of the organic molecules that make up liquid crystals.

While we can typically qualitatively label something as a *liquid* or *solid* by its appearance and behaviour of fluidity or solidity—such as flowing water versus ice crystals—a more rigorous metric should be used in order to distinguish the *liquid crystal* state. For this, we should look at the *order* of the constituent components. In a solid or crystal, the components are positioned on a three-dimensional periodic lattice; if they exhibit a pattern at one location, there is always the probability to find an equivalent pattern by a discrete translation along the lattice. On the contrary for (isotropic) liquids, there is no sense of order between the components; if there happens to be a pattern at one location, there is no probability to locate another instance of it no matter how far away or what direction you go. In other words, there is no correlation between one component and a neighbouring component far enough away, independent of spatial direction.

The order of liquid crystals, therefore, lies in between these two cases, wherein there is some liquid-like order in at least one spatial direction and there is some anisotropy. This can occur when there is (i) no positional ordering, (ii) positional ordering in one direction, or (iii) positional ordering in two dimensions. These three cases result in the three main types of mesophases: (i) nematic, (ii) smectic, and (iii) columnar phases. For (i), as we've seen, no positional ordering can refer to a liquid; however, if there is anisotropy present—

i.e., the loss of correlation is different in two orthogonal directions—orientation is what matters. Smectics, which have one-dimensional order, appear as distinctly spaced stacks of two-dimensional liquid layers. On the other hand, columnar phases, as per their name, manifest as a two-dimensional array of liquid tubes. Figure 2.1 demonstrates these three mesophases.

Which mesophase occurs is highly dependent on the shape of the organic molecular components; they are usually either rod- or disc-shaped. Nematics and smectics tend to be elongated and rod-shaped, on the order of tens of angstrom long; meanwhile, most columnar phases and some nematics are disc-shaped. As this is not a thesis in chemistry, exact chemical formulae will be omitted; though, the reader is welcome to consult [4] for various examples of the different mesophases. Overall, the order plays a crucial role in explaining the transitions between different liquid crystal phases. The three main mechanisms that drive these transitions is temperature (thermotropic), molecular concentration (lyotropic), and the presence of inorganic molecules (metallotropic). For example, nematics are thermotropic.

Let us take a closer look at the nematic phase, which is the primary subject of this thesis. As there is only short-range positional order, its behavioural characteristics are derived from the long-range order in the orientation of the molecules. The uniaxial, rod-shaped molecules prefer to align with some common axis, called the *director*, defined as a unit vector $\hat{\mathbf{n}}$. The direction of the director is arbitrary, though it can be influenced by external means such as containment walls or electric and magnetic fields. Additionally, the ‘head’ ($\hat{\mathbf{n}}$) and ‘tail’ ($-\hat{\mathbf{n}}$) of the nematic molecules are indistinguishable, even if they themselves are polar. At high temperatures, the order is small, and the material behaves as an isotropic liquid, where the orientation of the molecules is completely random. As the temperature is lowered, the order increases, and the molecules become more aligned.

How ordered a nematic mesophase is can be quantified through an order parameter [4]. The complete description of the order parameter—in particular the general tensor order parameter—is beyond the scope of this thesis. However, a small understanding can be grasped from considering the alignment of nematic rigid rods. Each rod has cylindrical symmetry about its long axis $\hat{\mathbf{n}}'$ and makes an angle θ with the director axis $\hat{\mathbf{n}}$ of the whole nematic substance. There will be some distribution function $f(\theta)$ that describes the alignment of the rods, with a maximum around parallel alignment ($\theta = 0$ or π), and a minimum around perpendicular alignment ($\theta = \pi/2$). The full form of $f(\theta)$ may be complicated and different for different nematic systems, so it is more informative to find a single numerical parameter that describes the state of alignment. One could consider the

average alignment as a possible candidate,

$$\langle \hat{\mathbf{n}}' \cdot \hat{\mathbf{n}} \rangle = \langle \cos \theta \rangle = \int f(\theta) \cos \theta d\Omega, \quad (2.1)$$

where $d\Omega$ is the solid angle differential. Unfortunately, this quantity is identically zero by the fact that $f(\theta) = f(\theta - \pi)$, i.e., there is no average dipole. However, one could consider a multipole expansion using $P_\ell(\cos \theta)$, where $P_\ell(\cdot)$ are the Legendre polynomials. The next higher multipole $P_2(\cos \theta)$ gives better incite, with the quadrupole being,

$$S = \frac{1}{2} \langle 3 \cos^2 \theta - 1 \rangle = \frac{1}{2} \int f(\theta) (3 \cos^2 \theta - 1) d\Omega. \quad (2.2)$$

We see that if there is strong parallel alignment with $\theta = 0$ or π , then $\cos \theta = \pm 1$ and $S = 1$. If there is strong perpendicular alignment with $\theta = \pi/2$, $S = -1/2$. And importantly, if $f(\theta)$ is uniform and independent of θ , this gives random isotropic orientation like in a liquid, and consequently, $S = 0$. S is, therefore, an appropriate order parameter. This order parameter can be measured using nuclear magnetic resonance [40], fluorescence [41], Raman scattering [42], and infrared spectroscopy [43], though these will not be described here. From here on out, when I refer to liquid crystals, I am referring to the nematic mesophase.

2.3 Physical and Optical properties

2.3.1 Bulk and boundary effects

In order to practically make use of liquid crystals, they should be contained in some form. A suitable cell to imprison them is in between two glass plates, and the edges have been appropriately sealed. The fabrication process of such a liquid crystal cell will be detailed in Sec. 3.3. However, we can begin to look at the boundary and bulk behaviour of nematics in a cell—so-called long-range distortions—qualitatively for the time being.

If the glass walls of the container possess a particular alignment direction—for example, if the surfaces are rubbed in one direction, or coated with a polymer layer—then the liquid crystals at the boundaries will preferentially line up parallel to that direction. This is referred to as the *easy direction* of the director $\hat{\mathbf{n}}$ which minimizes the energy of the surface region. It is also possible to align the liquid crystals perpendicular to the glass walls by treating surfaces with certain detergents. The polar heads of the detergent molecules

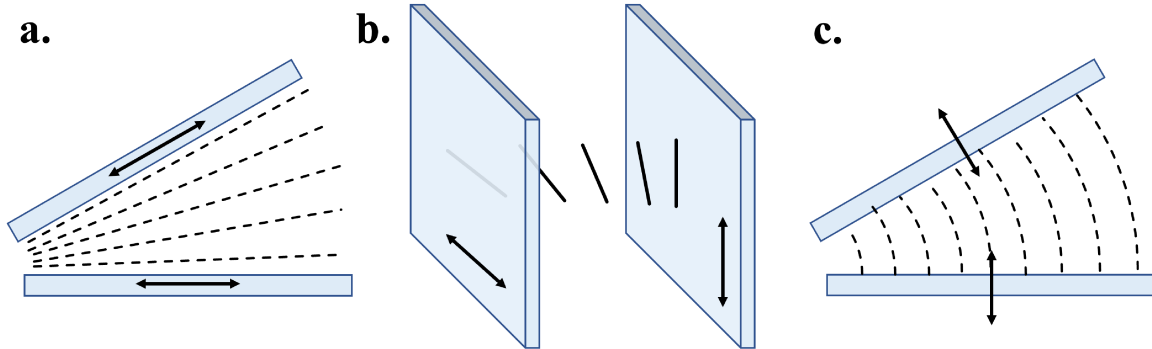


Figure 2.2: **Bulk distortions.** When nematic liquid crystals are placed between two glass plates with a particular alignment direction (denoted by the arrows), they can exhibit a. splay, b. twist, and c. bend distortions to conform with the boundary conditions.

attach to the glass surface, and the liquid crystals align themselves accordingly in this normal orientation. With these two kinds of surface treatments, we can create the three main types of bulk distortions—splay, twist, and bend—as shown in Fig. 2.2.

There is then the matter of how strong is the anchoring to the glass walls. If the anchoring is weak, then the distortions of the bulk nematics may be affected by the surface region. The anchoring can be quantified by the so-called extrapolation length b , which is a measure for how far into the bulk the surface distortions will effect [4],

$$b \sim a \frac{U}{U_{\text{WN}}}, \quad (2.3)$$

where a is the average molecular dimension, U is the nematic–nematic interaction energy, and U_{WN} is the interaction energy between the glass wall and one nematic molecule directly in contact with the wall. If $U_{\text{WN}} \geq U$, then $b \sim a$. Of course, a is much smaller than the total thickness L of the cell, so we may neglect any surface contributions to the bulk distortions beyond the boundary condition imposed by the easy direction. This is *strong* anchoring. On the other hand, if $U_{\text{WN}} \ll U$, then b becomes much larger than a , and we have weak anchoring. For the liquid-crystal devices fabricated for this thesis, strong anchoring is assumed.

2.3.2 Birefringence

As discussed briefly in Sec. 1.3 in regards to waveplates, birefringence is caused by anisotropy in the material, with different refractive indices along different directions. For positive uni-

axial crystals ($n_e > n_o$), the component of light polarized along the slow or extraordinary axis of the crystal will travel with a slower phase velocity ($v_p = c/n_e$) than the component polarized along the fast or ordinary axis ($v_p = c/n_o$). Nematic liquid crystals are one such example of a positive uniaxial crystal with $\Delta n = n_e - n_o \sim 0.1$. Unlike a waveplate which is typically placed normal to an incoming light beam, nematics may be arbitrarily oriented depending on the bulk deformation and applied field. The phase retardation that is imparted from a birefringent crystal depends on the orientation of the crystal with respect to the incoming light beam. An easy way to both visualize and determine the action of an arbitrarily oriented birefringent crystal is to use what is known as the refractive index ellipsoid.

Suppose we have a general birefringent crystal with electric permittivity tensor,

$$\overset{\leftrightarrow}{\epsilon} = \epsilon_0 \begin{bmatrix} n_x^2 & 0 & 0 \\ 0 & n_y^2 & 0 \\ 0 & 0 & n_z^2 \end{bmatrix}, \quad (2.4)$$

with $\mathbf{D} = \overset{\leftrightarrow}{\epsilon} \mathbf{E}$. Then the energy density is given by,

$$u = \frac{1}{2} \mathbf{E} \cdot \mathbf{D} = \frac{1}{2} \left(\frac{D_x^2}{\epsilon_0 n_x^2} + \frac{D_y^2}{\epsilon_0 n_y^2} + \frac{D_z^2}{\epsilon_0 n_z^2} \right), \quad (2.5)$$

which can be rearranged to,

$$1 = \frac{(D_x/\sqrt{(2\epsilon_0 u)})^2}{n_x^2} + \frac{(D_y/\sqrt{(2\epsilon_0 u)})^2}{n_y^2} + \frac{(D_z/\sqrt{(2\epsilon_0 u)})^2}{n_z^2} = \frac{\bar{x}^2}{n_x^2} + \frac{\bar{y}^2}{n_y^2} + \frac{\bar{z}^2}{n_z^2}. \quad (2.6)$$

Equation 2.6 defines the refractive index ellipsoid, or optical indicatrix, with semi-axes given by n_x , n_y , and n_z along the principal axes \bar{x} , \bar{y} , and \bar{z} , respectively [44]. These axes have been suggestively labelled as they have because they coincide with the Cartesian axes (x, y, z) ; if light is propagating along the z -axis, the corresponding vector on the index ellipsoid will also be along the \bar{z} axis. For a uniaxial liquid crystal with its fast axis along x -axis, $n_x = n_z = n_o$, $n_y = n_e$, creating an ellipsoid that mimics the grain-like shape of nematics. Figure 2.3a gives the configuration for light propagating with wavevector \mathbf{k} in the y - z plane at an angle θ from the z -axis.

The refractive index ellipsoid allows us to determine the linear eigenpolarizations in the crystal for a tilted beam (or tilted crystal), as well as the refractive indices experienced by them. For light propagating with wavevector \mathbf{k} , the eigenpolarizations are the axes of the plane that is spanned by \mathbf{D} such that $\mathbf{D} \cdot \mathbf{k} = 0$ and intersects with the index ellipsoid.

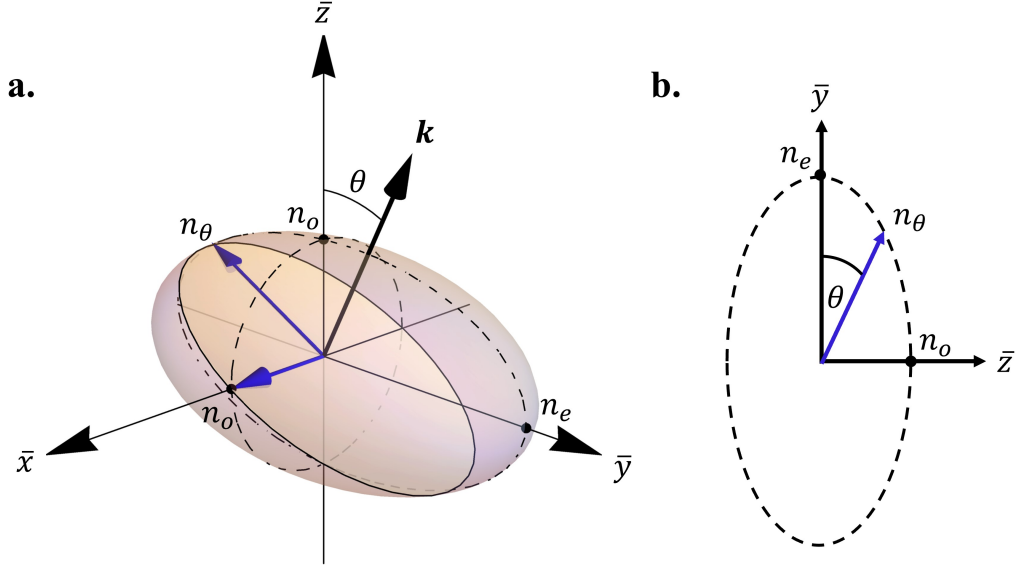


Figure 2.3: **Refractive index ellipsoid of uniaxial crystal.** a. For light propagating at an angle θ , the eigenpolarizations will be given by the blue vectors. b. The effective refractive index n_θ experienced by one of the eigenpolarizations.

The magnitude of these eigenvectors is the refractive index that each experiences. If the director of the liquid crystal is tilted by an angle θ with respect to the incident light—equivalently, the scenario shown in Fig. 2.3a—the effective refractive index n_θ that one of the eigenpolarizations experiences upon propagation is consequently modified to,

$$\frac{1}{n_\theta^2} = \frac{\cos^2 \theta}{n_e^2} + \frac{\sin^2 \theta}{n_o^2} \implies n_\theta \approx \Delta n \cos^2 \theta + n_o, \quad (2.7)$$

where the approximation is made that $\Delta n \ll n_o$. This is determined from the ellipse of the cross-section shown in Fig. 2.3b. For a cell of liquid crystals, which may have an arbitrary deformation with tilt distribution $\theta(z)$, the phase retardation experienced by the beam throughout the cell is,

$$\begin{aligned} \Gamma(z) &= \frac{2\pi}{\lambda} \int_0^z [n_\theta(z') - n_o] dz' \\ &\approx \frac{2\pi \Delta n}{\lambda} \int_0^z \cos^2 \theta(z') dz'. \end{aligned} \quad (2.8)$$

When the liquid crystal directors are all perpendicular to the optical axis ($\theta = 0$), $\Gamma(L) = 2\pi \Delta n L / \lambda$ is maximal. However, when the directors are all parallel with the optical axis

($\theta = \pi/2$), the incident light sees a circle instead of an ellipse in index space, and there is consequently no birefringence or phase retardation. It is possible to tilt liquid crystals by applying an external electric field, allowing for a field-tunable phase retardation.

2.4 Pancharatnam–Berry optical elements

The general class of devices that can structure light by coupling polarization to spatial modes is referred to as Pancharatnam–Berry optical elements (PBOEs), and may be based on dielectrics [45], plasmonics [46], or liquid crystals [47, 48], which we describe here. We consider for now the trivial configuration of LC cells where the front and back glass walls have parallel alignment, but spatial patterning—no splay, twist, or bend deformations introduced by the boundaries. PBOEs are the most compact and efficient way to structure light as compared to the other methods described in Sec. 1.2.2, and operate on the principle of *geometric phase*, which Pancharatnam and Berry are credited for formulating. A geometric phase is a global phase which has been acquired through a cyclic adiabatic process [49–51]. Here, if a polarization state undergoes a cyclic polarization transformation along a closed path on the Poincaré sphere, then the geometric phase acquired is half the solid angle enclosed by the path. For example, right-circularly polarized light \mathbf{A}_R will always be transformed to left-circularly polarized light \mathbf{A}_L by a half-wave plate no matter its optical axis angle, and the state traces a path from the north to the south pole of the PS. However, which path it follows in relation, determined by the HWP angle Φ , in relation to HWP_0 will affect what global phase is picked up. In the right-left circular basis $\{\hat{\mathbf{r}}, \hat{\mathbf{l}}\}$, we can see precisely this varying global phase,

$$\begin{bmatrix} \hat{\mathbf{r}} \\ \hat{\mathbf{l}} \end{bmatrix} \xrightarrow{\text{HWP}_\Phi} \begin{bmatrix} \hat{\mathbf{l}}e^{+i2\Phi} \\ \hat{\mathbf{r}}e^{-i2\Phi} \end{bmatrix} \quad (2.9)$$

So the angle of the optical axis translates directly to a global phase acquired. In this way, if we can construct a half-wave plate with a spatially varying optical axis $\Phi(\mathbf{r}_\perp)$, where \mathbf{r}_\perp is the transverse spatial coordinates, then we can imprint the phase $\pm i2\Phi(\mathbf{r}_\perp)$ on circularly polarized light. For example, if $\Phi(r, \phi) = \ell\phi/2 + \Phi_0$, then we can generate modes with OAM value $\pm\ell$; Φ_0 is an offset angle at $\phi = 0$. This is the concept of the PBOEs known as q -plates, where $q = \ell/2$ is the topological charge of the plate, see [52] for a history and review of q -plates. While q -plates are primarily fabricated using nematic liquid crystals for their ease of alignment and tunability, plasmonic and ultra-thin metasurfaces have also been demonstrated [46, 53]. For liquid crystals with phase retardation of $\Gamma(V)$, and V is

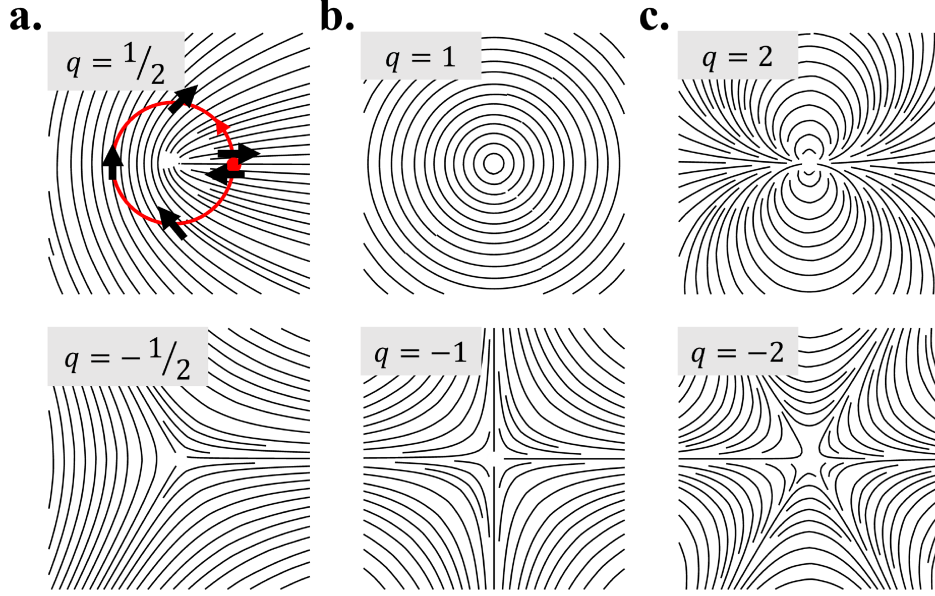


Figure 2.4: **q -plate patterns.** The optical axis distributions for topological charges a. $q = \pm 1/2$, b. $q = \pm 1$, and c. $q = \pm 2$. The topological charge is determined by the number of times (half-integer or integer) that the local axis turns about the center singularity, as shown by going around the red circle. NB: Line discontinuities are plotting artifacts; only the center singularities have an undefined axis.

an externally applied voltage, the action of a PBOE in the circular basis is [54],

$$\begin{bmatrix} \hat{\mathbf{r}} \\ \hat{\mathbf{l}} \end{bmatrix} \xrightarrow{PBOE} \cos\left(\frac{\Gamma(V)}{2}\right) \begin{bmatrix} \hat{\mathbf{r}} \\ \hat{\mathbf{l}} \end{bmatrix} + i \sin\left(\frac{\Gamma(V)}{2}\right) \begin{bmatrix} 0 & e^{+i2\Phi(\mathbf{r}_\perp)} \\ e^{-i2\Phi(\mathbf{r}_\perp)} & 0 \end{bmatrix} \begin{bmatrix} \hat{\mathbf{r}} \\ \hat{\mathbf{l}} \end{bmatrix}. \quad (2.10)$$

If the applied voltage is tuned such that $\Gamma(V) = \pi$, then we regain a half-wave plate with spatially varying optical axis $\Phi(\mathbf{r}_\perp)$, and a global phase of $|2\Phi(\mathbf{r}_\perp)|$ is added. The optical axis distribution for q -plates with various topological charges is shown in Fig. 2.4. While these output spatial modes carry OAM, they are not Laguerre–Gauss modes; rather, they are Hypergeometric–Gauss modes [55].

The coupling between polarization to spatial modes is particularly useful for fast switching in applications such as communication (both classical and quantum) since the achievable GHz modulation of input polarization states allows for the GHz modulation of output spatial modes. For tuned q -plates, linear polarization input states results in vector vortex beams; in particular, $q = 1/2$ plates produce radially and azimuthally polarized beams.

Chapter 3

Non-Symmetric Inhomogeneous Liquid-Crystal Devices

As per the name of this thesis, we are no longer dealing with the simple configuration of symmetrically patterned PBOEs. In this chapter, we will consider the case where there is a relative angle between the front and back walls, resulting in a twisted nematic liquid-crystal (TNLC) cell. While the underlying mathematics of light propagating in twisted anisotropic media is well known—see for example Chapter 5 in [44]—the implications for spatially varying non-symmetric LC (NS-LC) devices has not been analyzed in detail. In particular as I will show, if the overall phase retardation can be varied, then we gain the ability to toggle between different spatial polarization transformations that are not accessible with symmetrically patterned PBOEs. These *dual-plates* have promising applications, for example, multi- q -plates and tunable lenses.

3.1 Twisted nematics

Let's begin by deriving the Jones matrix for a TNLC cell of thickness d , total twist angle α , and phase retardation $\Gamma = 2\pi(n_e - n_o)d/\lambda$, with the extraordinary and ordinary refractive indices given by n_e and n_o , respectively. This formulation is expressed in the horizontal-vertical polarization basis $\{\hat{\mathbf{x}}, \hat{\mathbf{y}}\}$. Without loss of generality, we assume that the front layer of the cell is aligned along the x-axis at 0° , and the back layer is aligned counter-clockwise at α ; the intermediate twisting is slow and thus is assumed to be linearly dependent on propagation distance. We will show in Sec. 4.2.1 that this indeed the case. This

configuration, as shown in Fig. 3.1a, can be modeled as a stack of N thin waveplates, each possessing a phase retardation of Γ/N ; the fast axis of the n^{th} waveplate is oriented at an angle of $n\alpha/N$ ($n = 1, \dots, N$). The total Jones matrix, $\mathbf{T}(\alpha, \Gamma)$, can then be obtained via consecutive matrix multiplication as follows [44],

$$\begin{aligned}\mathbf{T}(\alpha, \Gamma) &= \prod_{n=1}^N \mathbf{R}(-n\alpha/N) \mathbf{W}_0(\Gamma/N) \mathbf{R}(n\alpha/N) \\ &= \mathbf{R}(-\alpha) \{ \mathbf{W}_0(\Gamma/N) \mathbf{R}(\alpha/N) \}^N,\end{aligned}\quad (3.1)$$

where $n = 1$ appears on the right most side of the matrix multiplication, and $\mathbf{R}(\cdot)$ is the rotation matrix,

$$\mathbf{R}(\cdot) = \begin{bmatrix} \cos(\cdot) & \sin(\cdot) \\ -\sin(\cdot) & \cos(\cdot) \end{bmatrix}.\quad (3.2)$$

Here, the Jones matrix for a single waveplate of phase retardation Γ/N with its fast axis along the x-axis is given by,

$$\mathbf{W}_0(\Gamma/N) = \begin{bmatrix} e^{-i\frac{\Gamma}{2N}} & 0 \\ 0 & e^{i\frac{\Gamma}{2N}} \end{bmatrix}.\quad (3.3)$$

In the limit as $N \rightarrow \infty$, Eq. 3.1 has the following closed form,

$$\begin{aligned}\mathbf{T}_0(\alpha, \Gamma) &= \mathbf{R}(-\alpha) \begin{bmatrix} \cos X - \frac{i\Gamma}{2X} \sin X & \frac{\alpha}{X} \sin X \\ -\frac{\alpha}{X} \sin X & \cos X + \frac{i\Gamma}{2X} \sin X \end{bmatrix} \\ &= \mathbf{R}(-\alpha) \mathbf{M}_0(\alpha, \Gamma),\end{aligned}\quad (3.4)$$

with $X = \sqrt{\alpha^2 + (\Gamma/2)^2}$. For the case where the fast axes of the front and back layers are aligned at angles ϕ_f and ϕ_b , respectively, the general twisted matrix, after setting $\alpha = \phi_b - \phi_f$, becomes,

$$\begin{aligned}\mathbf{T}_{\phi_f}(\alpha, \Gamma) &= \mathbf{R}(-\phi_f) [\mathbf{R}(\phi_f - \phi_b) \mathbf{M}_0(\alpha, \Gamma)] \mathbf{R}(\phi_f) \\ &= \mathbf{R}(-\alpha) \mathbf{M}_{\phi_f}(\alpha, \Gamma),\end{aligned}\quad (3.5)$$

where $\mathbf{M}_{\phi_f}(\alpha, \Gamma) = \mathbf{R}(-\phi_f) \mathbf{M}_0(\alpha, \Gamma) \mathbf{R}(\phi_f)$.

Figure 3.1b demonstrates the action of Eq. 3.4, shown on the Poincaré sphere (PS), on a horizontally polarized input for twist angles between $-\pi/2$ and $\pi/2$ at a given birefringence of $\Gamma = \pi$. Recall that the positive (negative) points of the three principal axes $\hat{S}_1, \hat{S}_2, \hat{S}_3$ on the PS correspond, respectively, to horizontal (vertical), diagonal (anti-diagonal), and

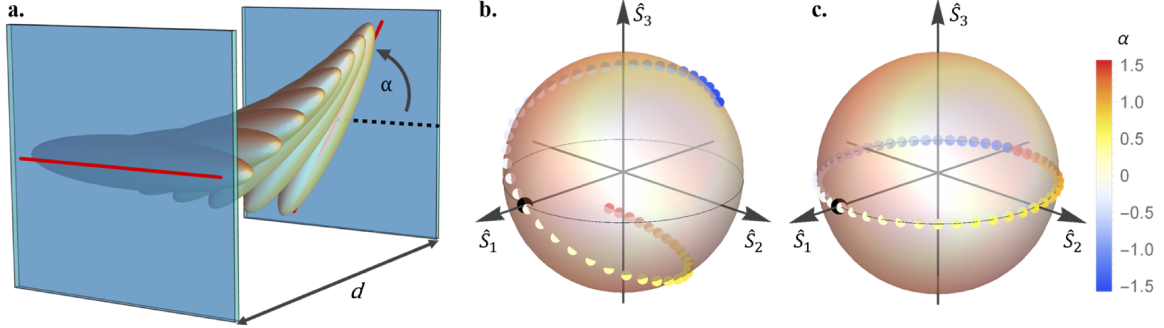


Figure 3.1: **Twisted nematic liquid-crystal cell.** a. Illustration of liquid crystals twisting between two glass plates, uniformly aligned at 0° and α for the front and back layers, respectively, spaced apart by a distance of d . The action of this configuration is shown on the Poincaré Sphere given a horizontally polarized input state (black dot) for varying twist angles α between $-\pi/2$ and $+\pi/2$, with a birefringence of b. $\Gamma = \pi$, and c. $\Gamma = 1001\pi$ in the adiabatic following regime.

left-hand circular (right-hand circular) polarization states. We see that the output state is elliptical, wherein the handedness is determined by the sign of α . Indeed, when the twist is much larger than the incident wavelength of light, i.e., $\alpha \gg \lambda$ —which is the case for visible light—this weak rotation of the polarization, following the twisting, is known as the *Mauguin régime* or *waveguide regime*. This is named after French physicist Charles Mauguin who first observed this twisted nematic effect [56].

An important behaviour to note is that if $\Gamma \gg \alpha$, then $\mathbf{M}_0(\alpha, \Gamma)$ simplifies to $\mathbf{W}_0(\Gamma)$, and Eq. 3.5 becomes,

$$\mathbf{T}_{\phi_f}(\alpha, \Gamma) \approx \mathbf{R}(-\alpha)\mathbf{W}_{\phi_f}(\Gamma), \quad (3.6)$$

where $\mathbf{W}_{\phi_f}(\Gamma) = \mathbf{R}(-\phi_f)\mathbf{W}_0(\Gamma)\mathbf{R}(\phi_f)$ is a regular waveplate of retardance Γ with its fast axis oriented at ϕ_f . Consequently, an input beam that is linearly polarized either parallel or orthogonal to ϕ_f will simply be rotated by α in the counterclockwise direction. This is referred to as *adiabatic following*, and can be achieved by either having very birefringent liquid crystals with large Δn or by constructing a thick cell with large enough d . Figure 3.1c demonstrates this behaviour for a horizontally polarized input state for a range of twist angles, wherein the output states were calculated via Eq. 3.4 with $\Gamma = 1001\pi$. We see that the horizontal input—parallel with the input alignment layer—is rotated by α through to other linear states along the equator of the PS.

Let us further examine the behaviour of TNLCs in the adiabatic following regime. Recall, while we have in this case that $\Gamma \gg \alpha$, the effective phase retardation is Γ modulo

2π . We thus observe that Eq. 3.6 simplifies further for two cases: $\Gamma(\text{mod}2\pi) = 0$ and $\Gamma(\text{mod}2\pi) = \pi$. For $\Gamma(\text{mod}2\pi) = 0$, $\mathbf{W}_{\phi_f}(0)$ reduces to the identity matrix, leaving,

$$\mathbf{T}_{\phi_f}(\alpha, 0) = \begin{bmatrix} \cos \alpha & -\sin \alpha \\ \sin \alpha & \cos \alpha \end{bmatrix}. \quad (3.7)$$

Left-handed (L) and right-handed (R) circular polarizations are invariant under rotations, save for a phase, so explicitly acting this on the circular basis yields $\{|L\rangle, |R\rangle\} \rightarrow \{e^{-i\alpha}|L\rangle, e^{i\alpha}|R\rangle\}$. We have adopted bra-ket notation to denote the complex polarization spinor. For the case where $\Gamma(\text{mod}2\pi) = \pi$, Eq. 3.6 simplifies to,

$$\mathbf{T}_{\phi_f}(\alpha_\pi, \pi) = \begin{bmatrix} \cos \alpha_\pi & \sin \alpha_\pi \\ \sin \alpha_\pi & -\cos \alpha_\pi \end{bmatrix}, \quad (3.8)$$

with $\alpha_\pi = \phi_b + \phi_f$. This is precisely the Jones matrix for a half-wave plate oriented at $\alpha_\pi/2$, yielding $\{|L\rangle, |R\rangle\} \rightarrow \{e^{i\alpha_\pi}|R\rangle, e^{-i\alpha_\pi}|L\rangle\}$. Of course, we can also consider the case for an arbitrary Γ . Eq. (3.6) can be rewritten out explicitly to be,

$$\mathbf{T}_{\phi_f}(\alpha, \Gamma) = \frac{1}{2} \left((1 + e^{i\Gamma})\mathbf{T}_{\phi_f}(\alpha, 0) + (1 - e^{i\Gamma})\mathbf{T}_{\phi_f}(\alpha_\pi, \pi) \right). \quad (3.9)$$

We see that the general case is a superposition of the cases when $\Gamma(\text{mod}2\pi) = 0$ and $\Gamma(\text{mod}2\pi) = \pi$, and the relative phases and amplitudes are determined by the birefringence.

Let's now extend this analysis to the spatially varying case of TNLC plates by letting the fast axis orientations of the front and back plates have spatial distributions $\Phi_f(r, \varphi)$ and $\Phi_b(r, \varphi)$, respectively, in cylindrical coordinates. Then an incident circularly polarized beam will pick up a spatially varying phase proportional to either $\alpha(r, \varphi) = \Phi_b(r, \varphi) - \Phi_f(r, \varphi)$ or $\alpha_\pi(r, \varphi) = \Phi_b(r, \varphi) + \Phi_f(r, \varphi)$, i.e. the difference or sum of the two fast axis distributions, depending on if $\Gamma(\text{mod}2\pi) = 0$ or $\Gamma(\text{mod}2\pi) = \pi$. Therefore, we can use the birefringence of such a *dual-plate* to toggle between two different behaviours. Of course, we could also consider the inverse problem wherein we desire a particular twist distribution; in this case, $\Phi_b = (\alpha_\pi + \alpha)/2$ and $\Phi_f = (\alpha_\pi - \alpha)/2$. Note that for a given dual-plate if the front and back layers are reversed—i.e. the orientation of the plate is flipped, or the beam enters from the back—a distinct third phase pattern could potentially be acquired at $\Gamma(\text{mod}2\pi) = 0$, defined by $\alpha^{-1} = \Phi_f - \Phi_b = -\alpha$.

One potential challenge that arises when dealing with non-symmetric liquid-crystal (NS-LC) devices is that nematic liquid-crystals are assumed to only favourably twist between $-\pi/2$ and $\pi/2$. For example, if $\phi_f = \pi/8$ and $\phi_b = 7\pi/8$, then $\alpha = -\pi/4$, and not $3\pi/4$, in order to achieve the lowest possible twist. At locations where ϕ_f and ϕ_b are orthogonal,

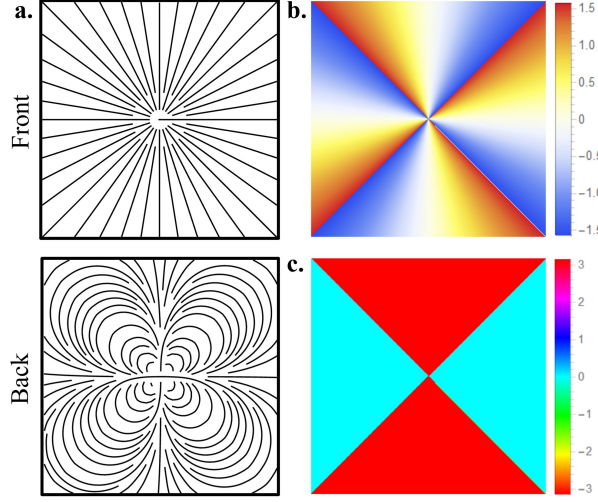


Figure 3.2: **Example of multi- q -plate.** a. Disclination patterns for the front ($\Phi_f(\varphi) = \varphi$) and back ($\Phi_b(\varphi) = 3\varphi$) alignment layers. b. The resulting twist distribution $\alpha(\varphi) = 2\varphi$. c. The induced global phase distribution with phase jumps located where the twist distribution could be either $\pm\pi/2$.

there is an ambiguity as to whether $\alpha = +\pi/2$ or $-\pi/2$. This leads to discontinuities in the twist distribution, which results in π phase jumps appearing in these locations. Consequently, a spatially varying phase distribution, $\Phi_\alpha(r, \varphi)$, will be imparted to any input beam, regardless of the birefringence setting, such that $\mathbf{E}_{\text{out}} = e^{iG} e^{i\Phi_\alpha(r, \varphi)} \mathbf{T}_{\phi_f}(\alpha, \Gamma) \mathbf{E}_{\text{in}}$. Unlike uniform global phases e^{iG} which can be safely ignored when manipulating light—except for interferometry—this kind of spatially varying phase distribution cannot be ignored as it can lead to unstable propagation unless dealt with appropriately. A phase plate, for example, with the inverse phase distribution can be placed after the NS-LC plate to remove the global phase, and since the global phase distribution is independent of Γ , the phase plate is a static addition to an experimental setup.

3.2 Dual-plates

The key behaviour of a properly constructed NS-LC plate is its dual functionality depending on either the orientation of the plate, or the effective phase retardation. Here are a couple of possible applications of what I will class as *dual-plates*.

Multi- q -plate: Recall that the functionality of a q -plate is equivalent to that of a

half-wave plate with a fast axis distribution of $\Phi_{\text{QP}}(\varphi) = q\varphi + \varphi_0$, where q , the topological charge of the plate, is either a full or half-integer, and φ_0 is the offset angle. Its Jones matrix is identical to Eq. (3.8) with $\alpha_\pi = 2\Phi$, and a circularly polarized input will experience spin-to-orbital angular momentum coupling. For example, an input beam with a spin of $+(-)\hbar$ along the axis of propagation will gain $+(-)2q\hbar$ units of orbital angular momentum (OAM), where \hbar is the reduced Planck constant, at the expense of switching the spin to be $-(+)\hbar$. We have adopted the convention that a spin of $+(-)\hbar$ corresponds to left(right) circularly polarized light. This provides a q -plate with the capability to generate a bi-dimensional Hilbert space spanning $\{|R, 2q\rangle, |L, -2q\rangle\}$, where we have used Dirac notation with the labels corresponding to a photon's polarization and OAM, respectively.

However, in order to have access to states created from a $-q$ -plate—thus having access to a four-dimensional Hilbert space—it is necessary to place a half-wave plate, or equivalent device imparting a $\lambda/2$ retardation, after the original q -plate. While this has been shown to be feasible in a practical experiment [14], it can introduce unnecessary issues such as alignment (for half-wave plate) or electronic (or Pockel cell). Additionally, it is impossible to create a q' -plate ($q' \neq \pm q$) from a single q -plate. E.g., a $q=1/2$ -plate cannot re-create the action of a $q=1$ -plate. An appropriately patterned dual-plate is capable of addressing both of these issues. For example, define the front and back distributions to be $\Phi_f(\varphi) = q_f\varphi$ and $\Phi_b(\varphi) = q_b\varphi$, respectively; we have the dropped offset angles without loss of generality. If $q_f = q_b$, we straightforwardly recover the behaviour of a regular $q = q_b$ -plate, so we will assume $q_f \neq q_b$ and we get the following cases.

(1) If $q_f = 0$, then $\alpha = \alpha_\pi = q_b\varphi$, and we lose the dual behaviour of the dual-plate; recall that a topology of zero corresponds to a uniformly linearly aligned fast axis distribution. (2) However, if $q_b = 0$, then $\alpha = -q_f\varphi$ and $\alpha_\pi = q_f\varphi$; we can thus use the birefringence of the dual-plate to toggle between the behaviour of oppositely charged q_f -plates. Of course, we note that cases (1) and (2) are the same dual-plate; however, the orientation of the device—or equivalently, the beam propagation—is reversed. So, while we obtain two distinct behaviours through α and α_π , we do not gain a third behaviour since $\alpha^{-1} = \alpha$ in case (2). (3) In general, if $|q_f|, |q_b| > 0$, then $\alpha \neq \alpha_\pi$ and $\alpha^{-1} \neq \alpha$, thus creating a multi- q -plate with three possible behaviours. Figure 3.2 is an example of a multi- q -plate with $q_f = 1$ and $q_b = 3$, with the respective alignment distributions given in Fig. 3.2a. The resulting twist distribution $\alpha(\varphi)$ and the global phase distribution are shown in Fig. 3.2b and c, respectively.

Lenses: We are of course not limited to fast axis distributions that are purely dependent on the azimuthal angle. Consider, for instance, the phase imparted by a lens, $\Phi_{\text{lens}}(r) = -\pi r^2/f$, where f is the focal length; if f is positive (negative), light will converge (diverge). We can again consider several different cases, and we'll assume $f > 0$ unless otherwise

specified.

(1) Consider the case when $\Phi_f = \Phi_b = \Phi_{\text{lens}}$; then $\alpha = 0$ and $\alpha_\pi = 2\Phi_{\text{lens}}$. Equivalently, we could consider $\Phi_f = -\Phi_b = -\Phi_{\text{lens}}$ to give $\alpha = 2\Phi_{\text{lens}}$ and $\alpha_\pi = 0$. This allows for the ability to toggle between a lensing effect and no lensing effect by changing the effective phase retardation Γ .

(2) If $\Phi_f = 0$ and $\Phi_b = \Phi_{\text{lens}}$, then $\alpha = \alpha_\pi = \Phi_{\text{lens}}$. Note that, while it might appear that we do not have a true dual-plate, we must consider that the sign of the imparted phase is polarization-dependent according to the behaviours of Eq. (3.7) and (3.8). For $\Gamma = 0$, an input polarization state of $|L\rangle$ picks up a phase of $e^{-i\alpha}$, so the output beam will diverge; however, an input of $|R\rangle$ will converge. The opposite scenario occurs when $\Gamma = \pi$, though the handedness of the inputs will be flipped. The dual setting in this case is the ability to switch the sign of a polarization-dependent lens. If the reverse device is considered, i.e. $\Phi_f = \Phi_{\text{lens}}$ and $\Phi_b = 0$, the same essential functionality occurs.

(3) For the general case, suppose $\Phi_f(r) = -\pi r^2/f_f$ and $\Phi_b(r) = -\pi r^2/f_b$, where $f_f \neq \pm f_b \neq 0$ could be either negative or positive. Then we straightforwardly get that α and α_π will impart lensing phases with focal lengths of $f_f f_b/(f_f - f_b)$ and $f_f f_b/(f_f + f_b)$, respectively. Depending on the signs and magnitudes of f_f and f_b , the overall lens for the two functionalities might be either converging or diverging. From a design perspective, it is more practical to consider the inverse problem such that $\alpha(r) = -\pi r^2/f_0$ and $\alpha_\pi(r) = -\pi r^2/f_\pi$, where f_0 and f_π are the desired effective polarization-dependent focal lengths obtained at $\Gamma = 0$ and $\Gamma = \pi$, respectively. This in turn gives that the lens phases of the front and back distributions have focal lengths of $f_0 f_\pi/2(f_0 - f_\pi)$ and $f_0 f_\pi/2(f_0 + f_\pi)$, respectively. It may be possible to create a thin LC optical element with a variable focal length by changing the phase retardation, i.e., programmable lenses.

Arbitrary phases: The same game can be played for any phase distribution. Indeed, we are not even limited to Φ_f and Φ_b being of the same class of phases—we could mix and match to create a dual-functionality, dual-setting device. This is the beauty of dual-plates.

3.3 Fabrication and characterization

Let us now describe the fabrication of dual plates; indeed, the process is similar to that for symmetric PBOEs [27]. First, we start with two glass substrates, each with a conductive layer of indium tin oxide (ITO). A drop of an azobenzene-based dye (PAAD-22, provided by BEAM Co) is deposited on top of the ITO; the sample is then spin coated for 30 s at 4000 rpm, and baked at 120° for 5 minutes. When exposed to light of a wavelength around

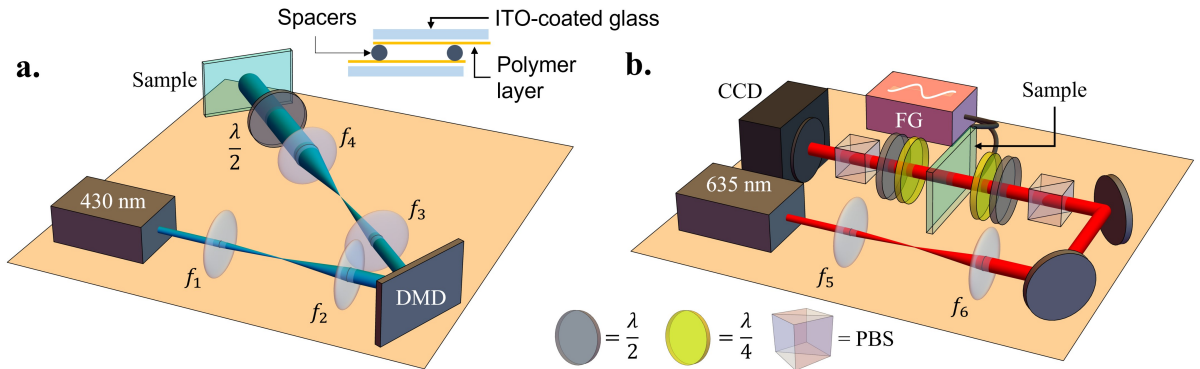


Figure 3.3: **Experimental setups** a. Setup to pattern the glass plates for fabricating liquid-crystal devices. The inset shows the cross-section of the constructed LC cell b. Setup to characterize the fabricated samples. DMD = digital micromirror device, PBS = polarizing beamsplitter, FG = function generator.

the peak of the azodye’s absorption spectrum, the molecules will photoalign themselves according to the light’s linear polarization. Here, we use a 430-nm laser, Fig. 3.3a shows the setup to pattern the sample. In particular, a digital micro-mirror device (DLP3000 DLP® 0.3 WVGA Series 220 DMD) is programmed to reflect a tailored intensity pattern. The resolution of the DMD is 608x684 with a micromirror pitch of $7.6 \mu\text{m}$. A HWP can then be rotated to adjust the polarization to the required orientation.

When fabricating symmetric PBOEs, the two glass substrates are first glued together—with spacers between them to create a uniform cavity for the liquid crystals—and then the sample is exposed with the desired pattern. For non-symmetric PBOEs, each substrate is separately exposed with the front and back plate patterns, respectively; then they are glued together, taking care to overlap the two patterns as best as possible by hand. For the samples presented here, silica microspheres with diameters between $32 \mu\text{m}$ and $38 \mu\text{m}$ are used as the spacers. Note, the two substrates are glued with a lateral offset such that wires can be soldered to the conductive ITO layer; this will allow for a voltage to be applied across the sample. Finally, the nematic liquid crystals (here, 6CHBT) are injected into the cavity and the remaining sides are sealed off with glue. The completed sample is heated to $\sim 100^\circ\text{C}$ on a hot plate and cooled to room temperature once more to cement the alignment of the liquid crystals with the written patterns.

Of course, there is the challenge of how to align the two plates when they each possess a non-zero topology, e.g. $q=1$ and $q=2$, and the alignment of their singularities is critical. The first issue is that, without any sort of markers, the exact position of the singularities

cannot be ascertained by visual inspection of the ITO glasses alone. They are only visible once liquid crystals are inserted between them, and the sample is placed between polarizers. This issue is rectified by placing a small droplet of liquid crystals on the patterned side of one plate, and rigging the unassembled sample between crossed polarizers. The second issue is then the physical alignment and subsequent gluing of the two plates. The simplest and most brute-force method—albeit with the least control of precision—is to align the plates by hand and by eye.

This was achieved by taping a linear polarizer on a light box—identical to those used for drawing and crafts—then one plate (pattern side up) was mounted above the first polarizer. Next, the spacers and a small amount of LCs are placed on the plate, followed by the second ITO plate (pattern side down). The researcher may then wear 3D glasses—wherein the plastic in each eyepiece has been reversed so that the linear polarizer is first, assuming the glasses are of the modern variety—or if these are unavailable, they may tape a linear polarizer over one eye or on their prescription lenses. This allows the researcher viewing ease and movement flexibility while carefully positioning the top plate on the bottom. Due to the spherical nature of the spacers, they tend to act like ball bearings, in such a way that the top plate rolls over the bottom far too easily, making it difficult to retain in one place for proper alignment. One remedy is to apply the super glue to the edge where the lateral offset will be and align while it dries, as it becomes tacky, easier to hold the plates in place, and make small adjustments. Time is of the essence in this scenario, with a complete drying time around 10–15 min for the fast-setting variety of Gorilla glue multi-purpose epoxy adhesive.

The setup to characterize the fabricated sample is shown in Fig. 3.3b. A red 635-nm diode laser is used to illuminate the sample; it is expanded using a telescoping lens system to completely cover the patterned area. A polarizing beamsplitter (PBS), HWP, and QWP are used to prepare the input polarization state. A second set of QWP, HWP, and PBS is used to project the output polarization state from the sample onto a different polarization state. Another telescoping lens system (not shown) is used to image the sample plane and shrink the beam down to fit onto a CCD camera in order to record the intensity measurement. Polarization state tomography is thus performed for the six cardinal polarizations as inputs on the sample. This consists of projecting the output polarization state onto the six cardinal states and recording the intensity or the result using the CCD camera; i.e., there are 6 measurements for each input state, for 36 measurements (images) total per configuration of the sample. The waveplate angles for the six measurement set are tabulated Table 3.1.

As we see from Eq. (1.23)–(1.25), the intensity difference of each polarization pair gives precisely the corresponding Stokes parameter on the Poincaré sphere. The polarization ellipse can then be reconstructed using Eq. 1.26 and 1.27.

Table 3.1: Waveplate settings for polarization tomography

Waveplate	\mathbf{A}_H	\mathbf{A}_V	\mathbf{A}_D	\mathbf{A}_A	\mathbf{A}_R	\mathbf{A}_L
QWP	0°	0°	45°	45°	45°	45°
HWP	0°	45°	22.5°	-22.5°	0°	45°

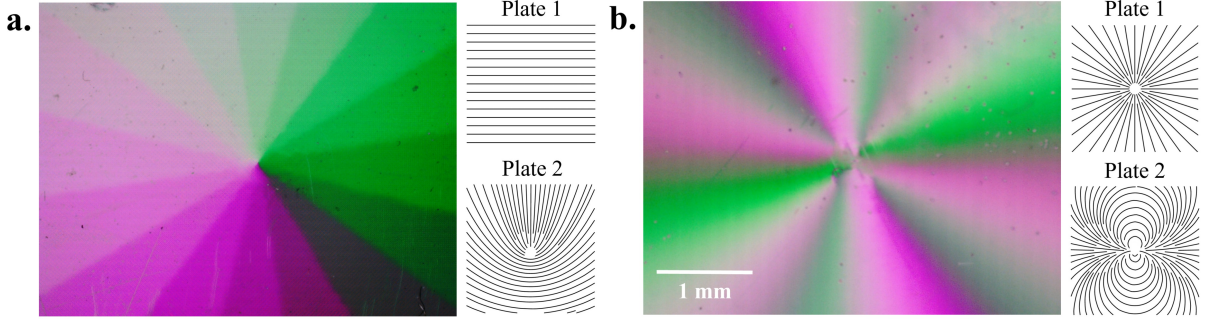


Figure 3.4: **Fabricated samples.** False colour images of a. discretized DP(0,1/2), and b. DP(1,2) between crossed polarizers under a microscope illuminated with white light. The topological patterns on each glass plate is also shown. Note that the $q = 1/2$ pattern is discretized into 16 slices for the patterning process.

3.4 Experimental results and discussion

To explore the validity of the TNLC model, several dual-plates (DP) were fabricated. The first DP fabricated was a discretized DP(0,1/2) with $\sim 35 \mu\text{m}$ spacers, where the labels are the topologies of the front and back plate. Of course, DP(1/2,0) is physically the same sample but the side that light is incident on is reversed. Fig. 3.4a is an image of the fabricated sample through crossed polarizers. The $q = 1/2$ topology was discretized into 16 slices such that a range of twist angles from $[-90^\circ, 90^\circ]$ can be characterized with enough room in each slice to average imperfections from the assemblage. Since the pattern on one plate is uniform, the tedious process of aligning singularities did not have to be done. The second sample type fabricated and tested was a DP(1,2), shown in Fig. 3.4b. The fabrication process for this sample required the careful alignment of the $q = 1$ and $q = 2$ singularities, as described in the previous section. We can see that the two singularities are not quite overlapped, but this is to be expected for eyeballing the alignment.

Let's begin with the experimental results of the discretized DP(0,1/2) sample, which were taken using a 635 nm diode laser. The reconstructed polarization distributions for the orientations DP(0,1/2) and DP(1/2,0) are presented in Fig. 3.5 and Fig. 3.7, respectively.

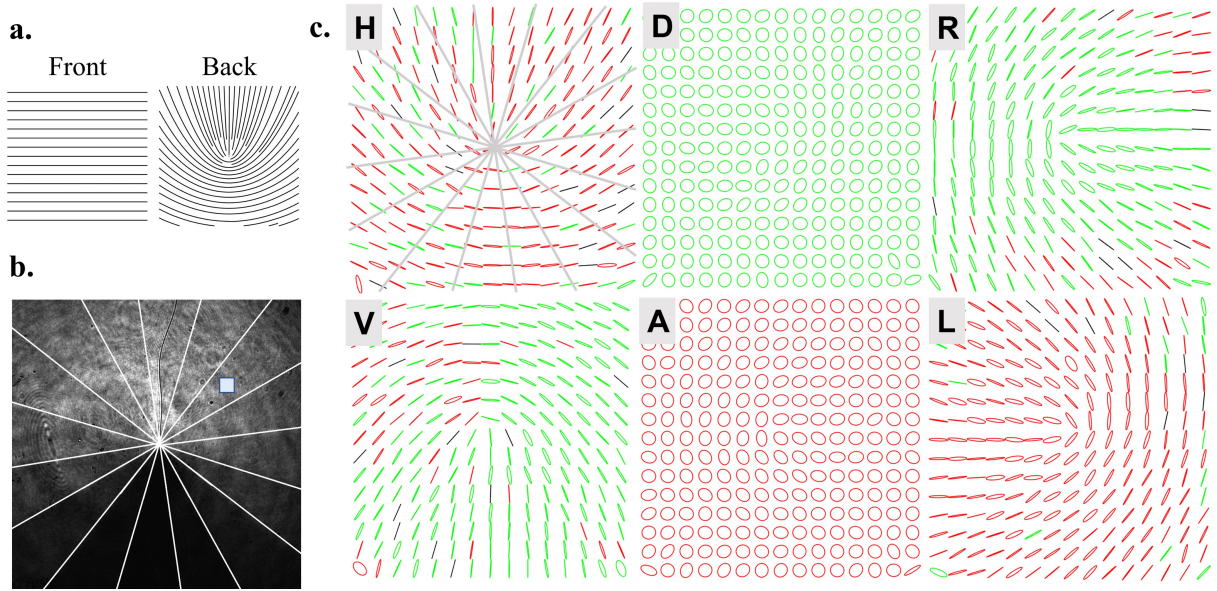


Figure 3.5: **Polarization tomography of discretized DP(0,1/2)**. a. Alignment patterns on the front and back glass plates. b. Example of recorded intensity distribution for an input of \mathbf{A}_H projected on \mathbf{A}_V . The white lines denote the border between each slice, and the small blue square is an example area over which the output polarization is averaged. c. Reconstructed output polarization ellipse distributions for the six cardinal input polarizations. Green = right-hand elliptical ($S_3 > 0$); red = left-hand elliptical ($S_3 < 0$); black = linear ($S_0 = 0$).

The corresponding Poincaré sphere visualizations of this data, along with theoretical fits are given respectively in Fig. 3.6 and Fig. 3.8. The experimental Stokes vectors plotted are the average values in each slice of the discretized sample; the 101×101 pixels which are averaged over are chosen to avoid any major defects present in the sample. Defects and imperfections are to be expected from the inherent ‘hand-made’ nature of the fabrication process. One defect that is inevitably present is the discontinuity line that appears in the slice that has twist angle $|\alpha| = 90^\circ$, caused by the ambiguity of whether the liquid crystals twist $+90^\circ$ or -90° . As can be seen in the intensity images of Fig. 3.5b and Fig. 3.7b, this ‘line’ wanders within the top slice, presumably perturbed into this squiggle by surface defects and spacers in the bulk. During the fabrication process, this line can be observed to evolve and settle into place during the final heating and cooling step if the sample is placed between crossed polarizers.

The diameters of the spacers used range from $32\text{--}38 \mu\text{m}$, with an average of $35 \mu\text{m}$. This

gives our sample an average phase retardation of $\Gamma_{avg} = 51.7$ for 6CHBT liquid crystals with $\Delta n = 0.151$. This Γ_{avg} was used when plotting the theoretical fits using the TNLC Jones matrix $\mathbf{T}_{\phi_f}(\alpha, \Gamma)$ of Eq. 3.5 in Fig. 3.6b and Fig. 3.8b. As a measure of good fit, the average state overlap across all twist angles for a given input polarization is used, where the overlap of each state is calculated as $|\mathbf{S}_{exp} \cdot \mathbf{S}_{TNLC}|^2$. The uncertainties on each average Stokes vector are the standard deviations from the 101×101 ensembles used for averaging, see Appendix A for the exact values. The theoretical fits using $\Gamma_{avg} = 51.7$ imitates the experimental data for all input polarizations and the two orientation cases very well, with total average fits of 89% and 87% for DP(0,1/2) and DP(1/2,0), respectively.

The important behaviour to note here is that we are almost in the adiabatic following regime when $\Gamma \gg \alpha$. If we are in the adiabatic following regime, we would see that a horizontal/vertical input on DP(0,1/2) would be rotated into another linear polarization state dictated by the twist angle. As we can see from the average Stokes vectors plotted for H and V inputs shown in Fig. 3.6b, there is a slight deviation from linear outputs, which the uncertainties given in Appendix A do not make up for. Without access to a different type of nematic liquid crystals, slightly larger spacers could be used in the fabrication process to reach the adiabatic following regime. A sample using 300 μm spacers was attempted, but this appeared to be too thick as the liquid crystals in the bulk were fluid and not anchored by the boundary conditions.

The experimentally reconstructed and theoretically expected polarization distributions for DP(1,2) and DP(2,1) are presented in Fig. 3.9 and Fig. 3.10, respectively. A phase retardation of $\Gamma_{fit} = 52.4$ was used for the theoretical distributions to give the best visual fits. An offset angle of $\sim 15^\circ$ between the front and back patterns was also introduced to account for the glass plates being glued slightly rotated with respect to one another—one of the difficulties encountered while aligning the pattern singularities in the fast drying time of the glue. The effect of this offset angle is that the total polarization patterns are slightly rotated, but this is reproduced well with the theoretical model. Misalignment between the two pattern singularities was not included in the theoretical fits; however, it appears that the physical misalignment was small enough to not affect the overall polarization distributions. Note that the messy distributions along the top and bottom edges of the experimental data is due to permanent ink in those regions which were used to denote the pattern border during fabrication. These ink borders are not visible in Fig. 3.4b as the image is a zoomed-in version to show the misaligned singularities.

All of the experimental data shown so far was taken with no externally applied electric field, i.e., voltage. As mentioned in Sec. 3.3, wires were soldered onto the exposed ITO layer of each glass plate, which can be connected to a function generator. A typical waveform that is generated is a sine wave with 4 kHz frequency and peak-to-peak voltages between $V_{pp} =$

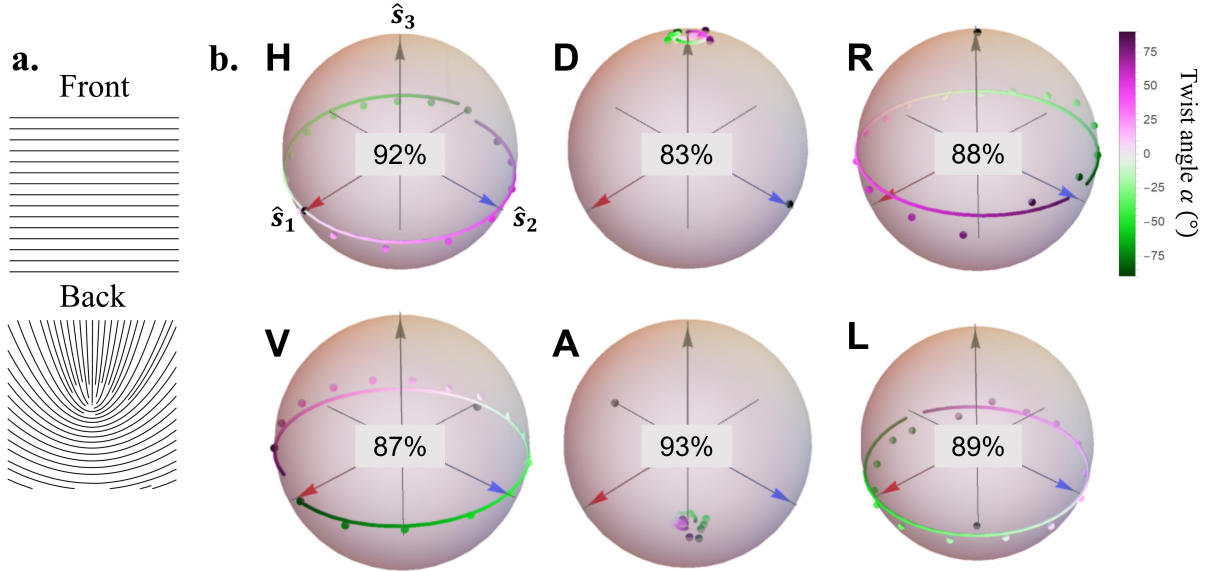


Figure 3.6: **Stokes vectors of discretized DP(0,1/2)**. a. Alignment patterns on the front and back glass plates. b. Reconstructed average Stokes vectors in each of the 16 slices (coloured points) for the cardinal input states (black points), and theoretical fit (line) using the TNLC Jones matrix with $\Gamma_{\text{fit}} = 51.7$. Percentages are the average state overlap with all 16 average Stokes vectors.

0 V and 20 V. Polarization tomography data was also collected for a horizontally polarized 635-nm input beam incident on the discretized DP(0,1/2), and continuous DP(1,2) samples in both orientations. However, a major issue was encountered when trying to reproduce the reconstructed polarization distributions using Eq. 3.5 by only varying Γ : it is impossible. For symmetric PBOEs where the front and back patterns are identical, the assumption that is usually adopted without consequence is that varying the voltage applied to the sample will simply vary the effective phase retardation as the liquid crystals tilt with the applied field, allowing the user to tune and detune the overall effect. Unfortunately, it appears for twisted samples that this assumption cannot be naïvely made. In particular, we may no longer be able to assume a linear twist model when formulating our TNLC Jones matrix, on top of the fact that the liquid crystals now tilt with the field.

In order to determine the true tilt and twist distributions within a non-symmetric PBOE, along with their effect on polarized light, it is necessary to do a deep dive into the elastic continuum theory first developed by de Gennes. Down the rabbit hole, we go.

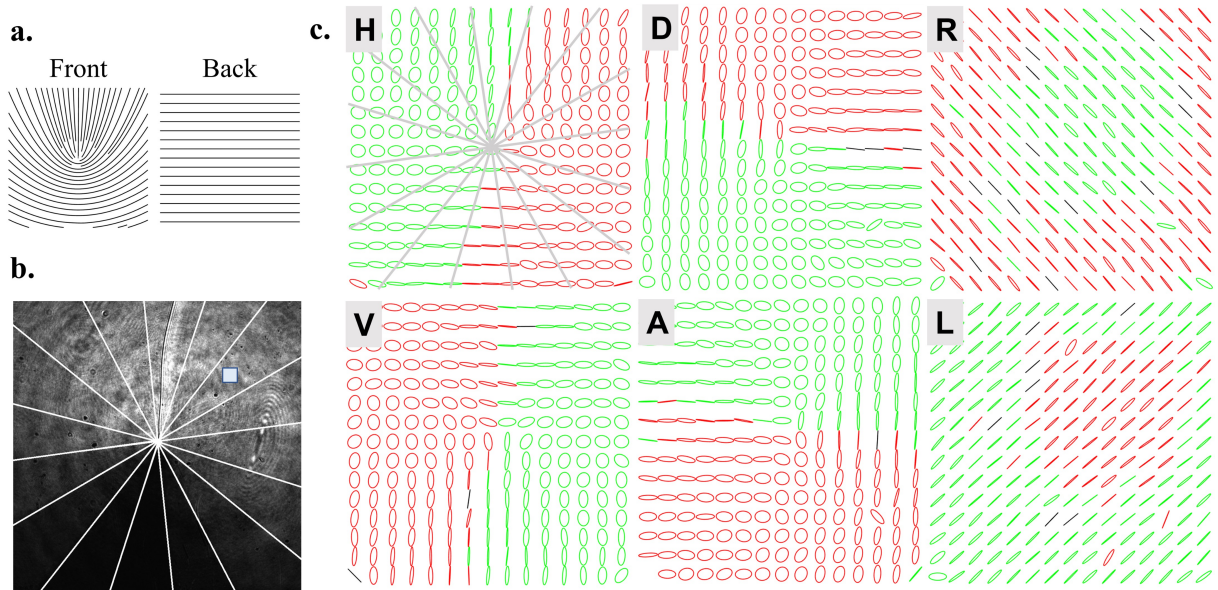


Figure 3.7: **Polarization tomography of discretized DP(1/2,0)**. a. Alignment patterns on the front and back glass plates. b. Example of recorded intensity distribution for an input of \mathbf{A}_H projected on \mathbf{A}_V . The white lines denote the border between each slice, and the small blue square is an example area over which the output polarization is averaged. c. Reconstructed output polarization ellipse distributions for the six cardinal input polarizations. Green = right-hand elliptical ($S_3 > 0$); red = left-hand elliptical ($S_3 < 0$); black = linear ($S_0 = 0$).

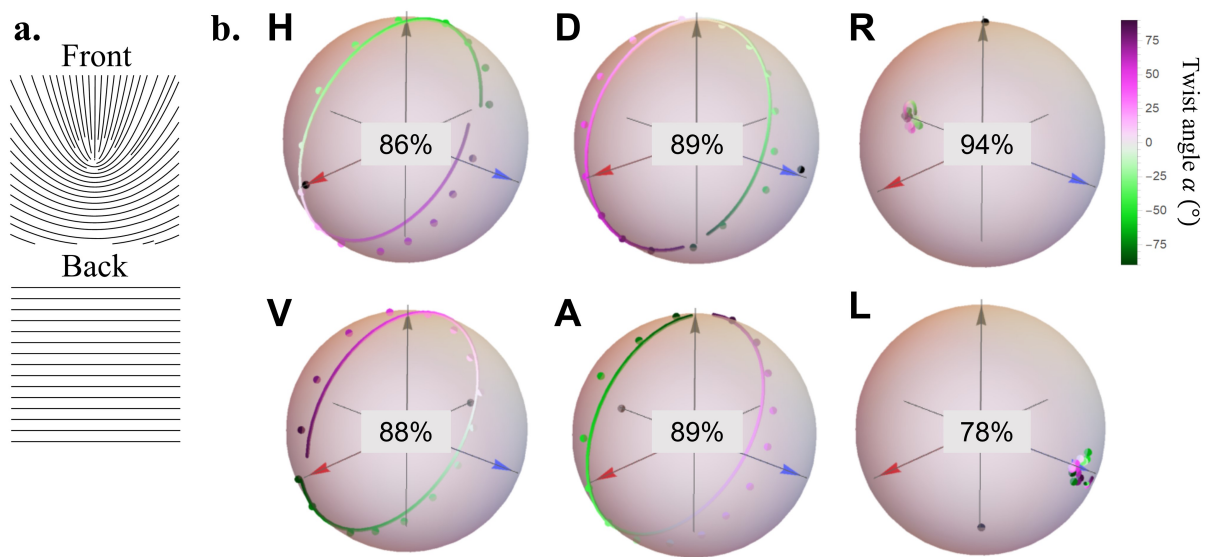


Figure 3.8: **Stokes vectors of discretized DP(1/2,0)**. a. Alignment patterns on the front and back glass plates. b. Reconstructed average Stokes vectors in each of the 16 slices (coloured points) for the cardinal input states (black points), and theoretical fit (line) using the TNLC Jones matrix with $\Gamma_{\text{fit}} = 51.7$. Percentages are the average state overlap with all 16 average Stokes vectors.

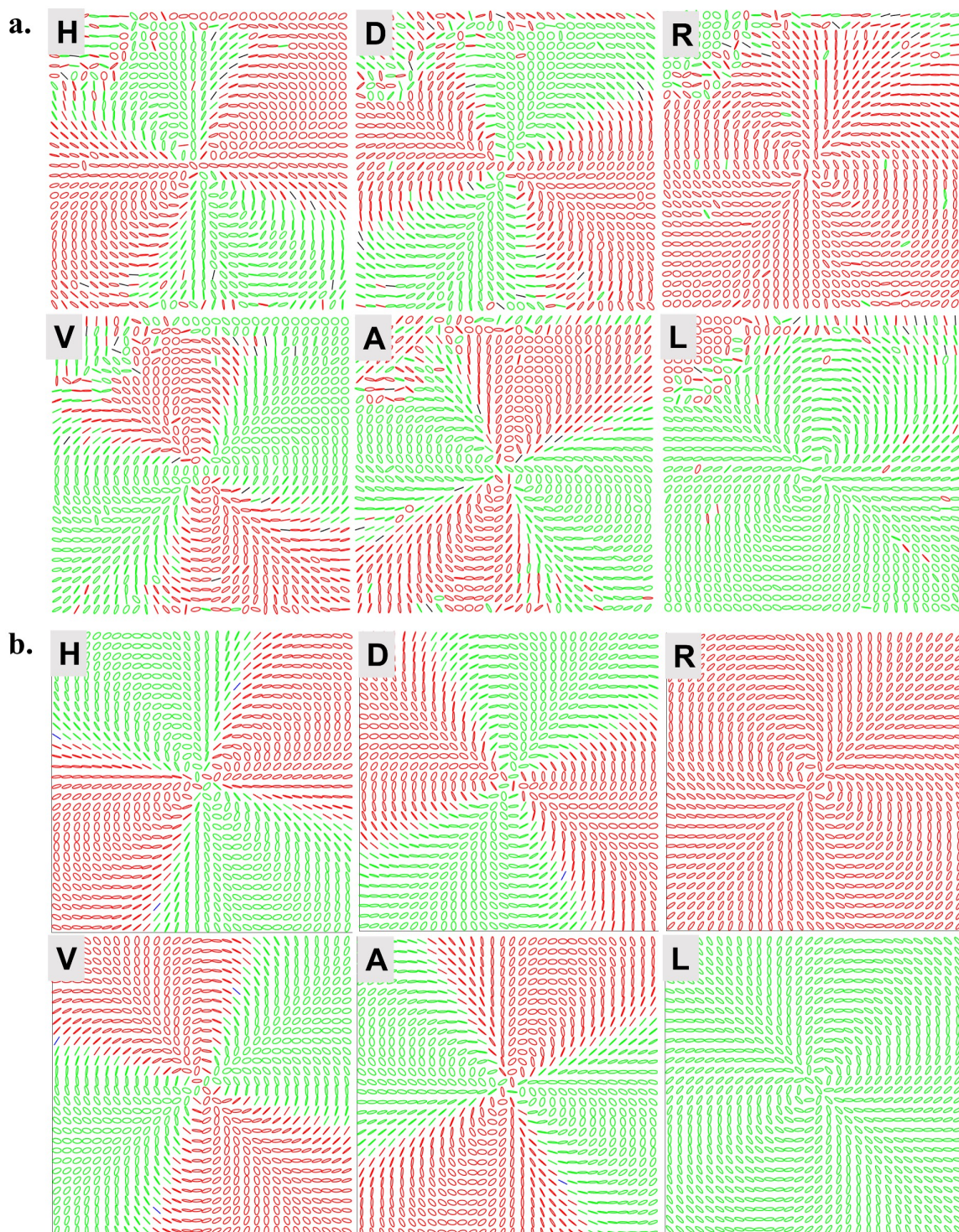


Figure 3.9: **Polarization tomography of DP(1,2)**. a. Reconstructed output polarization ellipse distributions for the six cardinal input polarizations. b. Theoretically predicted polarization distributions with $\Gamma_{\text{fit}} = 52.4$. Green = right-hand elliptical ($S_3 > 0$); red = left-hand elliptical ($S_3 < 0$); black = linear ($S_0 = 0$).

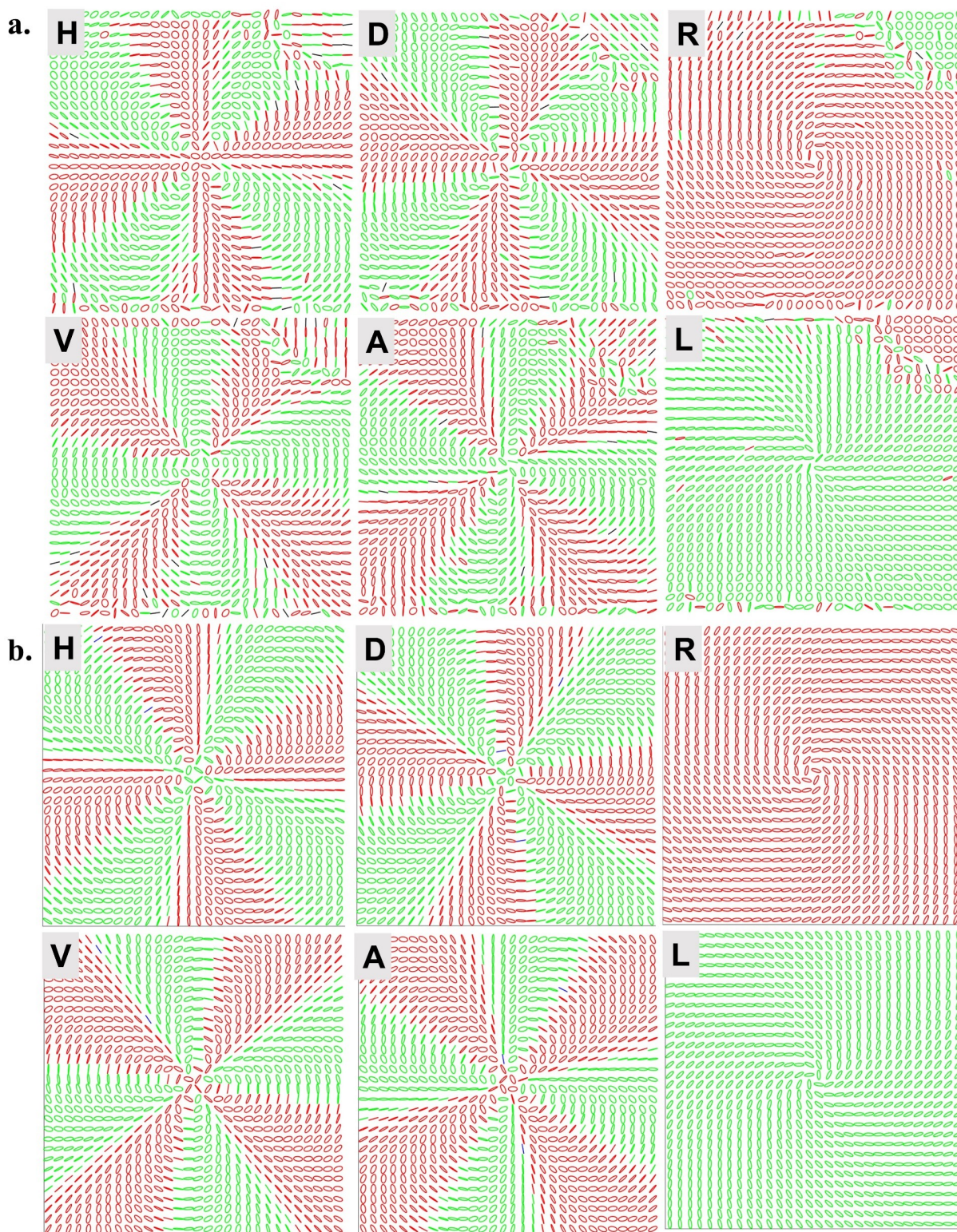


Figure 3.10: **Polarization tomography of DP(2,1).** a. Reconstructed output polarization ellipse distributions for the six cardinal input polarizations. b. Theoretically predicted polarization distributions with $\Gamma_{\text{fit}} = 52.4$. Green = right-hand elliptical ($S_3 > 0$); red = left-hand elliptical ($S_3 < 0$); black = linear ($S_0 = 0$).

Chapter 4

Electric field-induced effects

In this chapter, we extend our TNLC theory of the previous chapter to rigorously include the changes in the tilt and twist distributions of the liquid crystals when an electric field is externally applied. There is unfortunately no convenient analytical solution, so we implement a series of genetic algorithms to numerically calculate the distributions at a range of field strengths. These numerical distributions can then be turned into an approximate Jones matrix of the system in order to compare the experimentally observed effects with the extended model. This is the first time that such an analysis has been carried out in regards to the polarization transformations of an arbitrarily twisted LC cell under the effect of an externally applied field.

4.1 Elastic continuum theory

While many transitional and order behaviours of liquid crystals may be described using molecular theories, there are many other phenomena due to the bulk of the liquid crystals responding to external disturbances. These phenomena are characterized by two properties. Firstly, the energy involved per molecule in producing these effects is small in comparison to the strength of the intermolecular reactions. Secondly, the characteristic distances involved are large in comparison to the molecular dimensions. In this way, liquid crystals may be regarded as a continuous medium with a set of elastic constants. This is referred to as the phenomenological continuum theory for liquid crystals, which has been an excellent way for describing magnetic or electric field-induced effects. This section follows closely the analysis of [4, 57] for the simplified cases of a twisted nematic system under the effect

of an external field, and [58, 59] for the comprehensive case of distorted twist and tilt distributions.

4.1.1 Fundamental equation

As we saw in Sec. 2.2, nematic liquid crystals possess uniaxial symmetry for their orientational order. The axis of uniaxial symmetry is parallel to a unit vector $\hat{\mathbf{n}}$, which we will call the director. Since we are not regarding the liquid crystal bulk on a molecule-by-molecule basis, it is instead useful to partition our macroscopic sample into very small regions. Each region contains a sufficiently large number of molecules such that the long-range orientational order is well defined, and we may characterize it by its director, pointing along the local axis of uniaxial orientational symmetry. The macroscopic sample can then be characterized itself by $\hat{\mathbf{n}}(\mathbf{r})$, the local director at every spatial ‘point’. The equilibrium state, i.e., the state of minimum free energy, for a sample free of disturbances is one where there is parallel alignment of all the local directors. Of course, when we perturb the system by pinning the surface directors to the walls of a container, apply an external field, or introduce thermal fluctuations, then the local directors will no longer remain uniformly aligned, i.e., spatially invariant. Let us define a set of distortion parameters describing the magnitude and nature of the distortions by the first derivative of the local directors with respect to each spatial direction $\partial_i n_j$. The subscripts $i, j = x, y, z$ correspond to the three orthogonal components in the Cartesian coordinate system. For the equilibrium state, clearly, $\partial_i n_j = 0$.

By perturbing the system, the now distorted state will have a higher free energy, with its free-energy density of the form:

$$f_D = f_0 + \Delta f, \quad (4.1)$$

where f_0 is the free-energy density of the equilibrium state, and Δf is a function of potentially n_j and $\partial_i n_j$, which must vanish when all $\partial_i n_j = 0$. Since $\partial_i n_j \ll (\text{molecular dimension})^{-1}$, we may expand Δf as a power series in n_j and $\partial_i n_j$ around $\partial_i n_j = 0$ (the free-energy minimum), keeping only the lowest-order non-vanishing terms. Let this expansion be \mathcal{F}_D , which must have the following properties:

1. Since we are expanding around $\partial_i n_j = 0$, the lowest-order non-vanishing terms are quadratic.
2. The ‘head’ and ‘tail’ of the nematic director represent the same physical state; therefore, \mathcal{F}_D should be even in n_j .

$\Delta\epsilon$	Δn	K_1 [pN]	K_2 [pN]	K_3 [pN]
8.0	0.151	6.7	3.4	10.6

Table 4.1: Material properties of 6CHBT nematic liquid crystals [60].

3. \mathcal{F}_D should be a scalar quantity by nature of it being energy.
4. We may discard any $\nabla \cdot \mathbf{u}(\mathbf{r})$, where $\mathbf{u}(\mathbf{r})$ is an arbitrary vector field, since they are surface contributions to f_D . These are assumed small by Gauss' Theorem.

There are then only three linearly independent terms which satisfy these conditions (see Appendix B.1 for details): $[\nabla \cdot \hat{\mathbf{n}}(\mathbf{r})]^2$, $[\hat{\mathbf{n}}(\mathbf{r}) \cdot \nabla \times \hat{\mathbf{n}}(\mathbf{r})]^2$, and $[\hat{\mathbf{n}}(\mathbf{r}) \times \nabla \times \hat{\mathbf{n}}(\mathbf{r})]^2$. Physically, these three terms correspond to splay, twist, and bend behaviour of the bulk liquid crystals, as was shown in Fig. 2.2. The total distortion-free free-energy contribution of \mathcal{F}_D is then,

$$\mathcal{F}_D = \frac{1}{2} \{ K_1 [\nabla \cdot \hat{\mathbf{n}}(\mathbf{r})]^2 + K_2 [\hat{\mathbf{n}}(\mathbf{r}) \cdot \nabla \times \hat{\mathbf{n}}(\mathbf{r})]^2 + K_3 [\hat{\mathbf{n}}(\mathbf{r}) \times \nabla \times \hat{\mathbf{n}}(\mathbf{r})]^2 \}, \quad (4.2)$$

where the K_i are the Frank elastic constants. Since it is possible to create deformations that are purely splay, twist, or bend, we must have that $K_i > 0$; otherwise, the undistorted, uniformly aligned case would not correspond to a free energy minimum. It is a non-trivial task of calculating the K_i as they serve as the link between the continuum and microscopic theories for a particular composition of liquid crystal. However, an order-of-magnitude estimate can be obtained from dimensional analysis. As it happens, the K_i have units of energy per length. The characteristic energy of our system is the intermolecular energy, which is ~ 0.01 eV; meanwhile, the characteristic length is the separation between two molecules, $\sim 10\text{\AA}$. This gives an order-of-magnitude estimate to be $K \simeq 10^{-12}$ N; measured values have been found to be between 10^{-11} – 10^{-12} N. For the samples fabricated in this thesis, 4-(trans-4-n-hexylcyclohexyl) isothiocyanatobenzoate (6CHBT) nematic liquid crystals were used with material properties tabulated in Table 4.1.

Let's now look at the free-energy contributions from an externally applied electric (\mathbf{E}) or magnetic field (\mathbf{H}). Since liquid crystal molecules are, in general, electrically polarizable, diamagnetic, and anisotropic in their electric/magnetic properties, an applied field will cause the molecules to align, and contribute a free-energy density opposite in sign to f_D . The free-energy density contribution of an applied electric or magnetic field is [4, 61],

$$\mathcal{F}_E = -\frac{1}{2} \mathbf{D} \cdot \mathbf{E}, \quad \mathcal{F}_M = -\frac{1}{2} \mathbf{B} \cdot \mathbf{H}, \quad (4.3)$$

$$D_i = \epsilon_0(\epsilon_{\perp} E_i + \Delta\epsilon n_i n_j E^j), \quad (4.4)$$

$$B_i = \mu_0(\chi_{\perp} H_i + \Delta\chi n_i n_j H^j), \quad (4.5)$$

where ϵ_0 and μ_0 are the permittivity and permeability of free-space, respectively, and summation is performed on repeated indices. Here, ϵ_{\parallel} (ϵ_{\perp}) denote the dielectric constant per unit volume that is parallel (perpendicular) to the local director, such that $\Delta\epsilon \equiv \epsilon_{\parallel} - \epsilon_{\perp}$; χ_{\parallel} (χ_{\perp}) denote the diamagnetic susceptibility per unit volume that is parallel (perpendicular) to the local director, such that $\Delta\chi \equiv \chi_{\parallel} - \chi_{\perp}$. The complete formulation for the fundamental equation of the elastic continuum theory is thus,

$$\begin{aligned} \mathcal{F} &= \mathcal{F}_D + \mathcal{F}_E + \mathcal{F}_M \\ &= \frac{1}{2} \{ K_1 [\nabla \cdot \hat{\mathbf{n}}(\mathbf{r})]^2 + K_2 [\hat{\mathbf{n}}(\mathbf{r}) \cdot \nabla \times \hat{\mathbf{n}}(\mathbf{r})]^2 + K_3 [\hat{\mathbf{n}}(\mathbf{r}) \times \nabla \times \hat{\mathbf{n}}(\mathbf{r})]^2 - \mathbf{D} \cdot \mathbf{E} - \mathbf{B} \cdot \mathbf{H} \}. \end{aligned} \quad (4.6)$$

And the total free energy of our sample is then simply the integral of \mathcal{F} over its volume,

$$F = \int_{\mathcal{V}} \mathcal{F} d^3r. \quad (4.7)$$

For any given configuration of distortions and applied fields, the name of the game is to determine the local direction distribution $\hat{\mathbf{n}}(\mathbf{r})$ that minimizes the total free energy F . This can be found through the Euler–Lagrange equation. If we want to minimize the following integral by varying the form of a function $y(x)$,

$$I = \int_a^b G(y, y', x) dx, \quad (4.8)$$

where y' is the first full derivative of y with respect to x , then $y(x)$ must satisfy the Euler–Lagrange equation,

$$0 = \frac{\partial G}{\partial y} - \frac{d}{dx} \frac{\partial G}{\partial y'}. \quad (4.9)$$

Even with this method, it can become prohibitively difficult to minimize F analytically, depending on the configuration. It is very useful to make what is known as the one-constant approximation, wherein $K_1 = K_2 = K_3 = K$, which greatly simplifies Eq. (4.6) to:

$$\mathcal{F} = \frac{K}{2} \left\{ [\nabla \cdot \hat{\mathbf{n}}(\mathbf{r})]^2 + [\nabla \times \hat{\mathbf{n}}(\mathbf{r})]^2 - \frac{\mathbf{D} \cdot \mathbf{E}}{K} - \frac{\mathbf{B} \cdot \mathbf{H}}{K} \right\}. \quad (4.10)$$

The qualitative behaviour of the solution is still preserved.

4.1.2 Fréedericksz transition

First experimentally observed and studied by Fréedericksz and Repiewa in 1927 [62], this transition describes the threshold for when the bulk liquid crystals held in a cell

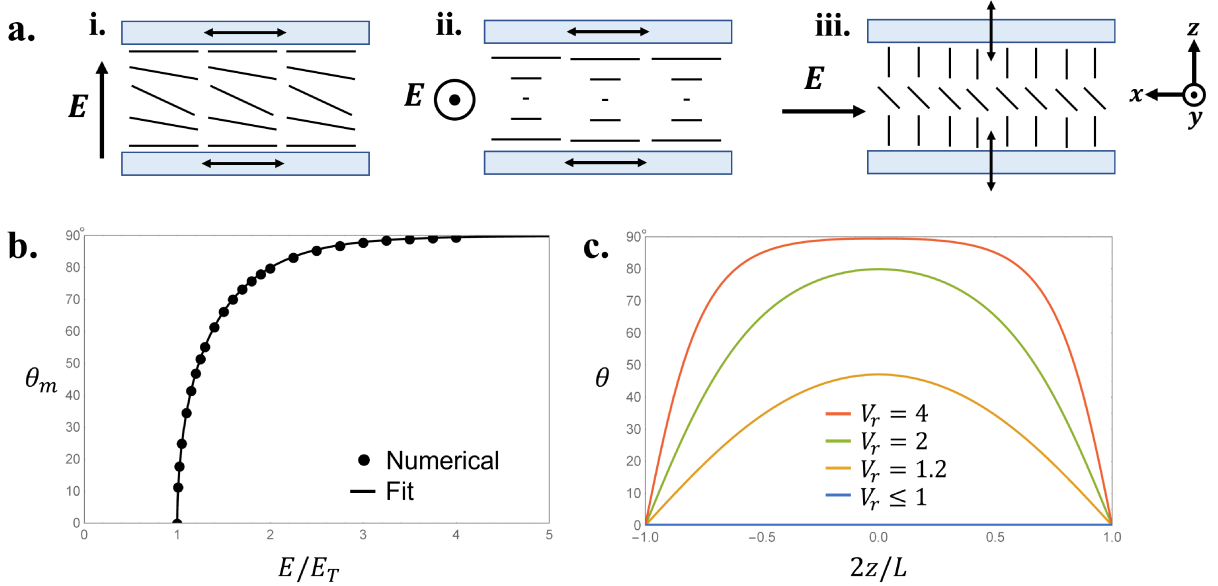


Figure 4.1: **Fréedericksz transition.** a. Sample patterning and field configurations for electric-field-induced i. splay ii. twist, and iii. bend Fréedericksz transitions. b. Plot of the maximum tilt angle $\theta_m(E/E_T)$ as a function of field strength. c. Tilt distributions $\theta(z)$ for reduced voltage $V_r \leq 1$, $V_r = 1.2, 2, 4$.

abruptly begin to align themselves to an increasing strength of applied field (electric or magnetic), perpendicular to the director. Figure 4.1a gives various configurations where the Fréedericksz transition will occur. In the literature, it is customary to first analyze the case of an applied magnetic field, noting that the electric field case is identical except for a conversion constant. I will present the electric field case here as it is more pertinent.

For the case of symmetry liquid-crystal cells, i.e., where the front and back plates have the same uniform easy axis, the liquid crystal will splay in the direction of the applied field (Fig. 4.1a-i), with a general director distribution of,

$$\begin{aligned} n_x &= \cos \theta(z), \\ n_y &= 0, \\ n_z &= \sin \theta(z), \end{aligned} \tag{4.11}$$

For simplicity, we will use the one-constant approximation, but this will give an analytical solution that qualitatively describes the behaviour of the director tilting. Therefore, the non-zero components of \mathcal{F}_D are $[\nabla \cdot \mathbf{n}(\mathbf{r})]^2 = \cos^2 \theta(z)[d\theta(z)/dz]^2$ and $[\nabla \times \mathbf{n}(\mathbf{r})]^2 =$

$\sin^2 \theta(z)[d\theta(z)/dz]^2$. For an applied electric field of $\mathbf{E} = E\hat{\mathbf{z}}$, the free-energy contribution is,

$$\mathcal{F}_E = -\mathbf{D} \cdot \mathbf{E}/2 = -\epsilon_0 E^2(\epsilon_{\perp} + \Delta\epsilon \sin^2 \theta(z))/2 = -(\epsilon_0 \Delta\epsilon E^2/2) \sin^2 \theta(z). \quad (4.12)$$

Note that the first term can be neglected as it is a constant and thus spatially independent. Our total free-energy per unit area A becomes,

$$\frac{F}{A} = \frac{K}{2} \int_0^L dz \left\{ \left(\frac{d\theta(z)}{dz} \right)^2 - \frac{\epsilon_0 \Delta\epsilon E^2}{K} \sin^2 \theta(z) \right\}. \quad (4.13)$$

This gives the following Euler–Lagrange equation to solve,

$$0 = \xi_E^2 \frac{d^2\theta}{dz^2} + \sin \theta \cos \theta, \quad (4.14)$$

where the characteristic electric length ξ_E is defined as,

$$\xi_E = \frac{1}{E} \sqrt{\frac{K}{\epsilon_0 \Delta\epsilon}}. \quad (4.15)$$

The math can be worked out [57] to give the solution for the tilt distribution $\theta(z)$,

$$\frac{\pi}{2} \frac{E}{E_T} \left(1 + \frac{2z}{d} \right) \sin \theta_m = \int_0^{\theta(z)} \frac{d\theta'}{\sqrt{1 - (\sin \theta' / \sin \theta_m)^2}}. \quad (4.16)$$

Here, $E_T = E\xi_E\pi/d = \frac{\pi}{d} \sqrt{\frac{K}{\epsilon_0 \Delta\epsilon}}$ is the threshold field strength of the Fréedericksz transition. This, of course, can be turned into a threshold voltage, which is independent of the thickness d of the cell, $V_T = \pi \sqrt{\frac{K}{\epsilon_0 \Delta\epsilon}}$. The remaining variable, θ_m , defines the maximum tilt angle for a given field strength, located precisely in the middle of the cell. If $E \leq E_T$, then $\theta_m = 0^\circ$, as the field is not strong enough to re-orient the liquid crystals. However, the maximum achievable tilt is $\theta_m = 90^\circ$ when the liquid crystals fully align in the direction of the field. Qualitatively, the functional form of $\theta_m(E)$ is akin to $\arctan\left(\sqrt{E/E_T - 1}\right)$. Figure 4.1b plots the numerically calculated θ_m for a range of field strengths; this was fit using the ansatz,

$$\theta_m(E) = \arctan \left[\left(c_1 \left(\frac{E}{E_T} \right) + c_2 \left(\frac{E}{E_T} \right)^2 + c_3 \left(\frac{E}{E_T} \right)^3 + c_4 \left(\frac{E}{E_T} \right)^4 \right) \sqrt{\left(\frac{E}{E_T} - 1 \right)} \right] \quad (4.17)$$

with $c_1 = 2.34455$, $c_2 = -0.385935$, $c_3 = -0.253328$, and $c_4 = 0.281609$ giving a coefficient of determination of $R^2 = 0.999994$. With this, the tilt distribution $\theta(z)$ can be computed for different field strengths; Fig. 4.1c demonstrates the behaviour tilt distribution for different applied voltages $V/V_T = V_r$.

A conventional assumption for calculations involving liquid-crystal devices is that the tilt angle changes with the applied field but is constant throughout the cell. This would result in a total phase retardation of $\Gamma_T = (2\pi\Delta nd/\lambda) \cos^2 \theta_c$. As this uniform tilt angle $\theta_c \in [0, \pi/2]$ steadily increases to align with the applied field, the total birefringence monotonically decreases from $(2\pi\Delta nd/\lambda)$ to zero. Of course, we now know that the tilt distribution does not stay uniform as the applied field strength increases, and Eq. (2.8) must be used.

For completeness, without approximation, the total free energy that should be minimized according to Eq. (4.6) with the director distribution of Eq. (4.11) is,

$$F = \frac{1}{2} \int_0^L \left\{ (K_1 \cos^2 \theta(z) + K_3 \sin^2 \theta(z)) \left(\frac{d\theta(z)}{dz} \right)^2 - \mathbf{D} \cdot \mathbf{E} \right\} dz \quad (4.18)$$

While this should be solved numerically [63], the tilt distributions follow the qualitative behaviour found in the one-constant approximation. More importantly, the threshold voltage is $V_T = \pi \sqrt{\frac{K_1}{\epsilon_0 \Delta \epsilon}}$, which only depends on the splay coefficient.

4.2 Twisted nematic cell

4.2.1 Field-free case

In Sec. 3.1, we assumed that the twist distribution of twisted nematic liquid-crystal cell was linear with propagation. We can now concretely show that it is indeed linear. Let's begin with the twisted configuration of Fig. 3.1a, assuming strong anchoring; we wish to determine if the twist distribution within the bulk is uniform or non-uniform. The form of the local directors are,

$$\begin{aligned} n_x &= \cos \phi(z), \\ n_y &= \sin \phi(z), \\ n_z &= 0, \end{aligned} \quad (4.19)$$

with the boundary conditions $\phi(0) = 0$ and $\phi(L) = \alpha$. Clearly, $\nabla \cdot \hat{\mathbf{n}}(\mathbf{r}) = 0$, and $\nabla \times \hat{\mathbf{n}}(\mathbf{r}) = \frac{d\phi(z)}{dz}(-\cos\phi(z)\hat{\mathbf{x}} + \sin\phi(z)\hat{\mathbf{y}})$. Inserting this into Eq. (4.10), with $\mathbf{E} = \mathbf{H} = 0$, we get from Eq. 4.7,

$$F = \frac{K}{2} \int d^3r [\nabla \times \hat{\mathbf{n}}(\mathbf{r})]^2 = \frac{K}{2} A \int_0^L dz \left[\frac{d\phi(z)}{dz} \right]^2, \quad (4.20)$$

where A is the area of the glass plates. Letting $y = \phi(z)$, $y' = d\phi(z)/dz$, then $G = (y')^2$, the Euler–Lagrange equation (Eq. 4.9) gives upon integration with appropriate boundary conditions that $\phi(z) = \alpha z/L$, which is precisely the linear form assumed before. Note, for $\alpha = \pi/2$, $\frac{d\phi(z)}{dz}$ could be either positive or negative as a 90° twist could be either left- or right-handed.

4.2.2 Field-induced effects

Here is where things get complicated. As we’ve discussed with the Fréedericksz transition, when a field is applied—electric or magnetic—the directors of the liquid crystals tilt towards the application direction, pinned at the boundaries by the walls of the cell. The overall effect of this is modifying the total phase retardation that light propagating through the cell experiences. A naïve assumption for the twisted case—much like for symmetric PBOEs—would be that again only the phase retardation Γ changes by applying a voltage across the cell and Eq. (3.5) is still applicable. Unfortunately, this is not the case, as the twist distribution is no longer linear. Indeed, it depends on the tilt distribution in a very non-trivial manner. I will set the problem up following [58].

Let the local director distribution be now very general,

$$\begin{aligned} n_x &= \cos\phi(z)\cos\theta(z), \\ n_y &= \sin\phi(z)\cos\theta(z), \\ n_z &= \sin\theta(z), \end{aligned} \quad (4.21)$$

The total free energy to minimize is now,

$$\begin{aligned} F = \frac{1}{2} \int_0^L \left\{ (K_1 \cos^2\theta + K_3 \sin^2\theta) \left(\frac{d\theta}{dz} \right)^2 + (K_2 \cos^2\theta + K_3 \sin^2\theta) \cos^2\theta \left(\frac{d\phi}{dz} \right)^2 \right\} dz \\ - \frac{1}{2} \int_0^L \mathbf{D} \cdot \mathbf{E} dz \end{aligned} \quad (4.22)$$

The dependence on z has been dropped without loss of generality. Recall that $\mathbf{E} = E\hat{\mathbf{z}}$; additionally, $\nabla \times \mathbf{E} = 0$ and $\nabla \cdot \mathbf{D} = 0$ as there are no space-charges. Since the symmetry of our problem requires that there is only z -dependence in all quantities, $\nabla \cdot \mathbf{D}$ implies that $\mathbf{D} = D_z \hat{\mathbf{z}}$. As a result, the second integral in Eq. (4.22) evaluates simply to $ELD_z/2 = VD_z/2$, where V is the voltage applied. We know from Eq. (4.4) that $D_z = \epsilon_0 E_z (\epsilon_\perp \sin^2 \theta + \epsilon_\parallel \cos^2 \theta)$, so we need to massage it a bit to be a constant,

$$V = \int_0^L E_z dz = \frac{D_z}{\epsilon_0} \int_0^L (\epsilon_\perp \sin^2 \theta + \epsilon_\parallel \cos^2 \theta)^{-1} dz. \quad (4.23)$$

This gives D_z as a functional of $\theta(z)$,

$$D_z = \epsilon_0 V \left/ \int_0^L (\epsilon_\perp \sin^2 \theta + \epsilon_\parallel \cos^2 \theta)^{-1} dz \right. \quad (4.24)$$

To simplify going forward, define new constants $\kappa = (K_3 - K_1)/K_1$, $\gamma = (\epsilon_\parallel - \epsilon_\perp)/\epsilon_\perp$, and $\tau = (K_3 - K_2)/K_2$. Then we get the Euler-Lagrange equations from Eq. 4.22 for two canonical variables ϕ , θ , respectively,

$$\frac{d}{dz} \left\{ \frac{d\phi}{dz} (1 + \tau \sin^2 \theta) \cos^2 \theta \right\} = 0, \quad (4.25)$$

$$\begin{aligned} \frac{d}{dz} \left\{ \frac{d\theta}{dz} (1 + \tau \sin^2 \theta) \right\} &= \kappa \sin \theta \cos \theta \left(\frac{d\theta}{dz} \right)^2 + \\ &+ \frac{1 + \kappa}{1 + \tau} \left(\frac{d\phi}{dz} \right)^2 \left\{ \tau \sin \theta \cos^2 \theta - (1 + \tau \sin^2 \theta) \sin \theta \cos \theta \right\} - \\ &- \frac{D_z^2}{K_1 \epsilon_0 \epsilon_\perp / \gamma} \frac{\sin \theta \cos \theta}{(1 + \gamma \sin^2 \theta)^2}. \end{aligned} \quad (4.26)$$

The details for manipulating the above two equations further can be found in [58]. We end up with a series of equations for minimizing the free energy and determining the twist and tilt distributions that we seek. The twist distribution $\phi(z)$ is given by,

$$\phi(z) = \beta \int_0^{\theta(z)} \frac{\sqrt{1 + \kappa \sin^2 \theta}}{g(\theta) \cos^2 \theta (1 + \tau \sin^2 \theta)} d\theta. \quad (4.27)$$

Note, that β is an unknown constant of integration that should be determined from boundary conditions. The tilt distribution $\theta(z)$ is determined implicitly through,

$$\frac{z}{L} = \frac{1}{2} \int_0^{\theta(z)} \frac{\sqrt{1 + \kappa \sin^2 \theta}}{g(\theta)} d\theta \left/ \int_0^{\theta_m} \frac{\sqrt{1 + \kappa \sin^2 \theta}}{g(\theta)} d\theta \right. \quad (4.28)$$

As we saw in Sec. 4.1.2, the maximum tilt angle θ_m occurs in the middle of the cell at $L/2$ and is itself a function of applied field. This $g(\theta)$ function depends on β and θ_m , with the ugly form,

$$g(\theta) = \left\{ \frac{\sin^2 \theta_m - \sin^2 \theta}{(1 + \gamma \sin^2 \theta)(1 + \gamma \sin^2 \theta_m)} + \beta^2 \frac{1 + \kappa}{1 + \tau} \left(\frac{1}{(1 + \tau \sin^2 \theta_m) \cos^2 \theta_m} - \frac{1}{(1 + \tau \sin^2 \theta) \cos^2 \theta} \right) \right\}^{1/2}. \quad (4.29)$$

To even begin thinking about solving $g(\theta)$, we require θ_m and β for a given applied voltage V and maximum twist ϕ_m . The maximum tilt angle is found through,

$$\frac{V}{V_{T0}} = \frac{2}{\pi} \int_0^{\theta_m} \frac{\sqrt{1 + \kappa \sin^2 \theta}}{(1 + \gamma \sin^2 \theta)g(\theta)} d\theta, \quad (4.30)$$

where $V_{T0} = \pi \sqrt{\frac{K_1}{\epsilon_0 \Delta \epsilon}}$ is the threshold voltage for $\phi(z) = 0$, the zero-twist configuration. And from Eq. (4.27), we have,

$$\phi(L/2) = \frac{\phi_m}{2} = \beta \int_0^{\theta_m} \frac{\sqrt{1 + \kappa \sin^2 \theta}}{g(\theta) \cos^2 \theta (1 + \tau \sin^2 \theta)} d\theta. \quad (4.31)$$

This is a coupled set of integrals and should be solved simultaneously. The numerical integration of this equation system is not trivial due to the strongly singular behaviour of the integrand functions. A better way to solve Eqs. (4.30)–(4.31) is to do it iteratively by first setting $\beta = 0$ in Eq. (4.30), giving a first estimate for $\theta_{m0} = \theta_m(\beta = 0)$. This can then be used to determine $\beta_0 = \beta(\theta_{m0})$ and so on, until the desired convergence is achieved. We've opted for a numerical minimization approach based on evolutionary methods, specifically a genetic algorithm, described in Sec. 4.3.

One useful set of analytical results from [58] is the threshold voltage V_T for a given total twist angle ϕ_m ,

$$V_T(\phi_m) = V_{T0} \left[1 + \left(\frac{\phi_m}{\pi} \right)^2 \left(\frac{K_3}{K_1} - 2 \frac{K_2}{K_1} \right) \right]^{1/2}, \quad (4.32)$$

and the value of the integration constant at the threshold voltage β_T for a given ϕ_m ,

$$\beta_T(\phi_m) = \left[\left(\frac{\pi}{\phi_m} \right)^2 + \frac{K_3}{K_1} - 2 \frac{K_2}{K_1} \right]^{-1/2}. \quad (4.33)$$

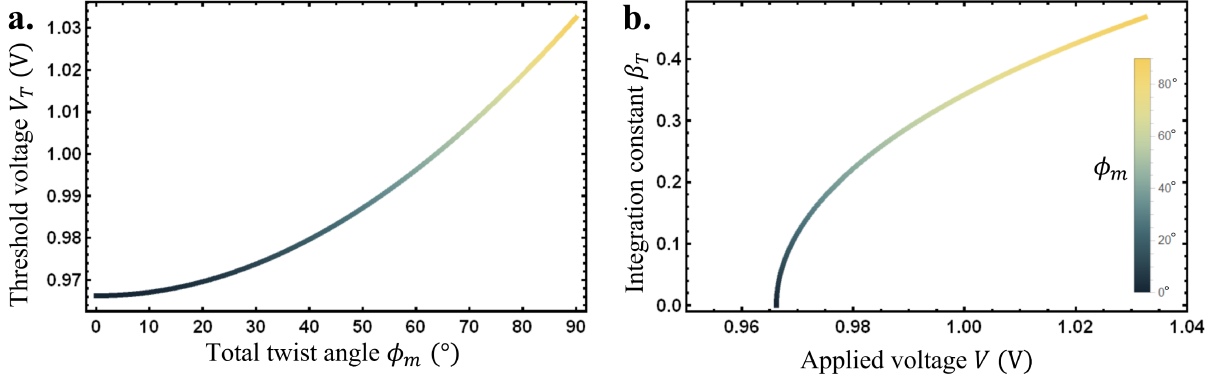


Figure 4.2: **Threshold field conditions for 6CHBT.** As a function of the total twist angle ϕ_m , a. the threshold voltage V_T , and b. the integration constant at threshold β_T .

Figure 4.2 plots these two quantities as a function of the total twist angle for 6CHBT liquid crystals. The usefulness of V_T and β_T is that they represent limiting behaviours and values when $V \rightarrow V_T$ which our numerical minimization approach must be able to reproduce. In particular, we should see that our tilt distributions $\theta(z) \rightarrow 0$ for a given ϕ_m at its corresponding V_T .

4.3 Numerical approach

4.3.1 Genetic algorithm

Inspired by Darwin’s evolutionary theory, the basic idea is to start from a population of completely random guesses and let the workflow of the genetic algorithm (GA) select the individuals that are closer to the actual solution of the original problem [64]. The workflow is based on the application of an iterative scheme composed of three sequential operators: *selection*, *crossover*, and *mutation*. The joint usage of these operators allows the algorithm to evolve a population of candidate solutions to a given problem toward near-optimal solutions, making these algorithms particularly well-suited to efficiently solve hard problems [65, 66]. Each candidate solution is referred to as an *individual* or *chromosome*. Starting from an initial set of possible solutions, a selection operator aims at choosing the ‘best’ solutions in the population, forming in this way the so-called *mating pool*. The individuals in the mating pool are used to create new possible solutions, forming the *offspring* by means of crossover and mutation operators, which respectively emulate the

recombination and the mutation of individuals in a natural environment. In the end, the offspring replace the initial population of the algorithm and a new iteration, denoted as a *generation*, can start. The algorithm ends when a certain termination criterion is reached [67].

To approximately solve Eqs. (4.30)–(4.31), we implement two genetic algorithms which evolve real-valued individuals θ_{mi} and β_i . As prescribed by the iterative method mentioned above, the first algorithm is first run to determine θ_{m0} , corresponding to the initial guess for $\beta = 0$. The second algorithm is then first run to determine β_0 assuming $\theta_m = \theta_{m0}$, and so on. Each individual is a candidate to provide an optimal approximation to the actual solutions θ_m and β . By means of operators mimicking the natural selection mechanism, the GA selects for reproduction those individuals which better minimize the following cost functions,

$$\mathcal{L}_{\theta_m} = \left| \frac{V}{V_0} - \frac{2}{\pi} \int_0^{\theta_m} \frac{\sqrt{1 + \kappa \sin^2 \theta}}{(1 + \gamma \sin^2 \theta)g(\theta)} d\theta \right|^2, \quad (4.34)$$

$$\mathcal{L}_{\beta} = \left| \phi_m - 2\beta \int_0^{\theta_m} \frac{\sqrt{1 + \kappa \sin^2 \theta}}{g(\theta) \cos^2 \theta (1 + \tau \sin^2 \theta)} d\theta \right|^2, \quad (4.35)$$

within the current generation to solve Eq. (4.30) and Eq. (4.31), respectively. The numerical integrations required for these cost functions are successfully performed using the IMT-rule—named after Iri, Moriguti, and Takasawa who first proposed the method in 1969 [68]—to handle singularities in finite integration regions [69].

The detailed sequence of operators used in our algorithm will now be described. First, the well-known *tournament selection* mechanism [70] is used as a selection operator. This consists of repeating the following steps N times, where N is the population size:

1. Randomly select a subset of k individuals.
2. Choose the fittest individual among them to be inserted in the mating pool.

For our purposes, the ‘fittest’ are those individuals for which the cost function is minimum. The *blend crossover* [71] is used to mate individuals in the mating pool. This means that when two individuals θ_A and θ_B reproduce, two newborn individuals θ_1 and θ_2 originate as random numbers belonging to the interval $[\theta_A - c_i(\theta_B - \theta_A), \theta_B + c_i(\theta_B - \theta_A)]$, where c_i tunes the crossover with $i = \{1, 2\}$, and we assume $\theta_B \geq \theta_A$. A similar reproduction occurs for two individuals β_A and β_B . To explore a wider region of the parameter landscape,

genetic mutations are included in our workflow in the form of Gaussian noise with mean μ and standard deviation σ which potentially affects single individuals [72]. Our GAs also include an *elitism* mechanism: the best individual from the old population is carried over to the next one, replacing the worst individual of the offspring. This mechanism pushes the algorithms to a faster convergence toward the best solutions. To preserve the physical validity of the final prediction for the maximum tilt angle θ_m , a modulo- $\pi/2$ is performed after each operation on a θ -individual. The maximum number of generations N_{gen} is used as the termination criterion.

Algorithm 4.1 presents the pseudo-code of the implemented GA. The parameters that determine the evolutionary sequence are termed *hyper-parameters*, the optimal choice of which will give a fast and adequate convergence. With the GA hyper-parameters reported in Table 4.2, the desired convergence for θ_m and β is achieved within ~ 10 iterations. Adequate convergence is chosen to be when the cost functions are minimized with differences less than 10^{-15} .

Algorithm 4.1 Pseudo-code of the implemented genetic algorithm

Input: size of the population pop_size , tournament size k , crossover probability p_c , c for blend crossover, mutation probability p_m , μ and σ for Gaussian mutation, termination criterion t

Output: the best solution $best$

```

gen ← 0
pop ← generateRandomPopulation(pop_size)
checkPhysicalConstraints(pop)
evaluateFitness(pop)
best ← getBestIndividual(pop)
while gen < t do
  offspring ← executeTournament(pop, k)
  checkPhysicalConstraints(offspring)
  executeGaussianMutation(offspring, p_m, μ, σ)
  evaluateFitness(offspring)
  pop ← offspring
  pop ← elitism(pop, best)
  best ← getBestIndividual(pop)
  gen ← gen + 1
end while
return best

```

Once the best estimates for θ_m and β have been determined. The same evolutionary

Table 4.2: Genetic algorithm hyper-parameters.

Size	Selection parameters	Crossover parameters	Mutation parameters
$N = 40$	$k = 3$	$p_c = 0.9$	$p_m = 0.1$
$N_{gen} = 20$		$c_1 = c_2 = 0.5$	$\mu = 0, \sigma = 0.2$

strategy is devised for retrieving the modulations of the twist $\phi(z)$ and tilt $\theta(z)$ distributions. By symmetry, we know that the distributions in the second half of the cell will be directly related to those in the first half; therefore, we need only compute the distributions from $0 < z < L/2$. Half the cell thickness $L/2$ is divided into small intervals—here, 50 intervals was used—and the GA is executed within each slice. The set of solutions $\{\theta(0), \theta(z_1), \theta(z_2), \dots, \theta(L/2)\}$ of Eq. (4.28) is first determined by minimizing the following cost function within each interval,

$$\mathcal{L}_\theta = \left| \frac{z}{L} \int_0^{\theta_m} \frac{\sqrt{1 + \kappa \sin^2 \theta}}{g(\theta)} d\theta - \frac{1}{2} \int_0^{\theta(z)} \frac{\sqrt{1 + \kappa \sin^2 \theta}}{g(\theta)} d\theta \right|^2. \quad (4.36)$$

At each propagation distance z_i , the corresponding solution $\theta(z_i)$ is then used to determine $\phi(z_i)$ via a subsequent algorithm by minimizing the cost function,

$$\mathcal{L}_\phi = \left| \phi(z) - \beta \int_0^{\theta(z)} \frac{\sqrt{1 + \kappa \sin^2 \theta}}{g(\theta) \cos^2 \theta (1 + \tau \sin^2 \theta)} dz \right|^2. \quad (4.37)$$

In both cases, a modulo- $\pi/2$ is performed after each operation carried out on an individual. Since the tilt and twist distributions are not expected to feature singular behaviours, the solution found at a given position z_i should not be too different from the solution associated with z_{i-1} and z_{i+1} . Therefore, the initial population of the GA performed at each position other than $z = 0$ —which is known from boundary conditions—can be initialized using the solution found at the previous position, perturbed with a uniform noise Δ . Here, we chose Δ between 0.05 and 0.1, depending on whether we were close to V_T or not. This allows us to initialize the current GA very close to the actual solution. Accordingly, few generations are needed to obtain an adequate convergence, greatly reducing the computation time. These genetic algorithms were performed using Mathematica 10.1 on a laptop with an Intel® Core™ i7-8565U CPU @ 1.80 GHz, 1992 MHz, 4 cores, and 8 logical processors. The total calculation run time for a given set of initial conditions was about 15–20 minutes.

4.3.2 Jones matrix method

With the numerical tilt and twist distributions in hand, we now seek the total Jones matrix of the corresponding LC cell to explore its effect on polarized light. As we saw in Sec. 3.1 for the field-free case, the total matrix was derived by multiplying N thin, gradually rotated waveplates of phase retardation Γ/N , with the analytic solution in the limit of $N \rightarrow \infty$,

$$\begin{aligned} \mathbf{T}_{\phi_f}(\phi_m, \Gamma) &= \mathbf{R}(-\phi_b) \begin{bmatrix} \cos X - \frac{i\Gamma}{2X} \sin X & \frac{\phi_m}{X} \sin X \\ -\frac{\phi_m}{X} \sin X & \cos X + \frac{i\Gamma}{2X} \sin X \end{bmatrix} \mathbf{R}(\phi_f) \\ &= \mathbf{R}(-\phi_b) \mathbf{M}_0(\phi_m, \Gamma) \mathbf{R}(\phi_f), \end{aligned} \quad (4.38)$$

where $X = \sqrt{\phi_m^2 + (\Gamma/2)^2}$. For the field-induced case, we do not have the luxury of an analytical solution, so we must make do with an approximation to the total Jones matrix. Here, we will instead multiply together N twisted cells of thickness $d = L/N$ using the form Eq. (4.38) with appropriate local twist and phase retardation calculated from $\phi(z)$ and $\theta(z)$,

$$\mathbf{J}_{\phi_f}(\phi_m, V) = \prod_{j=0}^N \mathbf{T}_{\phi(z_j)} \left(\phi(z_{j+1}) - \phi(z_j), \frac{\pi \Delta n d}{\lambda} (\cos^2 \theta(z_{j+1}) + \cos^2 \theta(z_j)) \right) \quad (4.39)$$

$$= \mathbf{R}(-\phi_b) \left[\prod_{j=0}^N \mathbf{M}_0(\phi'_m(z_j), \Gamma'(z_j)) \right] \mathbf{R}(\phi_f), \quad (4.40)$$

where $z_j = jd$, $\phi'_m(z_j) = \phi(z_{j+1}) - \phi(z_j)$, $\phi_f = \phi(0)$, and $\phi_b = \phi(L)$ are the front and back alignment angles, respectively, and $\phi_m = \phi(L) - \phi(0)$ is the total twist angle. In order to better estimate the phase retardation of each thin twisted cell, the trapezoidal rule is applied when calculating Eq. (2.8) in favour of left or right Riemann sums. That is, when integrating a function $f(z)$ from $z = a$ to $z = b$, the integral may be approximated by a trapezoid of area $(b-a)(f(b) + f(a))/2$. In this case,

$$\Gamma'(z_{j+1}) = \frac{\pi \Delta n d}{\lambda} [\cos^2 \theta(z_{j+1}) + \cos^2 \theta(z_j)]. \quad (4.41)$$

4.4 Results and discussion

4.4.1 β - θ_m

Let's now take a closer look at the results produced by our GA minimization method. A good place to start is analyzing the behaviour of the integration constant β and maximum

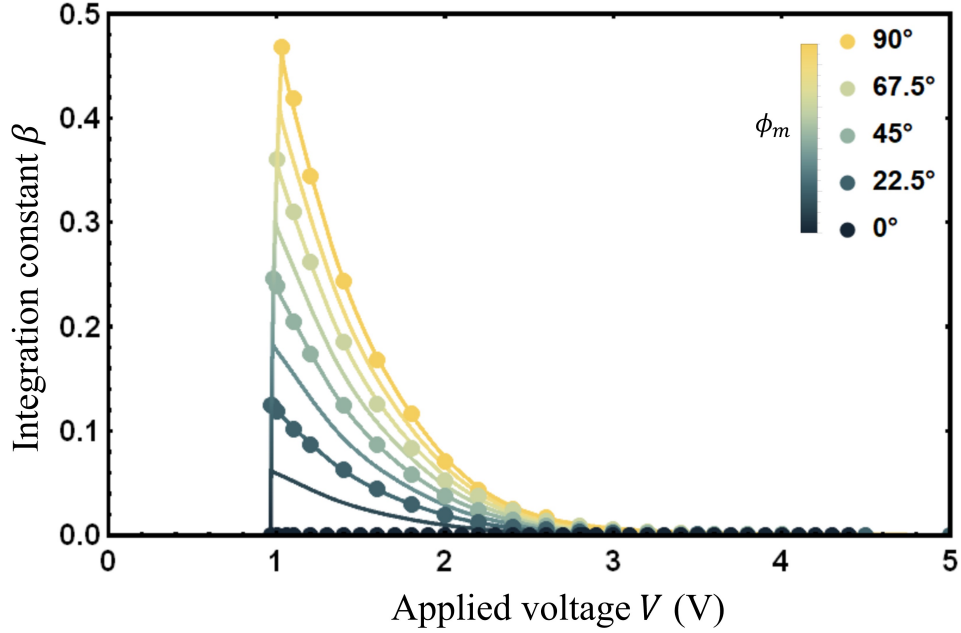


Figure 4.3: **Integration constant** $\beta(\phi_m, V)$. The dots correspond to the numerically calculated values for maximum twist angles $\phi_m = 90^\circ, 67.5^\circ, 45^\circ, 22.5^\circ, 0^\circ$. The vertical gradient line is the analytical $\beta_T(\phi_m)$ values from Eq. 4.33, whereas the cascading solid-coloured lines are the lines of best using Eq. 4.42.

tilt angle θ_m as a function of applied voltage V . These three parameters along with a given maximum twist angle ϕ_m completely determine the twist $\phi(z)$ and tilt $\theta(z)$ distributions. Figure 4.3 and Fig. 4.4 summarize the numerically computed results. The GA was run for maximum twist angles of $\phi_m = 90^\circ, 67.5^\circ, 45^\circ, 22.5^\circ, \text{ and } 0^\circ$ at a range of voltages from 0.96 V to 7 V, with resulting cost function \mathcal{L}_β values of less than 10^{-32} , and \mathcal{L}_{θ_m} between 10^{-17} and 10^{-26} . The behaviours for negative twist angles will be either identical or related, so they are not considered.

For $\beta(\phi_m, V)$, the first measure of whether the GA is working as intended is whether it can match the threshold $\beta_T(\phi_m)$ values according to Eq. 4.33. As can be seen in Fig. 4.3, the GA does indeed replicate the correct $\beta_T(\phi_m)$ at each maximum twist angle's respective threshold voltage. The data points for each ϕ_m follow a smooth decreasing trend, asymptotically approaching zero for large voltages. Since it would take a prohibitive amount of time to compute every possible β , a massive time-saving tool to have would be an analytical formula, or a good approximation of the true values. I thus postulate an ansatz

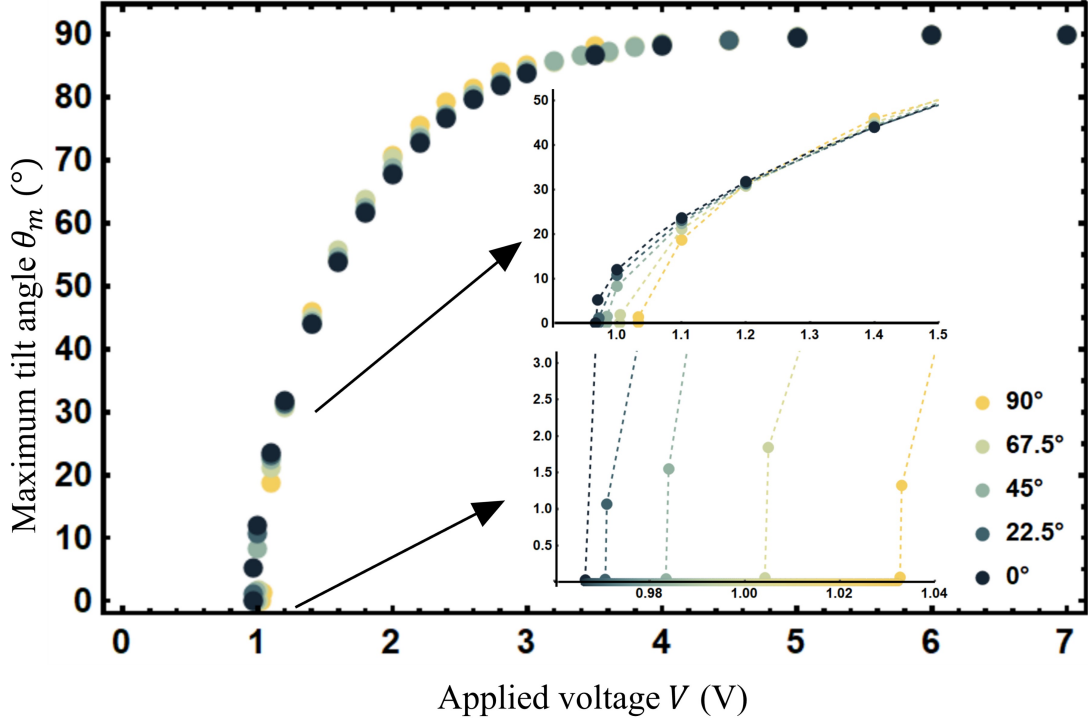


Figure 4.4: **Maximum tilt angle** $\theta_m(\phi_m, V)$. The dots are the numerically calculated values for maximum twist angles $\phi_m = 90^\circ, 67.5^\circ, 45^\circ, 22.5^\circ, 0^\circ$. In the bottom inset, the gradient line is the theoretical $V_T(\phi_m)$ from Eq. 4.32. The dashed lines in both insets merely connect the dots for visual ease.

of,

$$\beta(\phi_m, V) = \beta_T(\phi_m) \left(1 - \frac{2}{\pi}\right) \arctan \left[(c_1 V + c_2 V^2 + c_3 V^3 + c_4 V^4) \sqrt{V - V_T(\phi_m)} \right], \quad (4.42)$$

where c_i are a common set of fitting parameters for all ϕ_m . Equation 4.42 exhibits the expected behaviour: 1. $\beta(\phi_m, V)$ does not exist for $V < V_T(\phi_m)$; 2. when $V = V_T(\phi_m)$, $\beta(\phi_m, V) = \beta_T(\phi_m)$; and 3. $\beta(\phi_m, V) \rightarrow 0$ as $V \rightarrow \infty$. I used the computed data set for $\beta(45^\circ, V)$ to determine the c_i . The fitting parameters obtained are $c_1 = -7.95043$, $c_2 = 16.5784$, $c_3 = -10.5245$, and $c_4 = 2.35869$, giving a coefficient of determination of $R_{45}^2 = 99.99\%$. With these c_i , the coefficients of determination for the other computed data sets are $R_{90}^2 = 99.98\%$, $R_{67.5}^2 = 99.97\%$, $R_{22.5}^2 = 99.98\%$, and $R_0^2 = 100\%$. Indeed, when the other computed data sets are used for fitting, the c_i come out to be almost the

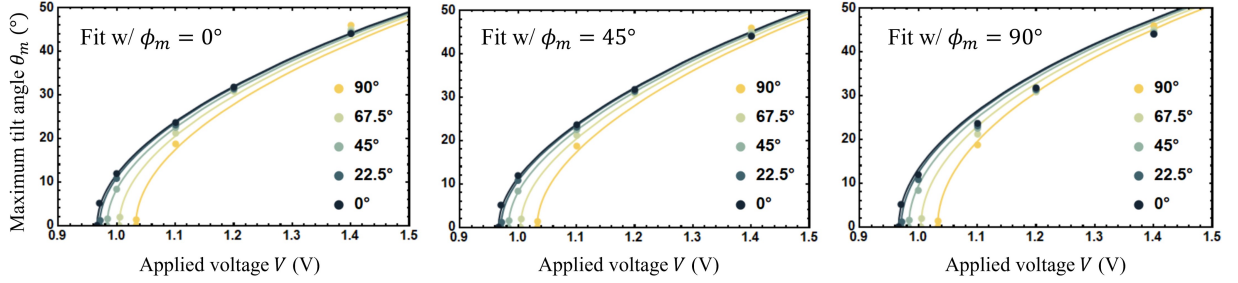


Figure 4.5: **Fits for $\theta_m(\phi_m, V)$.** Using the ansatz in Eq. (4.43), fits are produced using the $\phi_m = 0^\circ, 45^\circ, 90^\circ$ data sets. Each fit is then used to produce the $\theta_m(\phi_m, V)$ curves for other ϕ_m values, as shown in each subplot.

same with equally high R^2 values. Presumably, the fitting polynomial in the argument of $\arctan(\cdot)$ in Eq. 4.42 is actually some function of the elastic coefficients and material parameters, independent of ϕ_m ; however, no such function, let alone this form of ansatz, is mentioned in the literature to my knowledge. Higher-order terms could be included, but four was found to be sufficient.

Next up is the maximum tilt angle $\theta_m(V)$. Much like the non-twisted case in Fig. 4.1b, we have the behaviour that $\theta_m = 0$ when $V < V_T$ for each ϕ_m . The bottom inset of Fig. 4.4 shows that the GA reproduces the threshold voltage values of Eq. (4.32). The top inset is a zoom-in to show what appears to be a common crossing point around 1.2 V with $\theta_m \sim 30.9^\circ$. We can also try to fit these curves with one form, using a similar ansatz to Eq. (4.17),

$$\theta_m(\phi_m, V) = \arctan \left[(b_1 V + b_2 V^2 + b_3 V^3 + b_4 V^4) \sqrt{V - V_T(\phi_m)} \right], \quad (4.43)$$

where b_i are new common fitting parameters. As before, this ansatz obeys the expected behaviours: 1. when $V = V_T(\phi_m)$, $\theta_m = 0$ for each ϕ_m , and 2. as $V \rightarrow \infty$, $\theta_m \rightarrow 90^\circ$. However, when this form is plotted out for the different ϕ_m , it fails to reproduce the crossing point around 1.2 V. We can see this in Fig. 4.5 where different data sets were used for fitting, each with respective R^2 values of 99.99% for the fitted data set. This suggests that there is an extra ϕ_m dependence that Eq. (4.43) does not include. While there is the possibility that the GA is not converging to the necessary values, I do not believe this to be the case given the extremely small cost function values and the smooth behaviours of the computed data sets.

There is a hint about this dependence in the literature. [59] studies the tilt and twist

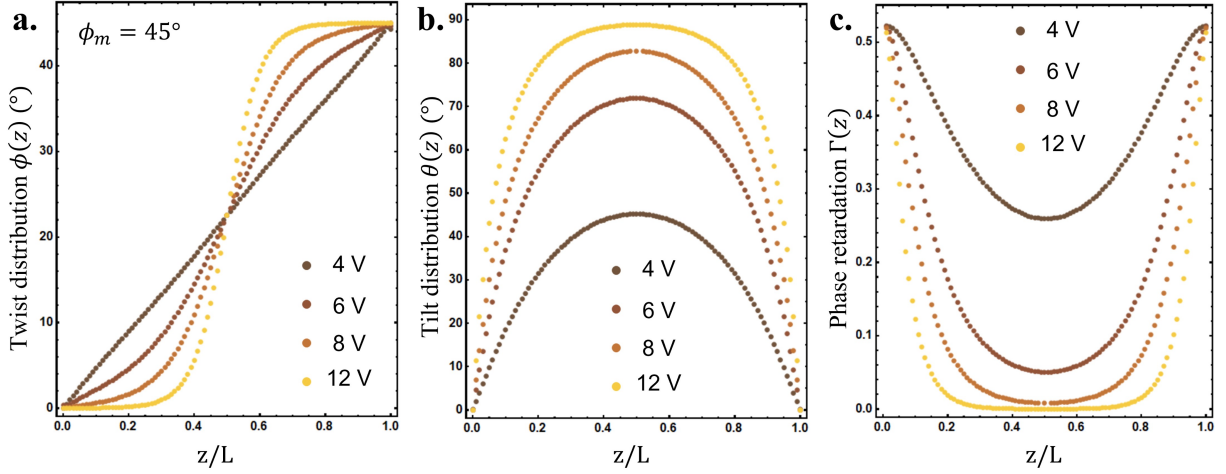


Figure 4.6: **GA results for $\phi_m = 45^\circ$.** a. Twist and b. tilt distributions for $V_{pp} = 4, 6, 8, 12$ V. c. Phase retardation distribution $\Gamma(z)$ computed using $L = 35 \mu\text{m}$.

distributions in the high-voltage limit, and provide an approximation for θ_m when $V \gg V_{T0}$,

$$\tan^2(\theta_m) \approx (1 + \tan^2(\phi_m/2)) \tan^2(\theta_{m0}), \quad (4.44)$$

where θ_{m0} is the maximum tilt angle for the non-twisted case at the same voltage. A ϕ_m dependence for low voltages or voltages near threshold where the critical behaviour happens was not found in the literature. At the time of writing this, it is not obvious what the correct ansatz is, as simply adding this factor or another fitting polynomial does not produce satisfactory fits. If a semi-analytical form can be found that reproduces the GA θ_m data sets, then along with Eq. (4.42) for $\beta(\phi_m, V)$, one would no longer need to run the GA for every desired (ϕ_m, V) , greatly reducing computation time.

4.4.2 Tilt and twist distributions

With numerical values for $\beta(\phi_m, V)$ and $\theta_m(\phi_m, V)$ in hand, we can now use the GA to compute the sought-after tilt and twist distributions. Figure 4.6 displays the results of $\phi_m = 45^\circ$ for different voltages $V_{pp} = 4, 6, 8, 12$ V. A note should be made that the applied voltage V that we have been using corresponds to a DC voltage as it assumes a static externally applied electric field. As briefly mentioned in Sec. 3.4, a sinusoidal, i.e., AC, voltage is generated using the function generator with peak-to-peak voltage V_{pp} . Therefore, V is in fact the root-mean-square voltage with conversion of $V = V_{rms} = V_{pp}/(2\sqrt{2})$.

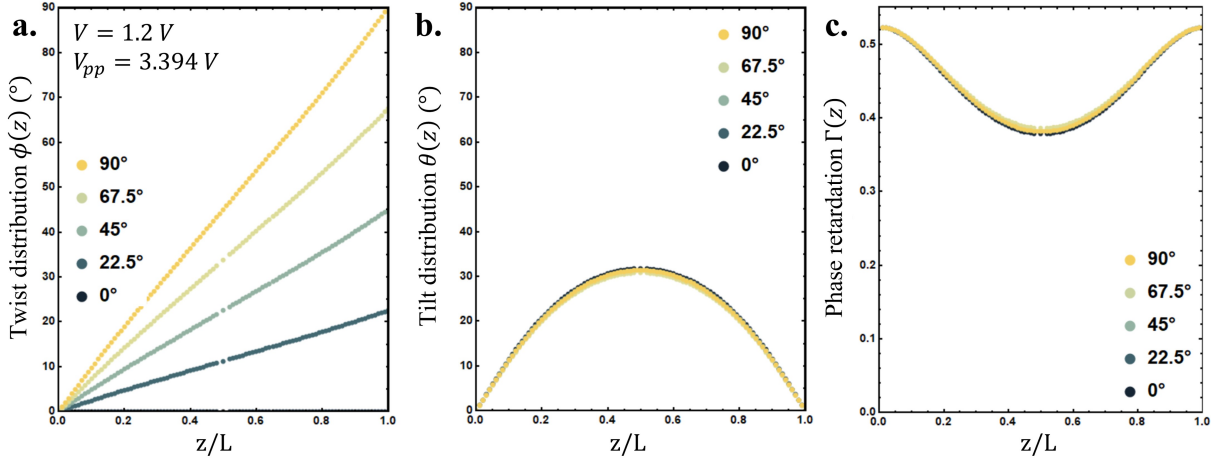


Figure 4.7: **GA results for 1.2 V.** a. Twist, b. tilt, and c. phase retardation distributions for $\phi_m = 0^\circ, 22.5^\circ, 45^\circ, 67.5^\circ, 90^\circ$ with $L = 35 \mu\text{m}$.

We immediately see that the twist distribution is no longer linear as we increase the applied field strength, confirming our suspicions that the Jones matrix of Eq. (3.5) is no longer valid. However, there appears to be a voltage up to which $\phi(z)$ is still linear above the threshold voltage. Here, $V_T(45^\circ) = 0.983188$ V or $V_{pp} = 2.78088$ V. As the field strength increases further, the distributions take on an S-like shape, becoming sharper and more step-like. As for the tilt distributions, we see similar behaviour as with the zero-twist case in Fig. 4.1c. Above the threshold, the maximum tilt angle steadily approaches $\theta_m = 90^\circ$ with increasing voltage. As the field strength increases even further, the distribution flattens out further in the middle. The phase retardation distribution $\Gamma(z)$ is calculated based on $\theta(z)$ using $L = 35 \mu\text{m}$ in Eq. (4.41).

Figure 4.7 and Fig. 4.8 are the GA results of $V = 1.061, 1.2, 2.0,$ and 4.0 V for various maximum twist angles. We see that there is a similar evolution of the twist distributions from linear to S-like, and the tilt distributions plateauing up to $\theta_m = 90^\circ$. Notably at 1.2 V, the tilt distributions in Fig. 4.7b are practically the same, corresponding to the observed crossing point in Fig. 4.4 with $\theta_m \sim 30.9^\circ$. As it so happens, the twist distributions begin to deviate from linear above this point for all ϕ_m . It is unclear as to whether this is a coincidence or the physical significance of this crossing point, let alone the mathematical explanation. Unfortunately, there is no analytical formula for the tilt distribution $\theta(\phi_m, V, z)$. There does exist analytical approximations for the twist distribution $\phi(\phi_m, V, z)$ in the high-voltage limit ($V \gg V_{T0}$) [59]; however, it does not capture the critical behaviours at low voltages such as the transition from linear to non-linear twists.

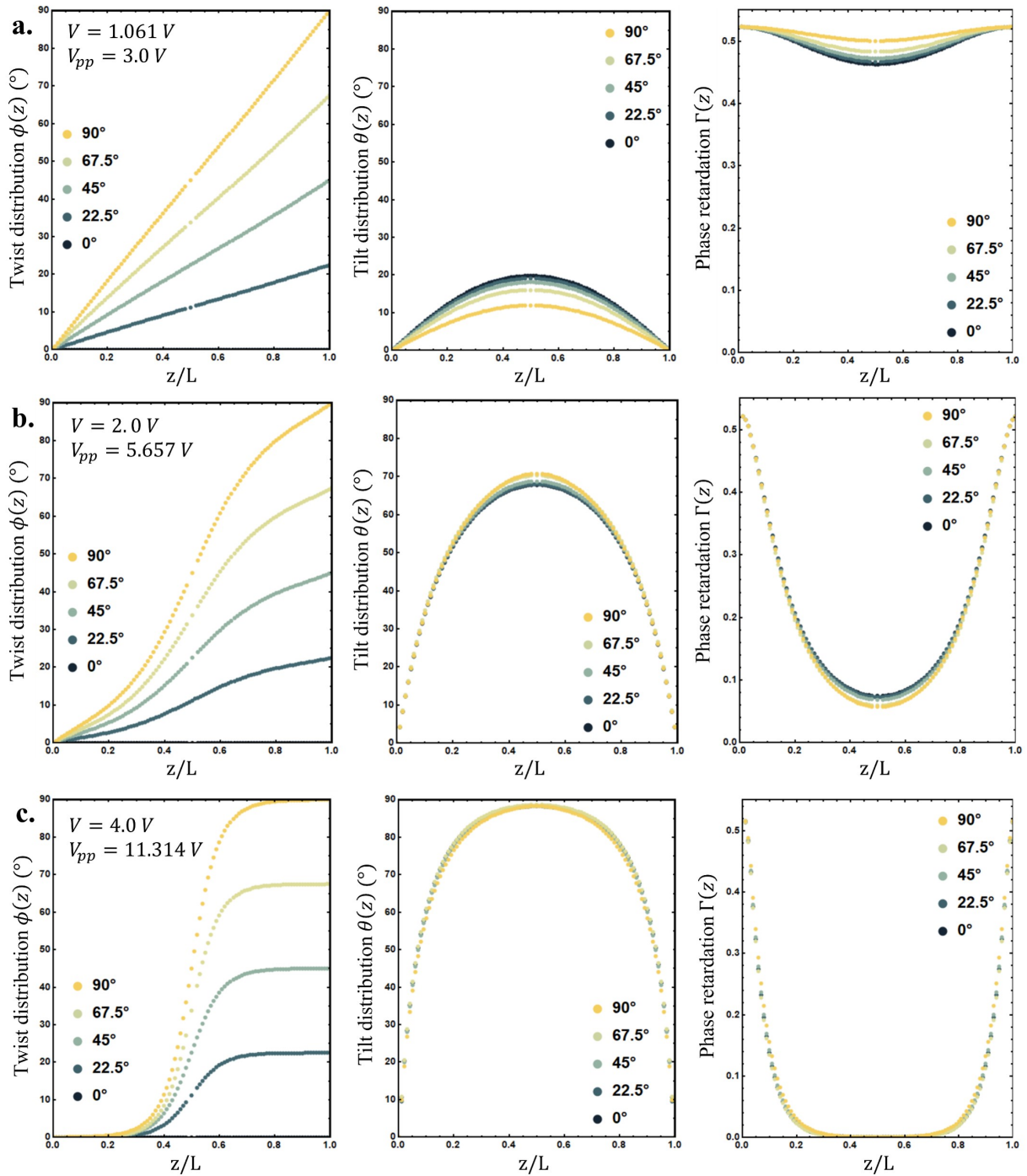


Figure 4.8: GA results for different maximum twist angles. a. $V = 1.061\text{ V}$, b. $V = 2.0\text{ V}$, c. $V = 4.0\text{ V}$.

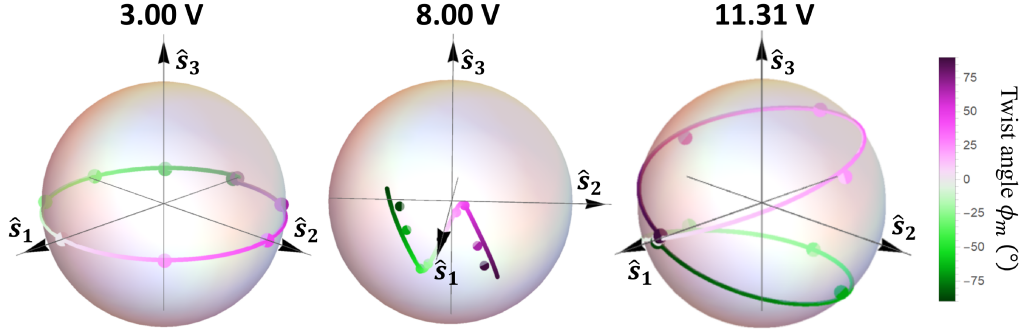


Figure 4.9: Comparison of output states generated via the approximated tilt and twist distributions (colored lines) based on $\phi(45^\circ, V, z)$ and $\theta(45^\circ, V, z)$ versus the numerically calculated distributions for each ϕ_m (colored dots). A horizontally polarized input was used.

4.4.3 Polarization effects

The numerical twist, tilt, and phase retardation distributions can now be converted to a Jones matrix according to Eq. (4.39). To greatly save on computation time, an additional rough approximation is made in that the twist distributions for different ϕ_m are simply scaled versions of each other; for example, $\phi(90^\circ, V, z) = 2 \times \phi(45^\circ, V, z)$. Consequently, the same tilt/phase retardation distributions are assumed the same for all ϕ_m at a given voltage; this is more or less the case for higher voltages, with deviations expected at lower voltages. Figure 4.9 shows that the difference between using the numerically calculated distributions as opposed to the approximate distributions based on $\phi_m = 45^\circ$ is minimal, with average state overlaps of over 99%.

Figure 4.10b. compares the reconstructed experimental Stokes data for DP(0,1/2) and horizontally polarized input light, with the numerically obtained approximation using $\phi(45^\circ, V, z)$ and $\theta(45^\circ, V, z)$. Uncertainties on the experimental points are comparable to those given for the case with no voltage applied, as listed in Appendix A. Qualitatively, we finally have a model that mimics the experimentally observed behaviours, which was not possible by simply assuming a linear twist distribution and varying Γ . We also see that the now non-linear twist distributions account for the novel and peculiar phenomenon of the evolving topological charge seen in Fig. 4.10a: the topological charge changes from $q \sim 1/2$ to $q \sim 1$ to $q \sim 0$ back to $q \sim 1$ as we increase the voltage. We can discuss the behaviour of this a bit more by looking at the Stokes vectors on the PS as a function of maximum twist angle ϕ_m . Around $V_{pp} = 8.00$ V, the polarization distribution is more or less

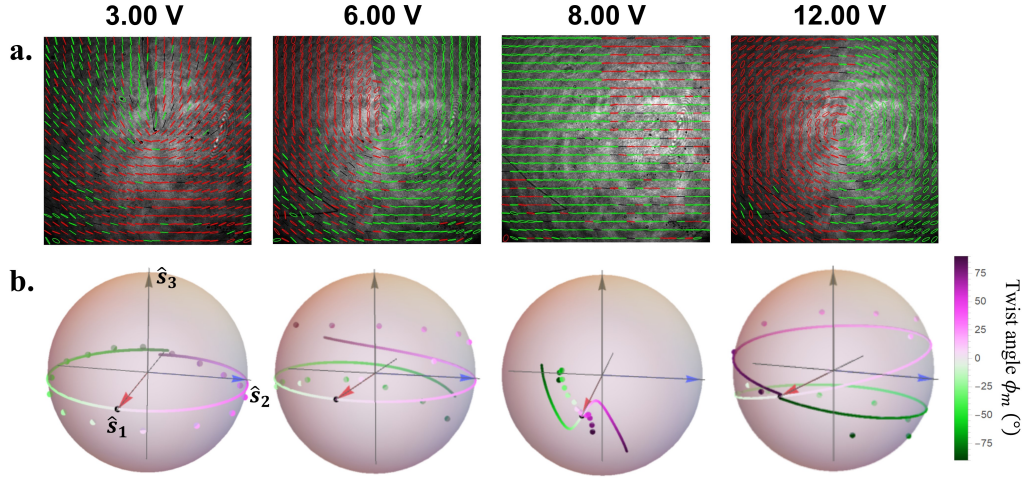


Figure 4.10: **Externally applied voltage on DP(0,1/2)**. a. Reconstructed polarization distributions from a horizontally polarized input for voltages of $V_{pp} = 3.00, 6.00, 8.00,$ and 12.00 V. b. The experimental data (dots) are the output Stokes vectors. Numerical approximations (graduated solid line) were obtained by scaling the twist distribution for $\phi_m = 45^\circ$.

uniform, and the Stokes vectors are clustered around $s_1 = [1, 0, 0]$, i.e., the horizontal input becomes almost a horizontal output for all ϕ_m . This is similar to the detuned setting for q -plates. For $V_{pp} = 3.00$ V, the Stokes vectors wrap around the equator once, which gives rise to a lemon-like polarization distribution, possessing a topological charge of $q \sim 1/2$. Since $V_{pp} = 3.00$ V which is equivalent to $V = 1.061$ V is below the ‘crossing-point’ at $V \sim 1.2$ V, the twist distribution is still linear. Indeed, the plotted Stokes vectors are qualitatively similar to those of DP(0,1/2) for the field-free case in Fig. 3.5b. As the voltage is increased, the Stokes vectors as a function of ϕ_m begin to wrap around the equator more than once. This is the key point that signals the departure from the linear-twist regime as this is not achievable by simply varying Γ in $\mathbf{T}_0(\phi_m, \Gamma)$. When the line wraps around the equator twice, then the topological charge is $q \sim 1$, producing an azimuthal-like polarized distribution, as seen at $V_{pp} = 12.00$ V. While detuning is observed with standard q -plates, this apparent charge-doubling is never observed nor achievable. Further investigations and calculations are required to determine if we do indeed reach true changes in the topological charge. This would open up another avenue to create a multi- q -plate.

Figure 4.11a, b compares the experimental data of DP(1/2,0) and the GA results for voltages of $V_{pp} = 3, 6, 8, 12$ V. We see that there is quite a discrepancy between the

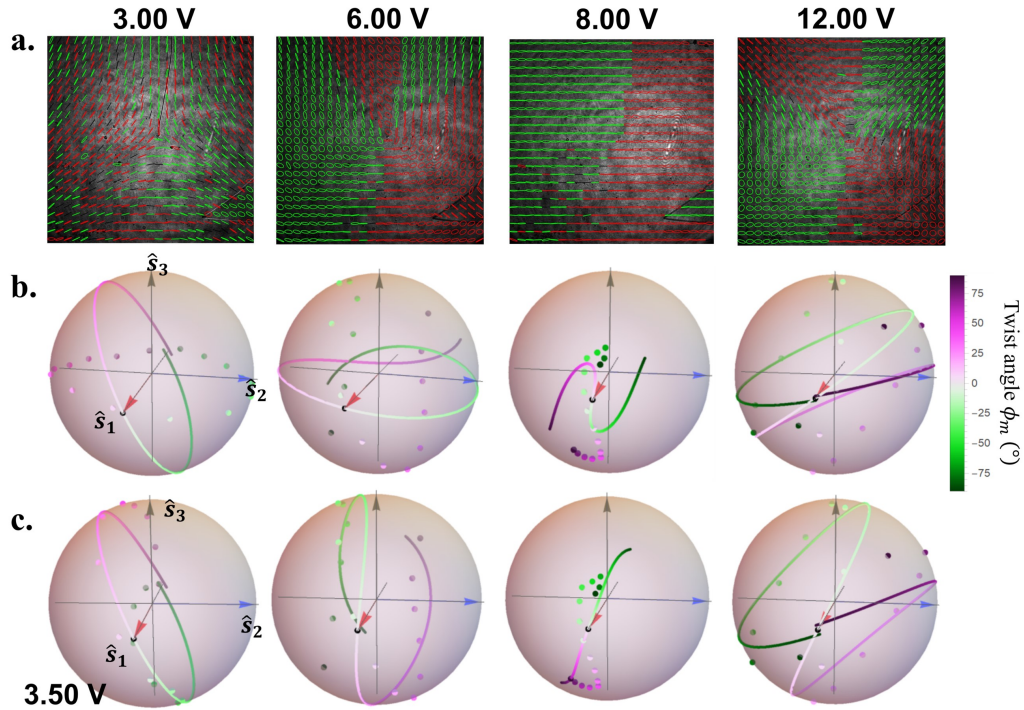


Figure 4.11: **Externally applied voltage on DP(1/2,0)**. a. Reconstructed polarization distributions from a horizontally polarized input for voltages of $V_{pp} = 3, 6, 8,$ and 12 V. b. The experimental data (dots); numerical approximations (gradiated solid line) were obtained by scaling the twist distribution for $\phi_m = 45^\circ$. c. Numerical (experimental) results at $V_{pp} = 3$ V (3.5 V), 5.5 V (6 V), 7.5 V (8 V), and 11.5 V (12 V).

two. However, this seems to be a problem of voltage scaling between what is set on the function generator and what the LC device feels, as we see in Fig. 4.11c where the comparison is with numerical results at about half a volt less, giving qualitatively good fits. This would suggest that the contact points where the electrical wires were soldered came loose between the experimental data collections of DP(0,1/2) and DP(1/2,0), which is not surprising given the delicate nature of the glass-metal bond. For future fabricated samples, the applied voltage should be properly measured across the sample; this would rule out soldering problems when trying to compare to the theory.

Overall, the take-away message from this chapter is that the inclusion of elastic continuum theory can explain the non-trivial behaviour displayed from non-symmetrically patterned LC devices fabricated in Chap. 3, which is reassuring. This was greatly aided

by the use of genetic algorithms to numerically calculate the non-linear tilt and twist distributions. There is certainly still more work to be done in regards to creating a complete semi-analytical solution to decrease computation time; however, the work presented here lays the foundation to properly calculate the field-induced effects on polarized light.

I think it's time for a reprieve from liquid crystals, don't you? Let's take a dip into...

Chapter 5

Underwater Quantum Cryptography

This chapter is based on the following papers:

1. F. Hufnagel, **A. Sit**, F. Grenapin, F. Bouchard, K. Heshami, D. England, Y. Zhang, B. J. Sussman, R. W. Boyd, G. Leuchs, E. Karimi, “Characterization of an underwater channel for quantum communications in the Ottawa River,” *Optics Express* **27**, 26346–26354 (2019).

DOI: <https://doi.org/10.1364/OE.27.026346>

© 2019 Optical Society of America

2. F. Hufnagel, **A. Sit**, F. Bouchard, Y. Zhang, D. England, K. Heshami, B. J. Sussman, E. Karimi, “Investigation of underwater quantum channel in a 30-meter flume tank using structured photons,” *New Journal of Physics* **22**, 093074 (2020).

DOI: <https://dio.org/10.1088/1367-2630/abb688>

© 2020 IOP Publishing

5.1 Quantum key distribution

The goal of secure communication is a tale as old as time. Throughout history, various methods and techniques have been used to protect sensitive information from unauthorized access and interception: from ciphers machines and codebooks to one-time pad and

encryption schemes. Today, more sophisticated algorithms like the Advanced Encryption Standard (AES) [73] and RSA (Rivest-Shamir-Adleman) [74] are widely used, relying on computational complexity for security. With the advent of quantum computing and the potential threat it poses to conventional cryptographic methods, the need for secure communication protocols that are resistant to quantum attacks has become increasingly important.

The next iteration of secure communication is thus quantum communication and quantum cryptography, which explores the use of quantum phenomena to enable secure and efficient transmission of information [75, 76]. It leverages the principles of quantum mechanics, such as the superposition principle, uncertainty, entanglement, and the no-cloning theorem, to achieve novel communication protocols that offer unprecedented levels of security and information capacity. One of the most studied aspects of quantum communication is quantum key distribution (QKD), where the main objective is to securely share a secret key between two parties. QKD protocols exploit the principles of quantum mechanics to establish a shared secret key, which can be used for secure encryption and decryption of messages. The security of QKD lies in the fundamental laws of quantum physics, which make it impossible for an eavesdropper to intercept the key without being detected.

Charles Bennett and Gilles Brassard developed the first quantum key establishment protocol in 1984, known as BB84 [77]. They showed that the security relied on, first, the fact that quantum states cannot be copied (no-cloning theorem), and second, randomly encoding bits of information in mutually unbiased basis states. Since the inception of this field, there has been significant progress in the development of security proofs and methods for establishing secure key distribution rates. In addition, many other protocols have been developed and examined in pursuit of practical implementations of quantum key distributions. The original BB84 protocol will be described here using polarization as the encoding basis.

Suppose Alice has a message she wants to securely send to Bob, who is perhaps in a distant location. To encrypt the message, Alice and Bob will establish a random secret key generated via BB84. To begin, Alice and Bob agree upon a pair of *mutually unbiased bases* (MUB) with which to encode the key information. The standard pair of MUB using polarization states is $\mathcal{M}_0 = \{|H\rangle, |V\rangle\}$ and $\mathcal{M}_1 = \{|D\rangle, |A\rangle\}$. We use Dirac bra-ket notation as we are now dealing with single photon states. For two bases to be mutually unbiased, the projection of any state from one bases onto any state from the other should yield equal probabilities, i.e., no information. For a general set of j states $|u_i\rangle_j$ in basis

\mathcal{M}_i , this can be written as,

$$|_j \langle u_i | u_{i'} \rangle_{j'}|^2 = \begin{cases} \delta_{jj'}, & \forall i = i' \\ 1/d, & \forall i \neq i' \end{cases}, \quad (5.1)$$

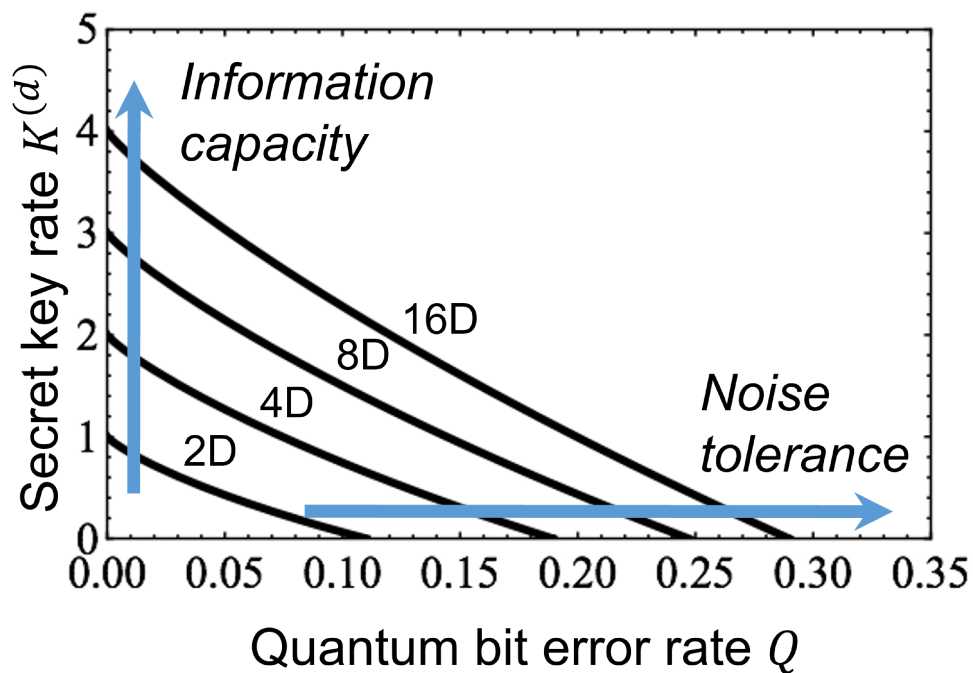
where d is the dimension of the encoding Hilbert space; $d = 2$ for polarization.

From the MUB, Alice and Bob establish their encoding alphabet for each state. One choice would be that $|H\rangle$ and $|D\rangle$ correspond to classical bit ‘0’, while $|V\rangle$ and $|A\rangle$ are classical bit ‘1’. Alice now begins the key exchange by i. randomly choosing a classical bit, and ii. randomly choosing a MUB to prepare a polarized photon accordingly. She sends the prepared photon over an untrusted quantum channel to Bob. This quantum channel could be optical fibres, free-space, or as will be discussed in this chapter, underwater. The channel is said to be untrusted since an eavesdropper could be ‘listening in’ on the key exchange process.

Upon receiving Alice’s photon through the channel, Bob will i. randomly choose a MUB to measure the state in, and ii. record either ‘0’ or ‘1’ depending on the result. This preparing and measuring of photons by Alice and Bob is repeated N times, after which the quantum part of this key distribution protocol is finished. Now Alice and Bob must distill their shared key from their respective strings of random 0’s and 1’s. This does not necessitate a secure channel nor a quantum one, but should at least be authenticated; for example, Alice and Bob call each other on the phone. We say that they will sift out the incorrect bits by comparing *only* the bases they respectively prepared and measured in. The incorrect bits are the instances when Alice and Bob prepared and measured in the wrong basis. Thus, for an infinitely long key, $1/2$ of the photons are sifted out, and the remaining classical bit string is the shared secret key.

In an ideal world at this stage, Alice and Bob would have identical keys; however, due to interference during the key distribution step—malicious or otherwise—there might be errors in the keys. While more often than not the quantum channel is simply noisy, any errors must be attributed to a possible attack from an eavesdropper to gain information. Alice and Bob thus must sacrifice a small portion of their key and directly compare each bit to estimate the errors in the whole key. These errors make up the quantum bit error rate (QBER) of the channel. The beauty of QKD protocols is that they have an error threshold; if the QBER is lower than this threshold, then Alice and Bob are 100% certain that their key is secure. In 2-dimensional BB84, such as with polarization, the error threshold is $Q_{\text{threshold}}^{(2)} = 11\%$, at which point no positive secret key rate K is possible.

For a d -dimensional BB84 protocol that uses qudits as opposed to qubits—for example, encoding using OAM states—the secret key rate after privacy amplification as a function

Figure 5.1: BB84 secret key rate plots for $d = 2, 4, 8, 16$.

of QBER Q is [78],

$$K^{(d)}(Q) = \log_2(d) - 2h^{(d)}(Q), \quad (5.2)$$

where,

$$h^{(d)}(Q) = -Q \log_2 \left(\frac{Q}{d-1} \right) - (1-Q) \log_2(1-Q), \quad (5.3)$$

is the d -dimensional Shannon entropy. Of note, the error threshold $Q_{\text{threshold}}^{(d)}$ is the error for which $K^{(d)} = 0$. Figure 5.1 plots the secret key rate for various dimensions; for $d = 3$, $Q_{\text{threshold}}^{(3)} = 15.95\%$, and for $d = 4$, $Q_{\text{threshold}}^{(4)} = 18.93\%$.

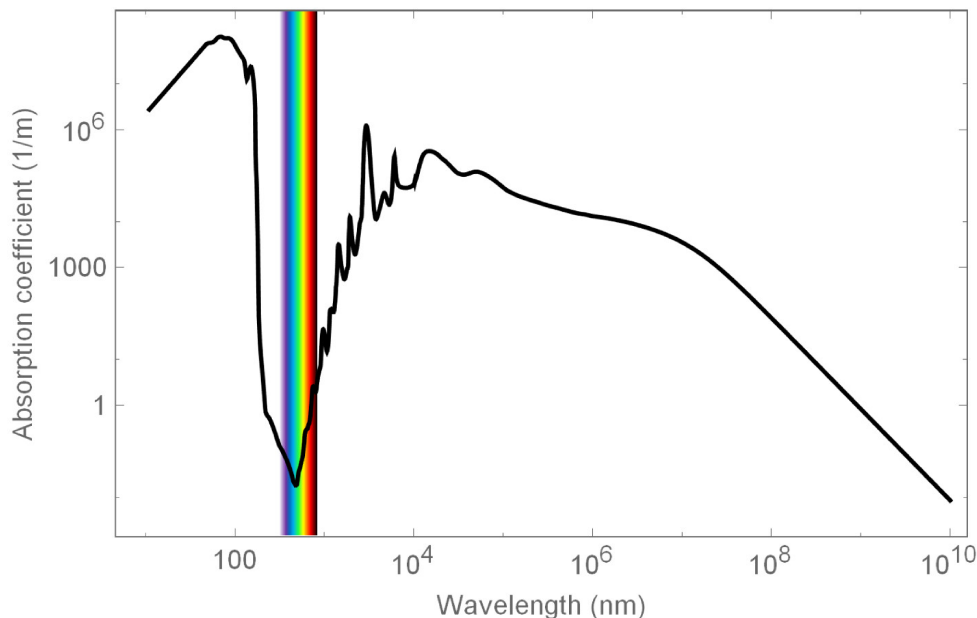


Figure 5.2: Absorption spectrum of water in the visible regime. Source: data from [3]

5.2 Underwater channel

5.2.1 Optical properties

Quantum communication through water presents unique challenges due to the nature of the underwater environment. The transmission of quantum information through water is complicated by factors such as high absorption, scattering, and signal distortion. Optical attenuation from both scattering and absorption is very wavelength dependent, and we can combine their effects into a total attenuation coefficient $a(\lambda) = a_{abs}(\lambda) + a_{sc}(\lambda)$. Beer's law is used to determine the output optical intensity through the channel given an input intensity of I_0 by $I(L) = I_0 e^{-c(\lambda)L}$. Signal distortions via underwater turbulence will be described in the next section.

Unlike air and optical fibres which have very large transparency windows—in which many of today's communication technologies are cross-compatible, e.g., the telecom wavelengths—water is highly absorbing in the near-IR and IR, with a narrow transparency window in the visible, due to vibrational modes of the water molecules. The absorption spectrum of water is shown in Figure 5.2. The minimum is around 480 nm with an ab-

sorption coefficient of $a_{abs}(480 \text{ nm}) = 0.0186 \text{ m}^{-1}$. This minimum may shift depending on the type and purity of the water. It is evident here that the visible wavelengths, particularly around the blue-green range, provide the best opportunity to transmit optical signals for long distances, limited as that is to a few hundred meters. Water also contains suspended particles, such as sediment and organic plant matter, which can also absorb and scatter light. In particular, we can get both Rayleigh scattering ($d < \lambda$) and Mie scattering ($d \gg \lambda$), defined by the size d of the scattering particle with respect to the radiation wavelength λ . The details of absorption and scattering from water particulates is beyond the scope of this thesis.

5.2.2 Turbulence

As once stated by Richard Feynman [79], “Turbulence is the most important unsolved problem in classical physics.” Indeed, while on his deathbed, Werner Heisenberg was asked what he would ask God, to which he replied [80], “When I meet God, I am going to ask him two questions: Why relativity? And why turbulence? I really believe he will have an answer for the first.” A similar quote has also been attributed to Sir Horace Lamb [79]. With what started as the carefully drawn depictions of vortices on the surface of moving water by Leonardo da Vinci, the ability to predict turbulent behaviour still challenges physicists and mathematicians alike today. However, this is not to say that we do not have a working framework for the mechanisms underlying turbulence.

The discussions in this section are applicable to any fluid, not just water or air. To start, the behaviour of a flowing fluid can be described as either laminar or turbulent, depending on the relation between the fluid’s viscosity and the flow’s inertia. Laminar flow is the regime in which the motion of the particles in the fluid all move in one direction in an orderly fashion—there is no motion perpendicular to the flow direction—hence the name laminar, as the fluid flows in smooth layers or laminations. Laminar flow is observed, for example, in water from a slightly open faucet, or air flow over an airplane’s wing. Turbulent flow, on the other hand, is the regime in which eddies and vortices form, giving rise to chaotic and unpredictable motion. Principally, turbulent flow can appear when there are differences at an interface; this interface could be formed from contrasting velocities, densities, temperature or contamination, to name a few. Of course, there is a third regime for the transitional behaviours in between laminar and turbulent flow. The flow regime can be determined by calculating the Reynolds number, which is the ratio of inertia to viscous forces,

$$R = \frac{\rho v L}{\mu}, \quad (5.4)$$

where ρ is the density of the fluid, v is the flow speed, L is the characteristic linear dimension of the system containing the fluid (e.g. diameter of a pipe), and μ is the fluid viscosity. While the exact numbers depend on the particular system, typically, a small Reynolds number corresponds to laminar flow and a large Reynolds number corresponds to turbulent flow. In a pipe, for example, the flow is laminar for $R < 2000$ and turbulent for $R > 4000$ [81]. For low viscous fluids, such as water and air, it is much easier to reach the turbulent regime as compared to very viscous fluids, such as honey or molasses.

While Reynolds' number classifies *when* a fluid flow is turbulent, it does not answer *what* and *how* it happens. For this, there is the underlying mechanism of how energy dissipates at different length scales. Indeed, Lewis F. Richardson—a mathematician, physicist and meteorologist—succinctly surmised his ideas on the energy cascade theory behind turbulent behaviour in his following poem [82]: *Big whirls have lesser whirls that feed on their velocity, and little whirls have lesser whirls and so on to viscosity.* This encapsulates the theory that kinetic energy is cascaded from large-scale, unstable structures (eddies, vortices, whirls) of size L_0 that break into smaller-scale structures of size l_0 until the energy is dissipated as heat at the smallest length scale of turbulence, where viscosity dominates. This smallest, characteristic size η is also termed the Kolmogorov length scale, after mathematician Andrey Kolmogorov who concretely formulated the statistical framework to describe the apparent randomness and chaos in turbulence.

Kolmogorov postulated that, at the small-scale, the energetics or energy spectrum of the eddies is universal, regardless of observed dynamics, depending only on the kinematic viscosity (μ/ρ) [83]. This means that, on the small-scale, the statistics are isotropic and homogeneous, unlike the large-scale structures. Recently, it was shown that this universality holds true even for transitional flows [84]. The reader is referred to [85, 86] for comprehensive reviews of Kolmogorov theory and other turbulence theories. Here, we will concentrate on the implications that turbulence has on a propagating beam of light. As noted above, turbulent flows are caused by the presence of small differences—density, temperature, impurities, etc—which translate to small fluctuations in the local refractive index of the medium. When light propagates through these fluctuations, different parts of the beam will be slightly deflected in different directions. This results in the displacement and distortion of the beam for weak turbulence, and speckle patterns for strong turbulence. Under the assumption that the fluctuations in refractive index are statistically homogeneous and isotropic, a spatial power spectrum $\Phi_n(\kappa)$ can be used to describe the distribution of spatial frequencies/wavenumbers κ for a given turbulent medium. Depending on the medium, $\Phi_n(\kappa)$ can depend on different parameters. For the case of atmosphere, these are parameters such as wavelength, channel length, and the atmospheric structure constant C_n^2 which describes the strength of the turbulence across a horizontal link. The atmospheric

spatial power spectrum, also known as the Kolmogorov power-law spectrum, is [87],

$$\Phi_n^{air}(\kappa) = 0.033C_n^2\kappa^{-11/3}, \quad 1/L_0 \ll \kappa \ll 1/l_0. \quad (5.5)$$

For a horizontal optical free-space link, C_n^2 (units of $\text{m}^{-2/3}$) can be calculated as,

$$r_0 = \left[0.423 \left(\frac{2\pi}{\lambda} \right)^2 C_n^2 L \right]^{-3/5}, \quad (5.6)$$

where r_0 (units of m) is the coherence length or Fried parameter, describing the average size of an air cell through which a wavefront remains plane. Together, C_n^2 and r_0 (which can be experimentally measured) are two quantities that are useful for quantifying the turbulence in a given link.

For water—ocean water, specifically—there are several more parameters affecting the refractive index fluctuations: the Kolmogorov length scale η ; the rate of dissipation of turbulent kinetic energy per unit mass of fluid ϵ (ranging from $10^{-2} \text{ m}^2/\text{s}^3$ to $10^{-8} \text{ m}^2/\text{s}^3$); the rate of dissipation of mean-square temperature χ_T (ranging from $10^{-4} \text{ K}^2/\text{s}$ to $10^{-10} \text{ K}^2/\text{s}$); and the ratio of temperature to salinity contributions to the refractive index spectrum w (ranging from -5 for dominating temperature-induced to 0 for dominating salinity-induced optical turbulence). The spatial power spectrum for ocean water is then [88],

$$\begin{aligned} \Phi_n^{ocean}(\kappa) = & 0.388 \times 10^{-8} \epsilon^{-1/3} \kappa^{-11/3} [1 + 2.35(\kappa\eta)^{2/3}] \\ & \times \frac{\chi_T}{w^2} (w^2 e^{-A_T\delta} + e^{-A_S\delta} - 2w e^{-A_{TS}\delta}), \end{aligned} \quad (5.7)$$

where $A_T = 1.863 \times 10^{-2}$, $A_S = 1.9 \times 10^{-4}$, $A_{TS} = 9.41 \times 10^{-3}$, and $\delta = 8.284(\kappa\eta)^{4/3}$.

From this rather unwieldy equation, it is not immediately obvious what the equivalent quantities for C_n^2 and r_0 are. For the Fried parameter, since $\Phi_n^{air}(\kappa)$ and $\Phi_n^{ocean}(\kappa)$ follow the same power-law—that is, the exponents on κ are both $-11/3$ —then the same formulations for r_0 in air can be used for water [89]. r_0 can be experimentally measured from the average deflection angle of the beam from the axis of propagation. C_n^2 , on the other hand, requires a bit more mathematical gymnastics to obtain an oceanic equivalent. As proposed in [90], it is possible to formulate an equivalent oceanic structure constant by recognizing that the scintillation index, m^2 , of a spherical wave will be the same regardless of medium. The scintillation index is a fourth-order statistical quantity characterizing the normalized variance of the fluctuating intensity for a beam of light, commonly observed as the twinkling of stars. In particular, m^2 is dependent on $\Phi_n^{ocean}(\kappa)$ in the oceanic case, and C_n^2 for the

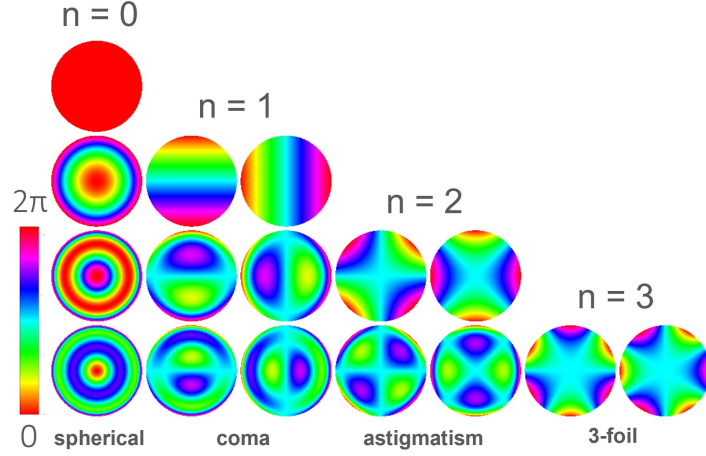


Figure 5.3: Phase profiles of Zernike polynomials.

atmospheric case; thus, an equivalence can be found by equating each scintillation index. The oceanic structure constant is then,

$$C_n^2 = 16\pi^2 k^{-7/6} L^{-11/6} \text{Re} \left\{ \int_0^L d\zeta \int_0^\infty \kappa d\kappa \left[E(\zeta, \kappa) \times E(\zeta, -\kappa) + |E(\zeta, \kappa)|^2 \Phi_n^{ocean}(\kappa) \right] \right\}, \quad (5.8)$$

where,

$$E(\zeta, \kappa) = ik \exp \left[-\frac{i\zeta(L - \zeta)\kappa^2}{2kL} \right], \quad (5.9)$$

is the field of the spherical wavefront propagating along the horizontal direction ζ . Typical values of C_n^2 range from $\approx 10^{-13} \text{ m}^{-2/3}$ corresponding to strong turbulence to $\approx 10^{-17} \text{ m}^{-2/3}$ corresponding to weak turbulence.

In terms of quantum communication schemes, turbulence may have a detrimental effect on the transmitted information depending on the strength. It is particularly degrading for spatial modes, where we require that the phase and amplitude profiles remain intact across the channel. Beyond deflections and distortions, strong turbulence can even cause singularity splitting for modes carrying OAM [91, 92]. While metrics such as C_n^2 and r_0 are useful for knowing the strength of turbulence in a channel, characterizing the turbulence in terms of its different effects is more useful when one wishes to eventually compensate for it with adaptive optics methods. The Zernike polynomials provide a quantitative measure

for these distortions and aberrations. These polynomials $Z_j(r, \phi)$ form a set of orthonormal polynomials on the unit disk [93],

$$Z_j(r, \phi) = \begin{cases} \sqrt{n+1}R_n^m(r)\sqrt{2}\cos(m\phi), & m \neq 0 \\ \sqrt{n+1}R_n^m(r)\sqrt{2}\sin(m\phi), & m \neq 0, \\ \sqrt{n+1}R_n^0(r), & m = 0 \end{cases} \quad (5.10)$$

where $j = 1 + (n(n+2) + m)/2$ is the Noll index with radial and azimuthal degree n and m , respectively. $R_n^m(r)$ are the radial polynomials,



$$R_n^m(r) = \begin{cases} \sum_{b=0}^{(n-m)/2} \frac{(-1)^b(n-b)!}{b!(\frac{n+m}{2}-b)!(\frac{n-m}{2}-b)!} r^{n-2b}, & (n-m) \text{ even,} \\ 0, & (n-m) \text{ odd.} \end{cases} \quad (5.11)$$

Figure 5.3 shows the phase profiles of the first few aberration orders. The first order aberrations ($n=1$) correspond to tip-tilt effects, while the second order aberrations ($n=2$) correspond to defocusing and astigmatism. It is possible to experimentally measure the Zernike coefficients for a distorted wavefront using, for example, a Shack–Hartmann wavefront sensor, which is a lenslet array that measures the local deflection of the wavefront.

What follows from here are the published works [1, 2] which explore the feasibility of quantum key distribution in an uncontrolled outdoor underwater channel, as well as through a more controlled flume tank. Of note, due to all the particulate matter in the Ottawa River, only a channel length of only 5 m was achievable. Liquid-crystal q -plates are employed to encode information and also to probe the effect of turbulence on vector vortex beams.



Characterization of an underwater channel for quantum communications in the Ottawa River

FELIX HUFNAGEL,¹ ALICIA SIT,^{1,*} FLORENCE GRENAPIN,¹
FRÉDÉRIC BOUCHARD,¹ KHABAT HESHAMI,^{1,2} DUNCAN ENGLAND,²
YINGWEN ZHANG,¹ BENJAMIN J. SUSSMAN,^{1,2} ROBERT W.
BOYD,^{1,3}  GERD LEUCHS,^{1,3} AND EBRAHIM KARIMI^{1,2,3} 

¹*Department of Physics, University of Ottawa, 25 Templeton, Ottawa, Ontario, K1N 6N5, Canada*

²*National Research Council of Canada, 100 Sussex Drive, Ottawa, Ontario K1A 0R6, Canada*

³*Max Planck Institute for the Science of Light, Staudtstr. 2, D-91058 Erlangen, Germany*

Abstract: We examine the propagation of optical beams possessing different polarization states and spatial modes through the Ottawa River in Canada. A Shack-Hartmann wavefront sensor is used to record the distorted beam's wavefront. The turbulence in the underwater channel is analysed, and associated Zernike coefficients are obtained in real-time. Finally, we explore the feasibility of transmitting polarization states as well as spatial modes through the underwater channel for applications in quantum cryptography.

© 2019 Optical Society of America under the terms of the [OSA Open Access Publishing Agreement](#)

1. Introduction

There are several different methods employed today for communicating underwater. The most widely used method is acoustic, capable of transmitting information over many kilometres [1]; however, the transmission rate is on the order of kilobits per second, limited by the speed of sound in water as well as the modulation rate of acoustic signals [2]. A second method is to use radio-frequency (RF) signals, which can be easily incorporated into current communication networks. This technique is limited to communication distances on the order of several meters due to high absorption in water at radio frequencies. Both the acoustic and RF implementations suffer from the necessity of bulky and expensive equipment for both transmitting and receiving signals. Over the last decade, using the optical domain for underwater communication has gained increasing interest [3,4]. With an optimal transmission window between blue and green (400-550 nm) wavelengths, a propagation distance between 50-200 m in clear water can be reached [5]. Higher data rates should additionally be achievable - up to gigabits per second depending on the scheme - allowing for larger data transfers and real-time communication. In [6], a data rate of 20 Mbps, at a distance of 200 m, has been experimentally achieved.

In a realistic aquatic environment, there are several other factors beyond absorption which can limit the distance and quality of a marine optical communication link, i.e. scattering and turbulence. Scattering in water is dependent on the density and the size of particles in the channel and will contribute significantly to attenuation and therefore to the maximum achievable distance. Scattering is separated into two types: Mie scattering for particles on the order of the wavelength of the light, and Rayleigh scattering for particles much smaller than the wavelength [7]. Especially in water where there are relatively large plankton and mineral particles floating in the water, Mie scattering will have to be considered, along with Rayleigh scattering, due to the water molecules [8]. Another limiting factor when it comes to an actual implementation of an optical link is turbulence [9,10]. A spatially varying index of refraction from temperature and salinity differences through the optical link can result in beam wander as well as higher order distortion effects on the propagating beam. This can contribute both to loss and errors in the transmitted

signal. In optical communication, security—affected by factors such as errors in the channel—is an important feature for successful information transfer. Typically, a line-of-sight approach is implemented, making eavesdropping much more difficult, as opposed to the broadcasting method for acoustic and RF communication where the signal is sent in all directions. By considering quantum cryptographic schemes, the security can be further enhanced [11]; for instance, quantum key distribution (QKD) allows authorized partners to communicate with unconditional security [12–14].

There are several different optical degrees of freedom which can be used to encode information in these QKD protocols. A popular option for direct line-of-sight channels is the polarization of photons, with successful experiments in free-space [15,16]. One limitation with polarization, however, is its inherently limited 2-dimensional Hilbert space, allowing for the maximum transmission of one bit per photon. The orbital angular momentum (OAM) degree of freedom of light, on the other hand, provides the potential of an unbounded state space, and thus unbounded encryption alphabet. Light beams carrying OAM possess a helical wavefront with ℓ intertwined helices, i.e. $\exp(i\ell\phi)$ where ℓ is an integer number and ϕ is the transverse azimuthal angle in polar coordinates [17]. These beams possess a doughnut-shaped intensity profile due to the presence of a phase singularity at their centre (ϕ is undefined at the origin in cylindrical polar coordinates). The unbounded state space of these spatial modes allow us to implement high-dimensional quantum communication channels [18–21], but they do come with unique challenges. One key challenge that has been observed with free-space communication is that turbulence in the channel can introduce errors in the transmitted information [22]. The measurement of OAM states is heavily dependent on the position of the incoming beam and thus these states are much more prone to errors from turbulence than polarization states which must just maintain their orientation.

Underwater quantum communications have been numerically investigated [23] and experimentally demonstrated in laboratory conditions using polarization [24,25], in outdoor conditions using the OAM degree of freedom [26], and over a 55 m water channel using polarization [27] and spatial modes [28]. These experimental investigations have lead to several numerical investigations of QKD in underwater channels [29–31]. In this Letter, we investigate the propagation of light through the Ottawa River in Canada's capital. In particular, we analyze the underwater turbulence by looking at the distorted wavefront and associated Zernike coefficients both obtained from a Shack-Hartmann wavefront sensor. Furthermore, we explore the transmission of polarization states of light and spatial modes of light through the underwater channel for quantum cryptography applications.

2. Experiment

The experiments presented here were conducted through the Ottawa River (latitude = 45.541048, longitude = -76.565719) during late August 2018. The water temperature was on average 20° C for the duration of the experiment. However, the ambient temperature varied significantly from the middle of the day to the middle of the night. This contributed to turbulent conditions with water at the surface being heated or cooled more than the water below. Of course since it is a river, there were already naturally varying currents, which moved the water through the beams propagation path resulting in a changing index of refraction.

The results discussed in this work were taken using a 532 nm laser diode. The sender and receiver units were mounted on breadboards along the shoreline of the river. As shown in Fig. 1, the sender consisted of the laser, Spatial Light Modulator (SLM), and a half-wave plate. The wave-plates were used to prepare four linear polarization states, i.e. horizontal (H), vertical (V), anti-diagonal (A), and diagonal (D). The SLM is used for preparing the OAM states. This is done by displaying a phase hologram on the SLM and selecting the first diffracted mode from the hologram. The laser beam is then sent from Alice's breadboard on shore to the first periscope

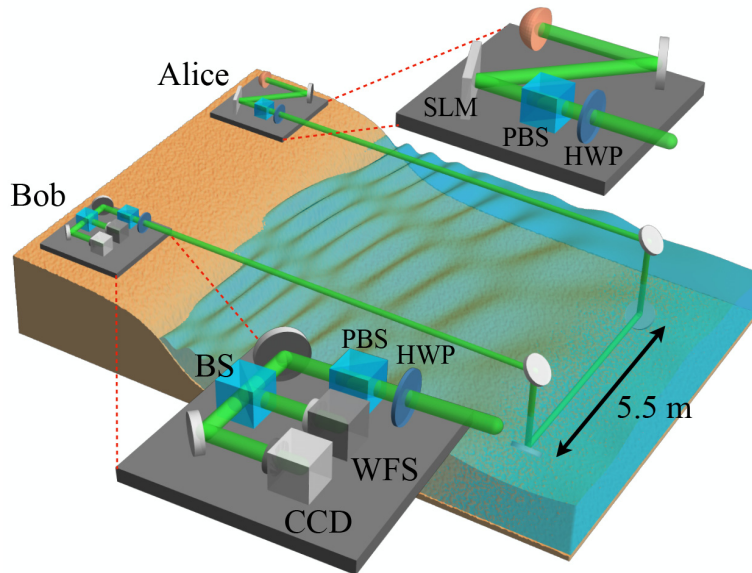


Fig. 1. Experimental setup. Two breadboards positioned on the beach are used for the sender and receiver, Alice and Bob respectively. A CW laser at $\lambda = 532$ nm is sent to an SLM, polarizing beamsplitter (PBS), and half-wave plate (HWP) for state preparation at Alice's side of the link. This is then sent to a first periscope (composed of two mirrors) which brings the beam underwater, where it propagates to the second periscope 5.5 m away. The receiver has a PBS and HWP for polarization measurements, and a beam splitter allows a CCD camera and Shack-Hartmann wavefront sensor (WFS) to take images.

system that brings the beam underwater. The beam then propagates underwater, parallel to the beach, to the second periscope system where it is brought out of the water and sent to the receiver unit, see Fig. 1. In order to eliminate air-water perturbations resulting from surface waves as the beam enters the water, a glass tube, closed at one end, is inserted within the periscope system to create an air-glass-water interface. At the receiver side, we captured the intensity of the beam for the polarization states of H, V, A, and D using a CCD camera. The camera only allows us to gain intensity information about the beam but not the phase. However in order to measure the phase of the beam, we place a Shack-Hartmann wavefront sensor (WFS) at the receiver. This device is made up of a micro-lens array placed in front of a CCD camera. The resulting effect is that the phase at each lens can be determined by the focus point of that lens on the CCD array. This allows one to determine the incidence angle of the given region of the beam and thus the phase relative to the rest of the beam. The accuracy of the wavefront sensor is limited by the number of micro-lenses in the array; the WFS that we use is the Thorlabs WFS20-7AR and has a 23×23 lenslet array with lenslet pitch of $150 \mu\text{m}$ and focal length of 5.2 mm.

Losses in the link due to scattering played a much larger roll in establishing a quantum channel than was expected. There has been analysis performed looking at the feasibility of quantum communication taking into account many factors including scattering [23]. These studies, however, consider at worst the Jerlov Type III ocean water with scattering loss of 1.3 dB/m. In our river channel, the total attenuation was significantly larger than these previously studied values. The channel losses from scattering varied over the course of many hours due to different magnitudes of waves in the river which brought sediment from the river bed into the beam path. During the polarization experiment, the total absorption was measured to be 5.4 dB/m,

significantly higher than even the worst water type considered in the previous calculations. This makes the absorption loss of 0.13 dB/m for pure water negligible for practical considerations of achievable distance [32]. Due to the large amount of scattering in the river, our experimental tests were limited to ~5 m. This high level of scattering was primarily due to large particles in the water ($d \gg \lambda$). The Mie scattering model is used when the particles' diameter is on the same order as the wavelength of the light. This is typically for particles such as pollen, dust, and water droplets which are approximately the same size as the wavelength of the light. In our channel, since we were near the shore of the river, there was even larger visible plant matter and dirt floating in the water. This resulted in a large amount of light being absorbed or back reflected as opposed to being primarily forward scattered as in the regular Mie scattering regime.

$ H\rangle$	0.93	0.06	0.40	0.59
$ V\rangle$	0.02	0.97	0.45	0.54
$ A\rangle$	0.49	0.50	0.97	0.03
$ D\rangle$	0.53	0.47	0.04	0.96
	$ H\rangle$	$ V\rangle$	$ A\rangle$	$ D\rangle$

Fig. 2. Polarization probability-of-detection matrix. The sender generates the linear polarization states of $\{|H\rangle, |V\rangle\}$ or $\{|A\rangle, |D\rangle\}$, chosen at random. The receiver randomly picks up one of the bases $\{|H\rangle, |V\rangle\}$ or $\{|A\rangle, |D\rangle\}$, and records the projection probability, whose numerical values are shown.

3. Results and discussion

The first goal of this project was to establish that polarization QKD could be achieved in this highly turbulent and highly scattering channel. For the original BB84 protocol [12], polarization states are chosen from a set of mutually unbiased bases (MUBs). We chose the bases to be $|\psi_i\rangle = \{|H\rangle, |V\rangle\}$ and $|\phi_i\rangle = \{|A\rangle, |D\rangle\}$.

The defining property of MUBs is that a measurement in the correct basis reveals with certainty the state that the photon was in, while measurement in the wrong basis gives no information about the state of the photon, i.e. $|\langle\psi_i|\phi_k\rangle|^2 = 1/2$. Herein lies the security of QKD: an eavesdropper making a measurement in the wrong basis will be successful only 50% of the time and will introduce errors when they are unsuccessful. The experimental probability-of-detection matrix for the polarization states is shown in Fig. 2. The discrepancy between the error rates of the $|H\rangle$ and $|V\rangle$ polarization are primarily due to imperfect polarization optics. This is not expected to be a property of the underwater channel. The resultant error rate is 4.01 %, which is below the threshold of 11.0 % necessary to perform QKD with a 2-dimensional BB84 protocol. The results here are obtained using classical light from a CW laser. However, on the assumption that the

background noise is small compared with the signal and thus the errors are introduced only by the channel, single photons will give the same error rate and we can calculate a bit rate of 0.52 bits per sifted photon.

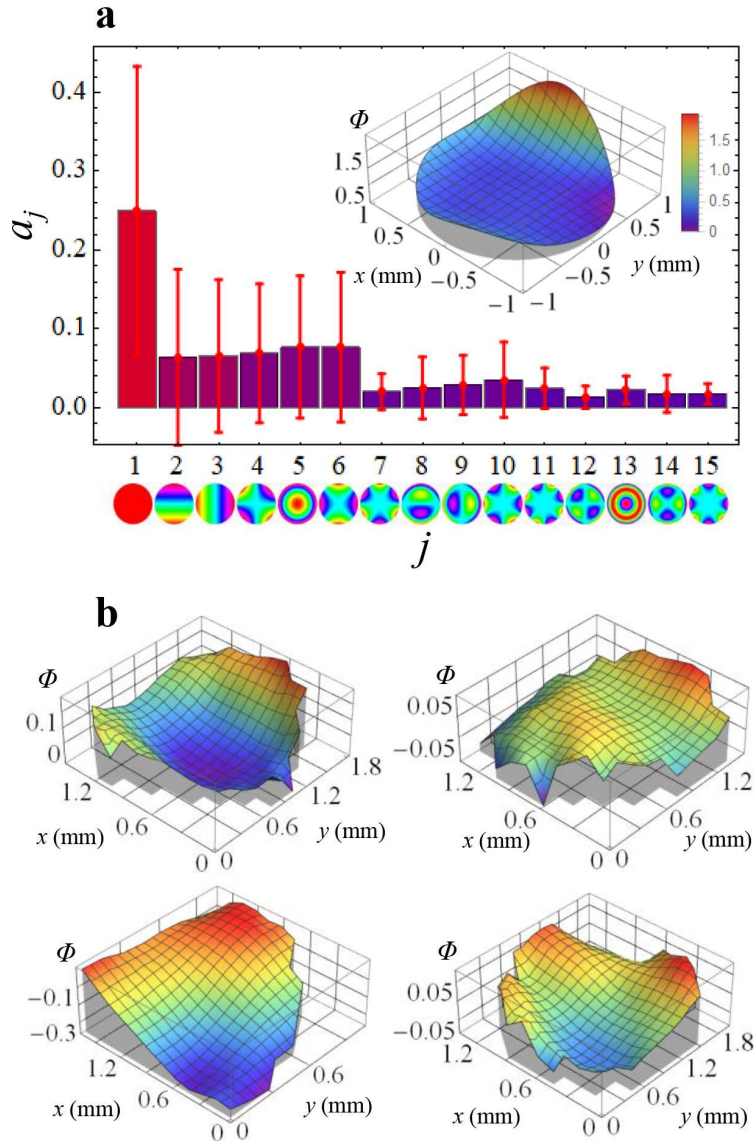


Fig. 3. Wavefront measurements. A Gaussian beam is sent through the underwater channel to measure the wavefront. Plot **a** shows the average value for the magnitude of the Zernike coefficients taken from the wavefront sensor. The coefficients are separated by their radial degree corresponding to the color bars. of The inset is a plot of the wavefront given by these values. The plots in **b** are wavefronts measured at different times of a gaussian beam through the 5 m underwater link. The wavefront measurements are taken using an array of $150 \mu\text{m}$ diameter lenses.

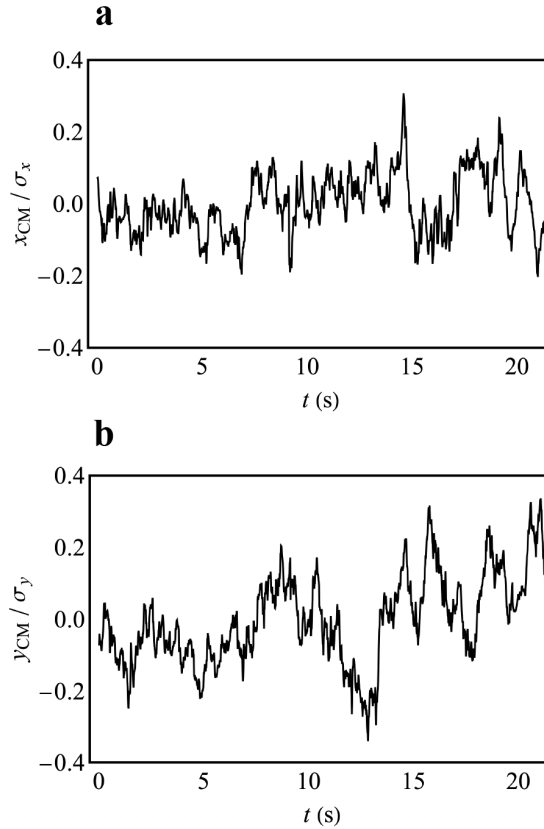


Fig. 4. Time dependence of tip-tilt aberrations. The intensity of a Gaussian beam was measured at the receiver using a CCD camera. The tip-tilt variations were then calculated by measuring the positional shift (x,y) of the Gaussian beam from the center. The x and y center of mass, relative to their respective beam waists σ_x and σ_y , are plotted as a function of time in **a** and **b**, respectively.

Although we achieved an error rate below the threshold, there are some residual errors in the system. In free space experiments, the errors are often attributed to optical turbulence, which comes from differences in the index of refraction along the path of propagation as described by the Kolmogorov theory of turbulence [33]. Tip-tilt effects can result in beam wandering, while higher order effects can be present in high turbulence situations, resulting in distortion of the beam's profile [26,34]. The aberrations in the beam are often visible in the intensity of the beam; however, more precise information lies in the phase of the received beam. In this experiment, we prepared a Gaussian beam at the sender, and measure the wavefront at the receiver. The Gaussian beam is the simplest for measuring the turbulence introduced by the channel, though OAM modes or any modes whose phase profile is known can be used. The Gaussian beam should have a spherical phase due to divergence; thus, any variations from this can be attributed to turbulence introduced by the water. From the wavefront measurements, the turbulence can be expanded in terms of the Zernike coefficients, i.e. $\Phi(r, \phi) = \sum_j a_j Z_j(r, \phi)$. Here, r and ϕ are the radial and azimuthal polar coordinates, respectively; a_j are the Zernike expansion coefficients; $Z_j(r, \phi) = Z_n^m(r, \phi)$ are the Zernike polynomials depicted underneath the x-axis of Fig. 3a; $j = 1 + (n(n+2) + m)/2$ is the Noll index; and n and m are the radial and azimuthal

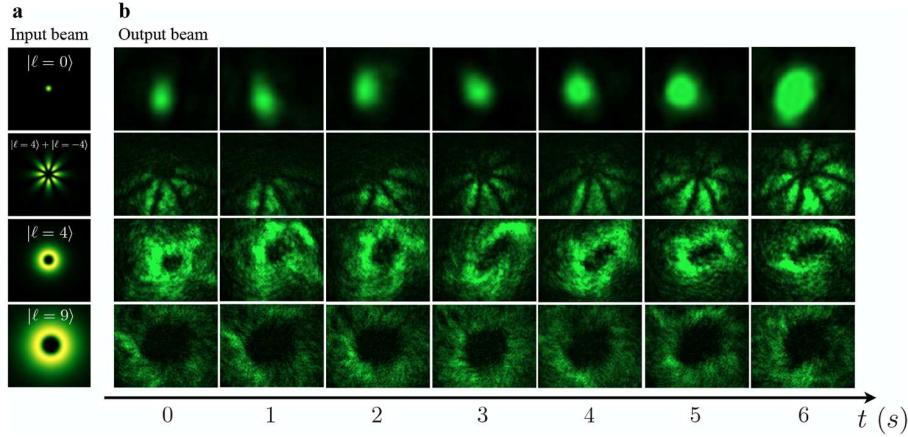


Fig. 5. Observed turbulence effects on spatial modes. The images in the first, second, third and fourth rows correspond to $LG_{0,0}$, $(LG_{4,0} + LG_{-4,0})/\sqrt{2}$, $LG_{4,0}$, and $LG_{9,0}$, respectively. The original beam profile is shown in **a**, and the images after propagation through the underwater channel are shown in **b**. The images are taken over a 6 second interval. The exposure time for the last three rows are set to 108 ms, while it is set to 20 ms for the Gaussian beam. The inhomogeneity in the beams' intensity profiles are due primarily to Mie scattering from floating objects in the underwater channel. Lower and higher-order aberrations are manifested in the beam wandering ($LG_{0,0}$) and singularity splitting.

indices, respectively. The values for the first 15 Zernike coefficients averaged from 30 wavefront measurements \bar{a}_j are shown in Fig. 3-a along with the reconstructed wavefront Φ from these values. The wavefront measurements are taken with an average exposure time of 60 milliseconds and are separated by 10 seconds. The time separation of the wavefront measurements is large with respect to the fluctuation of the Zernike coefficients. Thus, each wavefront is essentially an independent measurement of the turbulence in the channel. In Fig. 3-b, a sample of four of these individual wavefront measurements is shown. These wavefront measurements show that the beam experienced significant variation upon propagation through the turbulent channel. It is also interesting to consider the time dependence of the turbulence in the channel. This is necessary if one plans to implement an adaptive optics system to correct for wavefront aberrations in the optical channel. The intensity profile of a Gaussian beam was recorded to analyze the tip tilt fluctuations as a function of time. This is shown in Fig. 4. The frequency of the fluctuations in the underwater channel is lower than one typically observes in free space channels. This could make underwater channels an interesting test bed for adaptive optics systems.

As stated before, the turbulence is also visible in the intensity profile of the beam at the receiver. It is easy to see tip-tilt aberrations from a Gaussian beam as it visibly drifts across the x and y axis of a camera. The higher order aberrations are often less visible. These aberrations do, however, show themselves very clearly in their effect on higher-order spatial modes. Specifically, the oblique and vertical astigmatism ($Z_2^{\pm 2}(r, \phi)$) stretch OAM modes, giving them an elliptical shape, as well as splitting the singularity into lower topological charges. Intensity profiles of OAM and superposition modes are shown in Fig. 5 with consecutive images taken over a time of 6 seconds. The turbulence from the channel is very apparent in the wandering of the $LG_{0,0}$ mode, and the higher-order aberrations are shown most clearly in the stretching of the $LG_{0,4}$ mode. In addition to turbulence, all of the modes experience significant intensity fluctuations from changing levels of scattering as well as from objects floating into the beam's path. The latter is displayed clearly in the images of the petal beam, i.e. $(LG_{0,4} + LG_{0,-4})/\sqrt{2}$. As the

correct measurement of spatial modes requires that the position and phase of the beam remain intact, it is clear that, even over a short propagation through water, active wavefront correction or the implementation of adaptive optics would be required to compensate for the aberrations.

4. Conclusion

We have shown that significant challenges present themselves in underwater communication. Despite low absorption from the water at blue-green wavelengths, the scattering from floating particles in the water can severely limit the achievable communication distance. Though scattering will impact the distance, we see that polarization states do maintain their integrity even after propagation through a very highly scattering channel. The second key challenge in an underwater optical channel is turbulence. This has the largest impact on communications using spatial modes. Through the 5.5 m channel, the OAM modes experience aberrations which will result in errors in a communication protocol. The magnitude of these errors will need to be investigated in future work. Adaptive optics techniques will also need to be investigated to compensate for these errors and allow for communication using spatial modes.

Funding

Canada Research Chairs; Canada Foundation for Innovation; Canada First Research Excellence Fund; Natural Sciences and Engineering Research Council of Canada.

Acknowledgments

This work was supported by Canada Research Chairs (CRC); Canada Foundation for Innovation (CFI); Canada First Research Excellence Fund (CFREF); Natural Sciences and Engineering Research Council of Canada (NSERC). We thank Denis Guay and the NRC for their help in designing and building the periscopes.

References

1. M. Stojanovic, *Acoustic (underwater) communications* Wiley Encyclopedia of Telecommunications, 2003.
2. J. Heidemann, W. Ye, J. Wills, A. Syed, and Y. Li, Research challenges and applications for underwater sensor networking, in *IEEE Wireless Communications and Networking Conference WCNC, 2006*, 1, 228–235, (2006).
3. T. Wiener and S. Karp, “The role of blue/green laser systems in strategic submarine communications,” *IEEE Trans. Commun.* **28**(9), 1602–1607 (1980).
4. J. C. Brock and S. J. Purkis, “The emerging role of lidar remote sensing in coastal research and resource management,” *J. Coastal Res.* **10053**, 1–5 (2009).
5. Z. Zeng, S. Fu, H. Zhang, Y. Dong, and J. Cheng, “A survey of underwater optical wireless communications,” *IEEE Commun. Surv. Tutorials* **19**(1), 204–238 (2017).
6. S. Fasham and S. Dunn, “Developments in subsea wireless communications,” in *IEEE Underwater Technology (UT)* (IEEE, 2015), pp. 1–5.
7. H. C. Hulst and H. C. van de Hulst, *Light scattering by small particles* (Courier Corporation, 1981).
8. C. D. Mobley, *Light and water: radiative transfer in natural waters* (Academic, 1994).
9. G. Nootz, E. Jarosz, F. R. Dalgleish, and W. Hou, “Quantification of optical turbulence in the ocean and its effects on beam propagation,” *Appl. Opt.* **55**(31), 8813–8820 (2016).
10. G. Nootz, S. Matt, A. Kanaev, K. P. Judd, and W. Hou, “Experimental and numerical study of underwater beam propagation in a Rayleigh–Bénard turbulence tank,” *Appl. Opt.* **56**(22), 6065–6072 (2017).
11. J. Uhlmann, M. Lanzagorta, and S. E. Venegas-Andraca, “Quantum communications in the maritime environment,” in *OCEANS 2015 - MTS/IEEE Washington* (IEEE, 2015) 1–10
12. C. H. Bennett and G. Brassard, Quantum cryptography: public key distribution and coin tossing, in *Int. Conf. on Comput. Syst. Signal Process.* (IEEE, 1984), pp. 175–179.
13. N. Gisin, G. Ribordy, W. Tittel, and H. Zbinden, “Quantum cryptography,” *Rev. Mod. Phys.* **74**(1), 145–195 (2002).
14. V. Scarani, H. Bechmann-Pasquinucci, N. J. Cerf, M. Dušek, N. Lütkenhaus, and M. Peev, “The security of practical quantum key distribution,” *Rev. Mod. Phys.* **81**(3), 1301–1350 (2009).
15. T. Schmitt-Manderbach, H. Weier, M. Fürst, R. Ursin, F. Tiefenbacher, T. Scheidl, J. Perdigues, Z. Sodnik, C. Kurtsiefer, J. G. Rarity, A. Zeilinger, and H. Weinfurter, “Experimental demonstration of free-space decoy-state quantum key distribution over 144 km,” *Phys. Rev. Lett.* **98**(1), 010504 (2007).

16. S.-K. Liao, W.-Q. Cai, W.-Y. Liu, L. Zhang, Y. Li, J.-G. Ren, J. Yin, Q. Shen, Y. Cao, Z.-P. Li, F.-Z. Li, X.-W. Chen, L.-H. Sun, J.-J. Jia, J.-C. Wu, X.-J. Jiang, J.-F. Wang, Y.-M. Huang, Q. Wang, Y.-L. Zhou, L. Deng, T. Xi, L. Ma, T. Hu, Q. Zhang, Y.-A. Chen, N.-L. Liu, X.-B. Wang, Z.-C. Zhu, C.-Y. Lu, R. Shu, C.-Z. Peng, J.-Y. Wang, and J.-W. Pan, "Satellite-to-ground quantum key distribution," *Nature* **549**(7670), 43–47 (2017).
17. L. Allen, M. W. Beijersbergen, R. Spreeuw, and J. Woerdman, "Orbital angular momentum of light and the transformation of Laguerre-Gaussian laser modes," *Phys. Rev. A* **45**(11), 8185–8189 (1992).
18. M. Mafu, A. Dudley, S. Goyal, D. Giovannini, M. McLaren, M. J. Padgett, T. Konrad, F. Petruccione, N. Lütkenhaus, and A. Forbes, "Higher-dimensional orbital-angular-momentum-based quantum key distribution with mutually unbiased bases," *Phys. Rev. A* **88**(3), 032305 (2013).
19. M. Mirhosseini, O. S. Magaña-Loaiza, M. N. O'Sullivan, B. Rodenburg, M. Malik, M. P. Lavery, M. J. Padgett, D. J. Gauthier, and R. W. Boyd, "High-dimensional quantum cryptography with twisted light," *New J. Phys.* **17**(3), 033033 (2015).
20. A. Sit, F. Bouchard, R. Fickler, J. Gagnon-Bischoff, H. Larocque, K. Heshami, D. Elser, C. Peuntinger, K. Gunthner, B. Heim, C. Marquardt, G. Leuchs, R. W. Boyd, and E. Karimi, "High-dimensional intricacy quantum cryptography with structured photons," *Optica* **4**(9), 1006–1010 (2017).
21. F. Bouchard, K. Heshami, D. England, R. Fickler, R. W. Boyd, B.-G. Englert, L. L. Sánchez-Soto, and E. Karimi, "Experimental investigation of high-dimensional quantum key distribution protocols with twisted photons," *Quantum* **2**, 111 (2018).
22. M. Krenn, R. Fickler, M. Fink, J. Handsteiner, M. Malik, T. Scheidl, R. Ursin, and A. Zeilinger, "Communication with spatially modulated light through turbulent air across vienna," *New J. Phys.* **16**(11), 113028 (2014).
23. P. Shi, S.-C. Zhao, Y.-J. Gu, and W.-D. Li, "Channel analysis for single photon underwater free space quantum key distribution," *J. Opt. Soc. Am. A* **32**(3), 349–356 (2015).
24. L. Ji, J. Gao, A.-L. Yang, Z. Feng, X.-F. Lin, Z.-G. Li, and X.-M. Jin, "Towards quantum communications in free-space seawater," *Opt. Express* **25**(17), 19795–19806 (2017).
25. S. Zhao, W. Li, Y. Shen, Y. Yu, X. Han, H. Zeng, M. Cai, T. Qian, S. Wang, Z. Wang, Y. Xiao, and Y. Gu, "Experimental investigation of quantum key distribution over water channel," *Appl. Opt.* **58**(14), 3902–3907 (2019).
26. F. Bouchard, A. Sit, F. Hufnagel, A. Abbas, Y. Zhang, K. Heshami, R. Fickler, C. Marquardt, G. Leuchs, R. W. Boyd, and E. Karimi, "Quantum cryptography with twisted photons through an outdoor underwater channel," *Opt. Express* **26**(17), 22563–22573 (2018).
27. C.-Q. Hu, Z.-Q. Yan, J. Gao, Z.-Q. Jiao, Z.-M. Li, W.-G. Shen, Y. Chen, R.-J. Ren, L.-F. Qiao, A.-L. Yang, H. Tang, and X.-M. Jin, "Transmission of photonic polarization states through 55-meter water: Towards air-to-sea quantum communication," arXiv preprint arXiv:1811.11176 (2018).
28. Y. Chen, W.-G. Shen, Z.-M. Li, C.-Q. Hu, Z.-Q. Yan, Z.-Q. Jiao, J. Gao, M.-M. Cao, K. Sun, and X.-M. Jin, "Underwater transmission of high-dimensional twisted photons over 55 meters," arXiv preprint arXiv:1902.01392 (2019).
29. S. Tarantino, D. Cozzolino, K. Rottwitt, and D. Bacco, Feasibility of quantum communications in aquatic scenario, in *2018 IEEE Photonics Conference (IPC)*, (IEEE, 2018), pp. 1–2.
30. B. Guo, G. Yuan, J. Yu, H. Liu, W. Xu, and R. Hou, "Simulations and measurements of polarization states changing in underwater laser transmission," *Proc. SPIE* **10850**, 108500U (2018).
31. J. Gariano and I. B. Djordjevic, "Theoretical study of a submarine to submarine quantum key distribution systems," *Opt. Express* **27**(3), 3055–3064 (2019).
32. R. C. Smith and K. S. Baker, "Optical properties of the clearest natural waters (200–800 nm)," *Appl. Opt.* **20**(2), 177–184 (1981).
33. A. N. Kolmogorov, "The local structure of turbulence in incompressible viscous fluid for very large Reynolds numbers," *Akademiia Nauk SSSR Doklady* **30**, 299–303 (1941).
34. Y. Ren, L. Li, Z. Wang, S. M. Kamali, E. Arbabi, A. Arbabi, Z. Zhao, G. Xie, Y. Cao, N. Ahmed, Y. Yan, C. Liu, A. J. Willner, S. Ashrafi, M. Tur, A. Faraon, and A. E. Willner, "Orbital angular momentum-based space division multiplexing for high-capacity underwater optical communications," *Sci. Rep.* **6**(1), 33306 (2016).

PAPER • OPEN ACCESS

Investigation of underwater quantum channels in a 30 meter flume tank using structured photons

To cite this article: Felix Hufnagel *et al* 2020 *New J. Phys.* **22** 093074

View the [article online](#) for updates and enhancements.

You may also like

- [Roadmap on multimode photonics](#)
Ilaria Cristiani, Cosimo Lacava, Georg Rademacher et al.
- [Light based underwater wireless communications](#)
Hassan M. Oubei, Chao Shen, Abia Kammoun et al.
- [Roadmap on structured light](#)
Halina Rubinsztein-Dunlop, Andrew Forbes, M V Berry et al.



PAPER

OPEN ACCESS



RECEIVED
19 April 2020REVISED
18 August 2020ACCEPTED FOR PUBLICATION
9 September 2020PUBLISHED
23 September 2020

Original content from
this work may be used
under the terms of the
[Creative Commons
Attribution 4.0 licence](#).

Any further distribution
of this work must
maintain attribution to
the author(s) and the
title of the work, journal
citation and DOI.



Investigation of underwater quantum channels in a 30 meter flume tank using structured photons

Felix Hufnagel¹, Alicia Sit¹, Frédéric Bouchard^{1,2}, Yingwen Zhang², Duncan England²,
Khabat Heshami^{1,2} , Benjamin J Sussman^{1,2} and Ebrahim Karimi^{1,2,*} ¹ Department of physics, University of Ottawa, Advanced Research Complex, 25 Templeton Street, K1N 6N5, Ottawa, ON, Canada² National Research Council of Canada, 100 Sussex Drive, Ottawa, Ontario K1A 0R6, Canada

* Author to whom any correspondence should be addressed.

E-mail: ekarimi@uottawa.ca**Keywords:** quantum communication, underwater communication link, vector vortex modes

Abstract

Underwater quantum communication has recently been explored using polarization and orbital angular momentum (OAM). Here, we show that spatially structured modes, e.g., a coherent superposition of beams carrying both polarization and OAM, can also be used for underwater quantum cryptography. We also use the polarization degree of freedom to investigate the impact of the channel length on key rates for quantum communication applications. The underwater channel proves to be a difficult environment for establishing quantum communication as underwater optical turbulence results in significant beam wandering and distortions. However, the errors associated to the turbulence do not result in error rates above the threshold for establishing a positive key in a quantum communication link with both the polarization and spatially structured photons. The impact of the underwater channel on the spatially structured modes is also investigated at different distances using polarization tomography.

1. Introduction

The development of quantum computers and their ability to factor large prime numbers through Shor's algorithm, poses a threat to modern communication security [1]. Since the realization of the first protocol by Bennett and Brassard in 1984 (BB84), quantum key distribution (QKD) has become the most actively researched solution for secure communication in a post-quantum world [2]. At present, quantum communication is a research field reaching maturity with commercial devices available for optical fibre QKD, experimental demonstrations of satellite-to-ground channels [3, 4], and new protocols being developed to improve key rates and security [5]. There are two primary quantum communication instances currently investigated: quantum communication channels and quantum communication protocols [6–8]. Channels must be experimentally investigated to demonstrate the transmission fidelity of quantum states, while new protocols bring advantages in terms of security, error tolerance, and key rates.

Many different protocols have been developed, some of which take advantage of high-dimensional quantum states [9]. Although quantum information is typically encoded using one of the different photonic degrees of freedom (such as polarization, time-bin, position and transverse momentum), multiple degrees of freedom can be used, forming structured states of light. The coherent combination of polarization and orbital angular momentum (OAM) is one example of structured light, with numerous applications in microscopy, optical tweezers, classical communication, and quantum information [10]. QKD protocols performed across free-space channels have been implemented, for example, with polarization [11], time-bin [12], OAM [13], and structured photons [14, 15]. Likewise, there have been similar demonstrations in fibre channels [16–19]. Though two-dimensional qubit protocols are the most commonly implemented, there are advantages to high-dimensional communication in both noise tolerance [20] and bit-rate [21] which motivates the study of structured states [22].

Recently, there have been several studies demonstrating quantum communication tasks in underwater environments [23–27], motivated by the goal of secure communication between submersibles, research vessels, and surface vehicles. The absorption of water at radio frequencies has resulted in acoustic technology being the dominant form of communication for the last 100 years. There exists a transparency window in the blue-green wavelengths with the minimum absorption around 480 nm, giving the possibility of optical and quantum communication at these wavelengths. Theoretical works predict a maximum practical quantum channel length of 300 m at 418 nm in clear conditions [28, 29]. This theoretical work investigates the clearest ocean waters for scattering losses, and takes into account errors introduced from scattering and background light from the sky. Another in depth work considers different types of vertical and horizontal channels taking into account many factors including scattering, background light for different daytime and nighttime conditions, and the receiver's acceptance angle [30]. Daytime communication can be established; however the achievable distances are significantly reduced. Though this is a short distance as compared to the current fibre and free-space links, it is enough for communication between submersibles and surface vehicles. Thus far, the feasibility tests of QKD with polarization encoding has been performed through a 3 m tube of water [24], and through an indoor testing channel of 55 m [26]. However much like in air, uncontrolled underwater channels are prone to the effects of turbulence—caused by local changes in the refractive index of water from temperature variations—which displaces and distorts a transmitted beam of light. Recent studies have explored the effects of underwater turbulence on QKD protocols and spatial modes of light in uncontrolled [23] and natural [25] water channels. However, the security analysis of different protocols is not considered in these previous studies. The high loss nature of underwater channels makes the optimization of the protocol necessary to achieve maximum distances and key rates. Here, we investigate an underwater channel at various lengths up to 30 m. The turbulence impact on the channel is observed through polarization tomography of the spatial modes, showing mode degradation upon propagation through the water. The BB84 protocol is tested using both polarization states and two-dimensional spatially structured modes. Key rate analysis is performed showing how optimization of the protocol's parameters is important in the high loss scenarios observed in underwater channels. Moreover the variable channel length gives us a real-world look into the scaling of such quantum protocols, and the impact on the key rates.

2. Experiment

The experimental setup consists of a sender (Alice) and receiver (Bob), as well as the flume tank which provides our underwater channel, see figure 1. The flume is 1 meter wide and 1 meter tall; its full length was 50 m. On the top of the flume was a track with a mounted trolley which can travel the length of the channel. Alice's setup was placed on the trolley such that the channel length could be adjusted from 1 m to the full 50 m. A periscope was hung from Alice's setup so that, with proper beam alignment, the trolley could be moved up and down the length of the flume while maintaining some beam coupling to a single mode optical fibre at the receiver. This allowed for the beam pointing from Alice's setup to remain fixed, while the coupling was optimized at Bob's setup after each change in the channel distance. The setup was left for 5 minutes after moving the trolley to allow the periscope vibrations and disturbances in the water to settle. The sender consisted of two configurations for changing between sending polarization states and sending the spatially structured modes, e.g., vector vortex modes [31]. For sending polarization states, a 532 nm, 4.5 mW collimated diode-pumped laser was sent to a PBS, followed by a half-wave plate ($\lambda/2$) and a quarter-wave plate ($\lambda/4$) to allow any polarization state to be generated. An intensity modulator was not used to separate the signal into discrete pulses. Before being transmitted across the channel, the appropriate neutral density filters attenuated the beam to achieve a mean photon number of 0.1 photons per nanosecond. The vector vortex modes were generated by adding a q -plate with a topological charge of $q = 1/2$ after the polarization optics. At the receiver, the beam is initially collected by a three-inch lens so that the whole beam is gathered even with slight beam wandering due to the underwater turbulence. The beam then passes through a $\lambda/2$ and $\lambda/4$ waveplate and then a PBS to project on a particular polarization state. The beam is then coupled to a single mode fibre connected to a SPAD detector. The SPAD detectors have a 32 ns dead time and peak quantum efficiency of 65% (around 50% at 532 nm). To detect the vector vortex states, a q -plate with charge $q = 1/2$ is placed at the receiver before the polarization optics. In this way, the detection system mirrors the generation system. The setup is initially optimized with the trolley placed at 1 m from the receiver.

Linear polarization states are used to establish the polarization quantum communication channel. The two mutually unbiased bases (MUB) for encryption are $|\psi_i\rangle \in \{|H\rangle, |V\rangle\}$ and $|\phi_j\rangle \in \{|A\rangle = \frac{1}{\sqrt{2}}(|H\rangle + |V\rangle), |D\rangle = \frac{1}{\sqrt{2}}(|H\rangle - |V\rangle)\}$, respectively. MUB possess the property that a projection made on the incorrect basis results in no information gained about the state of the photon, i.e. a

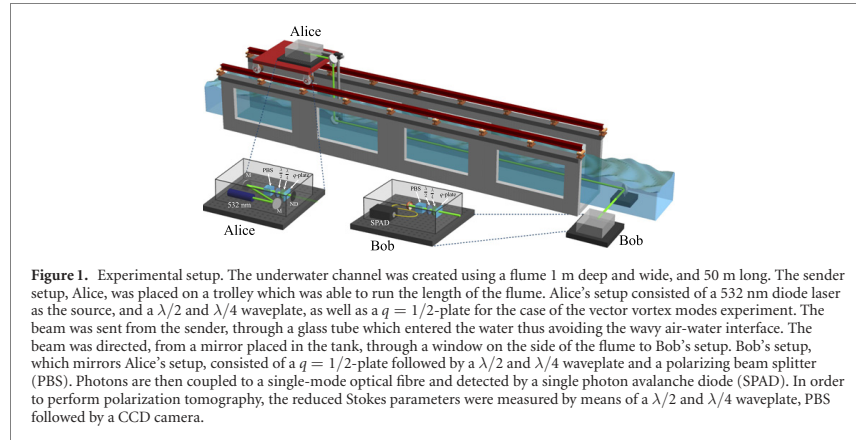


Table 1. QBER and key rates for polarization BB84. QBER and key rates per sifted photon for the polarization BB84 protocol are measured at different propagation distances. Note that in principle, the polarisation states can be modulated and detected at 100 MHz, and thus the actual key rate is *key rate per sifted photons* \times *modulation rate* \times *sifting efficiency*.

Distance	0.5 m	10.5 m	20.5 m	30.5 m
QBER (%)	0.27	0.74	3.7	0.96
Key rate	0.94	0.87	0.54	0.84
Signal (Hz)	3.1×10^6	6.7×10^5	6.2×10^4	2.8×10^4

probability of $1/2$ for each state $|\langle \psi_i | \phi_j \rangle|^2 = 1/2$. A full probability-of-detection matrix is determined by sending each of the four polarization states and subsequently performing projective measurements of the four states at the receiver setup. This probability-of-detection matrix gives us the quantum bit error rate (QBER) which is used to calculate the key rate that can be achieved with the underwater channel. The uniformly polarized photons, i.e. $|\psi_i\rangle$ and $|\phi_j\rangle$, should remain largely unaffected by the turbulence because water is not a birefringent medium. Thus, the introduced errors will be negligible for short distances. The length of the channel and level of turbulence will, however, introduce more losses as the photons are not able to be gathered at the receiver. This will have some effect on the measured error rate since the losses in the signal will give more weight to the dark counts and background noise as the distance increases.

The QBER and key rates for the different distances are given in table 1. The results show the QBER increasing slightly as the channel length is increased. The primary source of these increased errors is the losses that result from the turbulence at the longer distances. The type of experiment we performed involves projecting on one of the polarization states and recording the number of counts during a set time period. The unpredictable nature of the turbulence in the channel results in some periods of time having larger losses due to beam wandering and spatial distortions. The beam wandering and spatial distortions, of course, increase with distance, but are effectively random and difficult to predict in our uncontrolled environment. This effect, which is random, results in the high error rate observed for the 20.5 m channel in comparison with the other channel lengths.

The structured photon states, here, vector vortex modes, are generated at the sender, and detected at the receiver by adding q -plates to the setup—details are given in the caption of figure 1. q -plates are patterned liquid crystal devices which introduce a polarization dependent geometric phase across the plate when it is illuminated with circularly polarized beams [32, 33]. The transformation of a perfectly tuned $q = 1/2$ -plate in the circular polarization basis, left-circular \mathbf{e}_L and right-circular \mathbf{e}_R states, can be described as,

$$\begin{pmatrix} \mathbf{e}_L \\ \mathbf{e}_R \end{pmatrix} \rightarrow \begin{pmatrix} \mathbf{e}_R e^{i\phi} \\ \mathbf{e}_L e^{-i\phi} \end{pmatrix}. \quad (1)$$

where ϕ is the azimuthal coordinate. As we can see from the above equation, the $q = 1/2$ -plate will act on circular polarization states by converting left circularly polarized photons to right circularly polarized

Table 2. QBER and key rates for a two-dimensional BB84 using vector vortex beam. QBER and key rates per sifted photon for the vector vortex modes protocol are measured at different propagation distances. Note that in principle the mode generation and detection can be achieved by polarisation modulators at 100 MHz before (after) q -plates, and thus the actual key rate is *key rate per sifted photons* \times *modulation rate* \times *sifting efficiency*.

Distance	1.5 m	5.5 m	10.5 m
QBER (%)	1.44	3.4	1.0
Key rate	0.79	0.57	0.84
Signal (Hz)	2.6×10^6	1.9×10^6	9.4×10^5

photons with OAM of $\ell = +1$. Similarly, incident photons with right circular polarization will be converted to left circular with OAM of the opposite sign, i.e. $\ell = -1$. The states used for our structured QKD protocol are created by sending linear polarization states, $\{|H\rangle, |V\rangle\}, \{|A\rangle, |D\rangle\}$, onto the $q = 1/2$ -plate. This results in a state that has a spatially dependent polarization in the form of radial, azimuthal, clockwise and counterclockwise sink topology, all possessing polarization topological charge of $+1$ [31]. This is opposed to the case when a circular polarization state is sent to the q -plate resulting in uniform conversion to the opposite circular polarization and the addition of an OAM of $\ell = \pm 1$. The protocol we implemented uses the structured modes as a two-dimensional Hilbert space. The first MUB contained the radial and azimuthal states, i.e.,

$$|\Psi_i\rangle \in \left\{ \frac{(|L, -1\rangle + |R, +1\rangle)}{\sqrt{2}}, \frac{(|L, -1\rangle - |R, +1\rangle)}{\sqrt{2}} \right\}, \quad (2)$$

where $|\pi, \ell\rangle$ indicates the photons with polarization and OAM states of $|\pi\rangle$ and $|\ell\rangle$, respectively. The states for the second MUB were the polarization patterns in the form of clockwise and counterclockwise sinks (vortex) which were generated by sending the $|A\rangle$ and $|D\rangle$ polarization states onto the $q = 1/2$ -plate, i.e.,

$$|\Phi_i\rangle \in \left\{ \frac{(|L, -1\rangle + i|R, +1\rangle)}{\sqrt{2}}, \frac{(|L, -1\rangle - i|R, +1\rangle)}{\sqrt{2}} \right\}. \quad (3)$$

The combination of polarization, e.g., $\{|H\rangle, |V\rangle\}$ and OAM, e.g., $\{-1, +1\}$ can be used as a four-dimensional Hilbert space for high-dimensional QKD [15]. To avoid errors assigned to high-dimensional generation and detection schemes [9, 34], we compare the two-dimensional spatial modes with the polarization states. The vector vortex modes in equations (2) and (3) were used to establish a quantum channel at 1, 5, and 10 meter distances. The difficulty with alignment of these spatial modes restricted us from coupling to single mode fibre for distances longer than 10 meters. The QBER and consequent key rates for these channels are given in table 2.

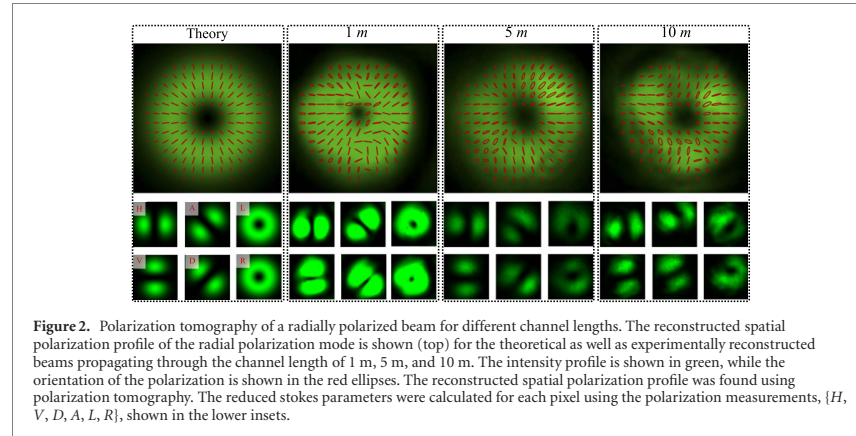
We also study the effect of underwater turbulence on the spatial profile of vector vortex modes propagating through different channel lengths. We perform polarization tomography by measuring the intensity of the structured beam, using a CCD camera, after passing a polarizer for $\{H, V, A, D, R, L\}$. From these measurements, the polarization is reconstructed pixel-by-pixel. The state sent across the channel is the radial polarization state. This is created by sending a vertical linearly polarized Gaussian beam onto the $q = 1/2$ plate. The resultant spin-orbit state is $(|L, -1\rangle + |R, +1\rangle)/\sqrt{2}$. The theoretical polarization profile as well as the measured profiles for 1, 5, and 10 meters is shown in figure 2. The spatial profile can be seen to degrade as the channel length increases. This is associated to turbulence in the water channel that increases by the length [23, 25]. The phase distortion associated to the turbulence includes not only tip-tilt aberrations, but also higher-order effects such as astigmatism to the spatial profile of the beam. The aberrations in the underwater scenario are slower than those observed in air free-space, and thus the astigmatism aberrations are more easily seen as opposed to the scintillation often observed in high turbulence cases in the air.

3. Key rate analysis

The initial BB84 proposal is an ideal protocol in which real single photons guarantee that there are not multiple photons in any given state which could open a door for an eavesdropping attack, i.e., photon number splitting attack [35]. For the BB84 protocol the number of bits that can be gained from each signal is,

$$G = \frac{1}{2}Q(1 - 2H(e)), \quad (4)$$

where Q is the gain and $H(e) = -e\log_2(e) - (1 - e)\log_2(1 - e)$ is the Shannon entropy for the error rate e . This ideal BB84 key rate requires some assumptions that are often not valid in practical QKD situations.



The first of these assumption is the use of real single photons, i.e., heralded pairs, as opposed to an attenuated laser source. An attenuated laser source is a much more practical implementation, as photon pairs generated through spontaneous parametric down conversion SPDC are not deterministic. When using an attenuated source, the main point of weakness to consider is the possibility of more than one photon in a pulse. Other practical factors to consider are the effect of imperfect detectors and channel losses. These are brought into consideration in modern security proofs done for practical QKD protocols. We implement the decoy state protocol in our key rate analysis [36]. In any protocol using an attenuated laser source, one must choose the pulse mean photon number (μ). This μ is taken below 1 such that the Poisson distribution gives a low probability of a two-photon state. The density matrix of this signal state is given as,

$$\rho = \sum_{i=0}^{\infty} \frac{\mu^i}{i!} e^{-\mu} |i\rangle \langle i|. \quad (5)$$

Here $|i\rangle$ is the Fock state, denoting i number of photons. In the decoy state protocol, we include another state, the decoy state, which has a different mean photon number (ν). The key rate for the decoy state protocol is given by,

$$K = \frac{1}{2} \{-Q_{\mu} f(E_{\mu}) H(E_{\mu}) + Q_1 (1 - H(e_1))\}, \quad (6)$$

where Q_{μ} is the gain of the total signal state sent by Alice, E_{μ} is the signal state QBER, Q_1 is the gain of the single photon state, e_1 is the error rate of the single photon state, and f is the error correction efficiency. Q_1 and e_1 are respectively lower and upper bounded by,

$$Q_1 \geq \frac{\mu^2 e^{-\mu}}{\mu\nu - \nu^2} \left(Q_{\nu} e^{\nu} - Q_{\mu} e^{\mu} \frac{\nu^2}{\mu^2} - \frac{\mu^2 - \nu^2}{\mu^2} Y_0 \right), \quad (7)$$

$$e_1 \leq \frac{E_{\nu} Q_{\nu} e^{\nu} - Y_0/2}{Q_1 \nu / (\mu e^{-\mu})}. \quad (8)$$

Here, Y_0 is the background rate per pulse, Q_{ν} is decoy state gain and E_{ν} is the decoy state QBER. We can optimize the values of μ and ν for different values of loss (channel distance), given the parameters associated to our channel. The values for the detector efficiency, darkcounts, channel loss, and Bob's detection efficiency measured for our underwater polarization channels are given in table 3. These parameters can be used to calculate the values of μ and ν , which will yield the optimal key rate for different distances. The optimal values of μ and ν for the optimal zero-error case are 1.0 and 0.001 respectively. The optimal value of μ decreases with higher error rates, while ν increases. This optimal key rate is plotted in figure 3 as the channel length, i.e., attenuation, is increased. The optimal key rate is shown in black accounting for errors resulting from dark counts only. It should be noted that finite key effects have not been included in this calculation. The experimental data points which add the measured QBER to the background errors are shown in red for the channel lengths of 0.5, 10.5, 20.5, and 30.5 meters. The achievable key rates of the experimental points fall below the theoretical line as expected. However, the key

Table 3. Experimental parameters of the underwater polarization channel.

Parameter	Dark counts	Source rep rate	Detector efficiency	Bob's detection efficiency	Channel Loss (α)
Flume result	300 Hz	10^9 Hz	0.6	0.188	0.57 dB m^{-1}

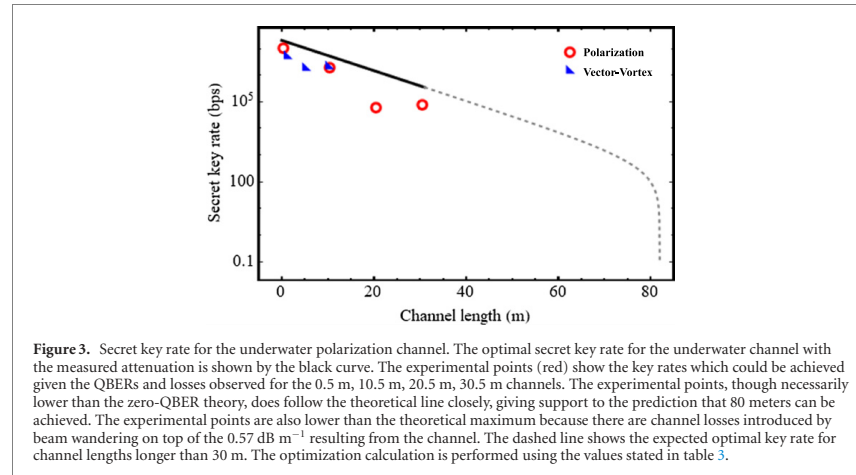


Figure 3. Secret key rate for the underwater polarization channel. The optimal secret key rate for the underwater channel with the measured attenuation is shown by the black curve. The experimental points (red) show the key rates which could be achieved given the QBERs and losses observed for the 0.5 m, 10.5 m, 20.5 m, 30.5 m channels. The experimental points, though necessarily lower than the zero-QBER theory, does follow the theoretical line closely, giving support to the prediction that 80 meters can be achieved. The experimental points are also lower than the theoretical maximum because there are channel losses introduced by beam wandering on top of the 0.57 dB m^{-1} resulting from the channel. The dashed line shows the expected optimal key rate for channel lengths longer than 30 m. The optimization calculation is performed using the values stated in table 3.

rates do closely follow the trend depicted by the theory, suggesting that a channel length near 80 meters could be successfully established with these channel parameters. The key rate analysis for the vector vortex modes follows the exact method demonstrated for the polarization states. The only change is the experimentally observed QBER, which have similar values to those of the polarization channels of the similar length—on the order of 1% for 10 m—and thus results in similar key rates. For example, the key rate for the ~ 30 meter channel of vector vortex modes is expected to be ~ 70 Kbps.

4. Conclusion and outlook


We have studied a turbulent underwater channel for quantum communication using polarization and vector vortex modes, beams having spatially structured polarization states. Both the polarization and vector vortex modes maintained their fidelity upon propagation through the channel, resulting in sufficiently low error rates (QBER) to achieve a secure quantum channel. The turbulence—primarily beam wandering—introduces significant challenges with alignment and coupling to single mode fibre. In our channel, the beam path is near the surface of the water for the entire length which results in relatively high turbulence due to the temperature gradient at the air-water surface. Thus channels operating at greater depths may see less turbulence than observed here. Despite these challenges we have shown that both polarization states and spatially structured polarization states can be used in an underwater free-space setting, and for establishing a positive secret key rate for lengths up to 30 meters. The alignment problems from turbulence as well as the difficulty presented by large attenuation present the greatest difficulties for underwater quantum communication. The implementation of automated beam tracking equipment would allow one to achieve longer channels approaching the lengths that have been theoretically proposed. In fact, the slower turbulence observed in an underwater channel makes this task of beam correction much easier than in a free-space air environment. The implementation of beam tracking and adaptive optics technologies also allow for the possibility of performing communication through the air-water interface where waves introduce significant fluctuations. We also performed key rate analysis taking into account the parameters measured in our channel. Given these parameters the maximum distance for secure communication would be 80 meters, though this is extremely dependent on the attenuation coefficient of the channel, and Bob's detection efficiency. Improvements in either of these areas would significantly extend the maximum achievable distance.

Acknowledgments

We would like to thank Nathalie Brunette, Michel Brassard, Yvan Brunet, and Tony Frade at the Ocean, Coastal and River Engineering Research Centre of National Research Council Canada for all of their efforts in helping us perform this research. This work was supported by Joint Centre for Extreme Photonics (JCEP), Canada Research Chairs (CRC), Canada First Excellence Research Fund (CFREF), and Ontario's Early Researcher Award. AS acknowledges the financial support of the Vanier graduate scholarship of the NSERC.

ORCID iDs

Khabat Heshami  <https://orcid.org/0000-0003-3864-1930>

Ebrahim Karimi  <https://orcid.org/0000-0002-8168-7304>

References

- [1] Shor P W 1994 Algorithms for quantum computation: discrete logarithms and factoring *Proc. 35th Annual Symp. on Foundations of Computer Science* 124–34
- [2] Bennett C H and Brassard G 1984 *Int. Conf. on Comput. Syst. Signal* pp 175–9
- [3] Vallone G, Bacco D, Dequal D, Gaiarin S, Luceri V, Bianco G and Villoresi P 2015 *Phys. Rev. Lett.* **115** 040502
- [4] Liao S K et al 2017 *Nature* **549** 43–7
- [5] Pirandola S et al 2019 arXiv:1906.01645
- [6] Leuchs G, Marquardt C, Sánchez-Soto L L and Strekalov D V 2020 *R & D Advances for Quantum Communication Systems Optical Fiber Telecommunications VII* ed A E Willner (New York: Academic) ch 12 pp 495–563
- [7] Ekert A K 1991 *Phys. Rev. Lett.* **67** 661
- [8] Bennett C H, Bessette F, Brassard G, Salvail L and Smolin J 1992 *J. Cryptol.* **5** 3–28
- [9] Bouchard F, Heshami K, England D, Fickler R, Boyd R W, Englert B G, Sánchez-Soto L L and Karimi E 2018 *Quantum* **2** 111
- [10] Rubinshtein-Dunlop H et al 2016 *Photonics Res.* **19** 013001
- [11] Buttler W, Hughes R, Kwiat P, Lamoreaux S, Luther G, Morgan G, Nordholt J, Peterson C and Simmons C 1998 *Phys. Rev. Lett.* **81** 3283
- [12] Jin J, Bourgoin J P, Tannous R, Agne S, Pugh C, Kuntz K, Higgins B and Jennewein T 2019 *Opt. Express* **27** 37214–23
- [13] Mirhosseini M, Magaña-Loaiza O S, O'Sullivan M N, Rodenburg B, Malik M, Lavery M P, Padgett M J, Gauthier D J and Boyd R W 2015 *New J. Phys.* **17** 033033
- [14] Vallone G, D'Ambrosio V, Sponselli A, Slussarenko S, Marrucci L, Sciarrino F and Villoresi P 2014 *Phys. Rev. Lett.* **113** 060503
- [15] Sit A et al 2017 *Optica* **4** 1006–10
- [16] Müller A, Breguet J and Gisin N 1993 *Europhys. Lett.* **23** 383
- [17] Marand C and Townsend P 1995 *Opt. Lett.* **20** 1695–7
- [18] Sit A et al 2018 *Opt. Lett.* **43** 4108–11
- [19] Xavier G and Lima G 2020 *Commun. Phys.* **3** 1–11
- [20] Ecker S et al 2019 *Phys. Rev. X* **9** 041042
- [21] Islam N T, Lim C C W, Cahall C, Kim J and Gauthier D J 2017 *Sci. Adv.* **3** e1701491
- [22] Cozzolino D, Da Lio B, Bacco D and Oxenlöwe L K 2019 *Adv. Quantum Technol.* **2** 1900038
- [23] Bouchard F et al 2018 *Opt. Express* **26** 22563–73
- [24] Zhao S et al 2019 *Appl. Opt.* **58** 3902–7
- [25] Hufnagel F et al 2019 *Opt. Express* **27** 26346–54
- [26] Hu C Q et al 2019 *Photonics Res.* **7** A40–4
- [27] Lanzagorta M 2012 *Synth. Lect. Commun.* **5** 1–129
- [28] Zhao S C, Han X H, Xiao Y, Shen Y, Gu Y J and Li W D 2019 *J. Opt. Soc. Am.* **36** 883–92
- [29] Sullivan S 1963 *J. Opt. Soc. Am.* **53** 962–8
- [30] Tarantino S, Da Lio B, Cozzolino D and Bacco D 2020 *Optik* **216** 164639
- [31] Cardano F, Karimi E, Slussarenko S, Marrucci L, de Lisi C and Santamato E 2012 *Appl. Opt.* **51** C1–6
- [32] Marrucci L, Manzo C and Paparo D 2006 *Phys. Rev. Lett.* **96** 163905
- [33] Larocque H, Gagnon-Bischoff J, Bouchard F, Fickler R, Upham J, Boyd R W and Karimi E 2016 *J. Opt.* **18** 124002
- [34] Zhu F, Tyler M, Valencia N H, Malik M and Leach J 2019 arXiv:1908.08943
- [35] Brassard G, Lütkenhaus N, Mor T and Sanders B C 2000 *Phys. Rev. Lett.* **85** 1330
- [36] Lo H K, Ma X and Chen K 2005 *Phys. Rev. Lett.* **94** 230504

Chapter 6

Conclusion

In summary, I have explored the unique physics that arise when nematic liquid crystals are twisted between two patterned glass plates. According to the theory for linearly twisted liquid crystals, there is the capability to create devices that demonstrate dual functionality depending on its orientation and effective phase retardation—which I have named *dual-plates*. An additional layer of intrigue arises when an electric field is externally applied to the twisted liquid crystals; in particular, the model which assumes a linear twist is no longer applicable. A genetic algorithm method was thus developed and rigorously implemented to numerically calculate the tilt and twist distributions of the liquid crystals within the cell. These distributions for a variety of externally applied voltages were then translated into an overall Jones matrix for the cell that could be used to probe its effects on polarized light. I fabricated various twisted liquid-crystal devices and compared their behaviour with the linear twist model and results of the genetic algorithm method. There is solid agreement in both cases—though the latter is a welcome surprise given additional assumptions and approximations that were made to reduce computation time. Liquid-crystal devices known as *q-plates* were also utilized for quantum key distribution through underwater channels.

While the story of my thesis formally ends here, there are still some questions that remain as studies for future works to whoever takes up the twisted-liquid-crystal mantle. The foremost that I raise is whether it is possible to vary the effective phase retardation of the twisted liquid crystal cell such that the twist distribution remains linear. One possible way would be to either heat up or cool down the sample, as the refractive index of the liquid crystals is also temperature dependent. This has already been demonstrated as a feasible method to tune conventional liquid-crystal *q-plates* [94]. Though, there would be the issues of how fast and how uniform this could be done, as well as what range of temperatures would be required. However, this would allow for the creation of dual-plates as I had first

intended, where their dual behaviour is toggled via a phase retardation of either $\Gamma = 0$ or $\Gamma = \pi$. As mentioned in Ch. 3, this could be of great benefit to some high-dimensional quantum key distribution protocols which encode using structured photons.

There are then a slew of (semi-)analytical and numerical questions to explore. For example, what dictates the ‘crossing-point’ when the twist distributions are no longer linear. Is this the same for all ϕ_m ? Or is it ϕ_m -dependent much like the threshold voltage. To that end, what would be a ‘correct’ semi-analytical formula to determine the maximum tilt angle $\theta_m(\phi_m, V)$? An even greater ask is whether a direct semi-analytical form for the tilt and twist distributions as a function of voltage is possible; there is some hint to this in [59] and merits further analysis. The hope would then be to only have to run the genetic algorithms for only one ϕ_m to generate its tilt and twist distributions, and thus extrapolate to the rest. Furthermore, is it possible to reverse engineer and determine what tilt and twist distributions are necessary to produce a particular output, i.e., what voltage? Even after going through this whole liquid crystal exercise, I do not possess an intuition as to why certain distributions give certain polarization transformations. In particular, what is the condition for which ‘detuned’ status is achieved, if at all, or what is the condition for which we have q -plate functionality and so-called topological charge ‘doubling’? What other phenomena can be generated from a single device that a symmetrically patterned device cannot recreate?

Thinking a bit more abstractly, this twisted nematic system provides a very exotic way to transform polarization states. Given that we have three independent degrees of freedom—total twist angle ϕ_m , the orientation and rotation of the physical sample, and the applied voltage V —it may be possible to create single-element general polarization transformations instead of the three- or four-element set of half- and quarter-wave plates. The construction of such a device where the total twist angle can be varied is a puzzle unto itself, but the theory may prove insightful. As to a spatially varying version along the lines of [29], that does not appear as straightforward using our current liquid crystal fabrication techniques.

Fin

References

- [1] F. Hufnagel, A. Sit, F. Grenapin, F. Bouchard, K. Heshami, D. England, Y. Zhang, B. J. Sussman, R. W. Boyd, G. Leuchs, and E. Karimi. Characterization of an underwater channel for quantum communication in the ottawa river. *Optics Express*, 27:26346–26354, 2019.
- [2] F. Hufnagel, A. Sit, F. Bouchard, Y. Zhang, D. England, K. Heshami, B. J. Sussman, and E. Karimi. Investigation of underwater quantum channel in a 30-meter flume tank using structured photons. *New Journal of Physics*, 22:093074, 2020.
- [3] D. J. Segelstein. *The complex refractive index of water*. Master’s thesis, University of Missouri-Kansas City, 1981.
- [4] P. G. De Gennes and J. Prost. *The Physics of Liquid Crystals*. Oxford: Clarendon Press, 2nd edition, 1993.
- [5] I. A. Shanks. The physics and display applications of liquid crystals. *Contemporary Physics*, 23(1):65–91, 1982.
- [6] M. Schadt. The twisted nematic effect: Liquid crystal displays and liquid crystal materials. *Molecular Crystals and Liquid Crystals*, 165:405–438, 1988.
- [7] Pochi Yeh and Claire Gu. *Optics of liquid crystal displays*, volume 67. John Wiley & Sons, 2009.
- [8] CH Gooch and HA Tarry. The optical properties of twisted nematic liquid crystal structures with twist angles 90 degrees. *Journal of Physics D: Applied Physics*, 8(13):1575, 1975.
- [9] H. L. Ong. Optical properties of general twisted nematic liquid-crystal displays. *Applied Physics Letters*, 51(18):1398–1400, 1987.

- [10] L. Marrucci, E. Karimi, S. Slussarenko, B. Piccirillo, E. Santamato, E. Nagali, and F. Sciarrino. Spin-to-orbital conversion of the angular momentum of light and its classical and quantum applications. *Journal of Optics*, 13:064001, 2011.
- [11] L. Yan, P. Gregg, E. Karimi, A. Rubano, L. Marrucci, R. W. Boyd, and S. Ramachandran. Q-plate enabled spectrally diverse orbital-angular-momentum conversion for stimulated emission depletion microscopy. *Optica*, 2:900–903, 2015.
- [12] V. D’Ambrosio, N. Spagnolo, L. Del Re, S. Slussarenko, Y. Li, L. C. Kwek, L. Marrucci, S. P. Walborn, L. Aolita, and F. Sciarrino. Photonic polarization gears for ultra-sensitive angular measurements. *Nature Communications*, 4(2432):1–8, 2013.
- [13] E. Karimi, L. Marrucci, C. de Lisio, and E. Santamato. Time-division multiplexing of the orbital angular momentum of light. *Optics Letters*, 37:127–129, 2012.
- [14] A. Sit, F. Bouchard, R. Fickler, J. Gagnon-Bischoff, H. Larocque, K. Heshami, D. Elser, C. Peuntinger, K. Günther, B. Heim, C. Marquardt, G. Leuchs, R. W. Boyd, and Karimi E. High-dimensional intracity quantum cryptography with structured photons. *Optica*, 4(9):1006, 2017.
- [15] F. Cardano, F. Massa, H. Qassim, E. Karimi, S. Slussarenko, D. Paparo, C. de Lisio, F. Sciarrino, E. Santamato, R. W. Boyd, and L. Marrucci. Quantum walks and wavepacket dynamics on a lattice with twisted photons. *Science Advances*, 1:e150087, 2015.
- [16] M. Stalder and M. Schadt. Linearly polarized light with axial symmetry generated by liquid-crystal polarization converters. *Optics Letters*, 21(23):1948–1950, 1996.
- [17] F. Cardano, E. Karimi, S. Slussarenko, L. Marrucci, C. de Lisio, and E. Santamato. Polarization pattern of vector vortex beams generated by q -plates with different topological charges. *Applied Optics*, 51(10):C1–C6, 2012.
- [18] I. Nys, B. Berteloot, and K. Neyts. Photoaligned liquid crystal devices with switchable hexagonal diffraction patterns. *Materials*, 15(7):2453–2465, 2022.
- [19] A. E. Siegman. *Lasers*. Mill Valley. Calif.: University Science Books, 1986.
- [20] L. Allen, M. W. Beijersbergen, R. J. C. Spreeuw, and J. P. Woerdman. Orbital angular momentum of light and the transformation of laguerre–gaussian laser modes. *Physical Review A*, 45(11):8185–8189, 1992.

- [21] D. Cozzolino, B. Da Lio, D. Bacco, and L. K. Oxenløwe. High-dimensional quantum communication: benefits, progress, and future challenges. *Advanced Quantum Technologies*, 2:1900038, 2019.
- [22] S. W. Hell and J. Wichmann. Breaking the diffraction resolution limit by stimulated emission: stimulated-depletion fluorescence microscopy. *Optics Letters*, 19(11):708–782, 1994.
- [23] G. Foo, D. M. Palacios, and G. A. Swartzlander. Optical vortex coronagraph. *Optics Letters*, 20(24):3308–3310, 2005.
- [24] M. W. Beijersbergen, Coerwinkel R. P. C., M. Kristensen, and J. P. Woerdman. Helical-wavefront laser beams produced with a spiral phaseplate. *Optics Communications*, 112:321–327, 1994.
- [25] M. W. Beijersbergen, L. Allen, H. E. L. O. van der Veen, and J. P. Woerdman. Astigmatic laser mode converters and transfer of orbital angular momentum. *Optics Communications*, 96:123–132, 1993.
- [26] E. Bolduc, N. Bent, E. Santamato, E. Karimi, and R. W. Boyd. Exact solution to simultaneous intensity and phase encryption with a single phase-only hologram. *Optics Letters*, 38(18):3546–3549, 2013.
- [27] H Larocque, J Gagnon-Bischoff, F Bouchard, R Fickler, J Upham, R W Boyd, and E Karimi. Arbitrary optical wavefront shaping via spin-to-orbit coupling. *Journal of Optics*, 18(12):124002, 2016.
- [28] B. Saleh and M. Teich. *Fundamentals of Photonics*. New York: Wiley, 2013.
- [29] A. Sit, L. Giner, E. Karimi, and J. S. Lundeen. General lossless spatial polarization transformations. *Journal of Optics*, 19:094003, 2017.
- [30] M. Born and E. Wolf. *Principles of Optics: Electromagnetic Theory of Propagation, Interference and Diffraction of Light*. Amsterdam: Elsevier, 1980.
- [31] H. Larocque, D. Sugic, D. Mortimer, A. J. Taylor, R. Fickler, R. W. Boyd, M. R. Dennis, and E. Karimi. Reconstructing the topology of optical polarization knots. *Nature Physics*, 14:1079–1082, 2018.
- [32] T. J. Sluckin, D. A. Dunmur, and H. Stegemeyer. *Crystals That Flow: Classic Papers from the History of Liquid Crystals*. London: Taylor Francis, 2004.

- [33] F. Reinitzer. Beiträge zur kenntiss des cholesterins. *Monatshfte für Chemie (Wein)*, 9:421–441, 1888.
- [34] O Lehmann. *Flüssigge Kristalle*. Leipzig: Wilhem Engelmann, 1904.
- [35] E. Bose. Zur theorie der anisotropen flüssigkeiten. *Physikalische Zeitschrift*, 9:708–713, 1908.
- [36] G. H. Brown and W. G. Shaw. The mesomorphic state: liquid crystals. *Chemical Reviews*, 57:1049–1157, 1957.
- [37] R. Williams. Domains in liquid crystals. *The Journal of Chemical Physics*, 39:384–388, 1963.
- [38] G. Heilmeyer. Liquid-crystal display devices. *Scientific Americacn*, 222(4):100–107, 1970.
- [39] P. Pieranski. Pierre-Gilles de Gennes: Beautiful and mysterious liquid crystals. *Comptes Rendus Physique*, 20:756–769, 2019.
- [40] C. L. Khetrapal and A. C. Kunwar. Nmr spectroscopy of molecules oriented in liquid crystalline solvents. *Advances in Liquid Crystals*, 6:173–242, 1983.
- [41] H. Yoshida, S. Kobinata, and S. Maeda. A study of orientational characteristics of nematics by means of polarized fluorecence. *Molecular Crystals and Liquid Crystals*, 131:209–216, 1985.
- [42] H. Yoshida, Y. Nakajima, S. Kobinata, and S. Maeda. Determination of the order parameters in liquid crystal by resonance raman method; 5cb as probed by β -carotene. *Journal of the Physical Society of Japan*, 50:3525–3528, 1981.
- [43] P. Chingduang, S. Bualek, O. Phaovibul, and B. Schrader. Study of orientation and order of non-mesogenic solutes in liquid crystalline matrix by infrared spectroscopy. *Molecular Crystals and Liquid Crystals*, 132:131–141, 1986.
- [44] A. Yariv and P. Yeh. *Optical Waves in Crystals: Propagation and Control of Laser Radiation*. New York: John Wiley Sons, 1984.
- [45] E. Bomzon, G. Biener, V. Kleiner, and E. Hasman. Space-variant pancharatnam–berry phase optical elements with computer-generated subwavelength gratings. *Optics Letters*, 27:1141–1143, 2002.

- [46] E. Karimi, S. A. Schulz, I. De Leon, H. Qassim, J. Upham, and R. W. Boyd. Generating optical orbital angular momentum at visible wavelengths using a plasmonic metasurface. *Light: Science Applications*, 3:e167, 2014.
- [47] L. Marrucci, C. Manzo, and D. Paparo. Optical spin-to-orbit angular momentum conversion in inhomogeneous anisotropic media. *Physical Review Letters*, 96:163905, 2006.
- [48] L. Marrucci, C. Manzo, and D. Paparo. Pancharatnam-berry phase optical elements for wavefront shaping in the visible domain: switchable helical modes generation. *Applied Physics Letters*, 88:221102, 2006.
- [49] S. Pancharatnam. Generalized theory of interference and its applications. *Proceedings of the Indian Academy of Sciences-Section A*, 44:398–417, 1956.
- [50] M. V. Berry. Quantal phase factors accompanying adiabatic changes. *Proceedings of the Royal Society of London A: Mathematical, Physical and Engineering Sciences*, 392:45–57, 1984.
- [51] E. Cohen, H. Larocque, F. Bouchard, F. Nejdassattari, Y Gefen, and E. Karimi. Geometric phase from aharonov—bohm to pancharatnam—berry and beyond. *Nature Reviews Physics*, 1:437–449, 2019.
- [52] A. Rubano, F. Cardano, B. Piccirillo, and L. Marrucci. Q-plate technology: a progress review [invited]. *Journal of the Optical Society of America B*, 36(5):70–87, 2019.
- [53] F. Bouchard, I. De Leon, S. A. Schulz, J. Upham, E. Karimi, and R. W. Boyd. Optical spin-to-orbital angular momentum conversion in ultra-thin metasurfaces with arbitrary topological charges. *Applied Physics Letters*, 105:101905, 2014.
- [54] B. Piccirillo, V. Kumar, L. Marrucci, and E. Santamato. Pancharatnam—berry phase optical phase optical elements for generation and control of complex light: generalized superelliptical q-plates. *Proceedings of SPIE*, 9379:937907, 2015.
- [55] E. Karimi, B. Piccirillo, L. Marrucci, and E. Santamati. Light propagation in a birefringent plate with topological charge. *Optics Letters*, 34:1225–1227, 2009.
- [56] C. Mauguin. Sur les cristaux liquides de lehmann. *Bulletin de la société française de minéralogie*, 34:71–117, 1911.
- [57] E. B. Priestley, P. J. Wojtowicz, and P. Sheng. *Introduction to Liquid Crystals*. New York: Plenum Press, 1975.

- [58] H. J. Deuling. Deformation pattern of twisted liquid crystal layers in an electric field. *Molecular Crystals and Liquid Crystals*, 27:81–93, 1993.
- [59] T. W. Preist, K. R. Welford, and J. R. Sambles. Response of a twisted nematic liquid crystal to any applied voltage. *Liquid Crystals*, 4(2):103–116, 1989.
- [60] E. Nowinowski-Kruszelnicki, J. Kedzierski, Z. Raszewski, L. Jaroszewicz, M. A. Kojdecki, W. Piecek, P. Perkowski, M. Olifierczuk, E. Miszczyk, K. Ogrodnik, and P. Morawiak. Measurement of elastic constants of nematic liquid crystals with use of hybrid in-plane-switched cell. *Opto-electronics Review*, 20:255–259, 2012.
- [61] B. J. Frisken and P. Palffy-Muhoray. Freedericksz transitions in nematic liquid crystals: The effects of an in-plane electric field. *Physical Review A*, 40(10):532–546, 1989.
- [62] V. Fréedericksz and A. Repiewa. Theoretisches und experimentelles zur frage nach der natur der anisotropen flüssigkeiten. *Zeitschrift für Physik*, 42:532–546, 1927.
- [63] H. J. Deuling. Deformation of nematic liquid crystals in an electric field. *Molecular Crystals and Liquid Crystals*, 19:123–131, 1972.
- [64] J. H. Holland. *Adaptation in Natural and Artificial Systems: An Introductory Analysis with Applications to Biology, Control and Artificial Intelligence*. Cambridge: MIT Press, 1992.
- [65] S. Katoch, S. S. Chauhan, and V. Kumar. A review on genetic algorithm: past, present, and future. *Multimedia Tools and Applications*, 80:8091, 2021.
- [66] L. D. Chambers. *The practical handbook of genetic algorithms: applications*. New York: Chapman and Hall/CRC, 2000.
- [67] X. Yao. An empirical study of genetic operators in genetic algorithms. *Microprocessing and Microprogramming*, 38:707, 1993.
- [68] M. Iri, S. Moriguti, and Y. Takasawa. On a certain quadrature formula. *RIMS Kokyuroku Kyoto University*, 91:82–118, 1970.
- [69] P. Davis and P. Rabinowitz. *Methods of Numerical Integration*. San Diego: Academic Press, 2014.
- [70] D. E. Goldberg and K. A. Deb. A comparative analysis of selection schemes used in genetic algorithms. *Foundations of Genetic Algorithms*, 1:69–93, 1991.

- [71] L. J. Eshelman and J. D. Schaffer. Real-coded genetic algorithms and interval-schemata. *Foundations of Genetic Algorithms*, 2:187–202, 1993.
- [72] O. Kramer. *Genetic Algorithm Essentials*. Springer, 2017.
- [73] S. Heron. Advanced encryption standard (aes). *Network Security*, 2009(12):8–12, 2009.
- [74] R. L. Rivest, A. Shamir, and L. Adleman. A method for obtaining digital signatures and public-key cryptosystems. *Communications of the ACM*, 21(2):120–126, 1978.
- [75] N. Gisin, G. Ribordy, W. Tittel, and H. Zbinden. Quantum cryptography. *Reviews of Modern Physics*, 74:145–195, 2002.
- [76] S. Pirandola, U. L. Andersen, L. Banchi, M. Berta, D. Bunandar, R. Colbeck, D. Englund, T. Gehring, C. Lupo, C. Ottaviani, J. L. Pereira, M. Razavi, J. Shamsul Shaari, M. Tomamichel, V. C. Usenko, G. Vallone, P. Villoresi, and P. Wallden. Advances in quantum cryptography. *Advances in Optics and Photonics*, 12(4):1012–1236, 2020.
- [77] C. H. Bennett and G. Brassard. Quantum cryptography: Public key distribution and coin tossing. *Proceedings of the IEEE International Conference on Computers, Systems, and Signal Processing, Bangalore, India*, 175:8, 1984.
- [78] L. Sherida and V. Scarani. Security proof for quantum key distribution using qudit systems. *Physical Review A*, 82:030301(R), 2010.
- [79] I. Eames and J. B. Flor. New developments in understanding interfacial processes in turbulent flows. *Philosophical Transactions of the Royal Society A*, 369:702–705, 2011.
- [80] A. Marshak and A. Davis. *3D Radiative Transfer in Cloudy Atmospheres*. New York: Springer, 2005.
- [81] E. S. Menon. *Transmission Pipeline Calculations and Simulations Manual*. Gulf Professional Publishing, 2015.
- [82] L. F. Richardson. *Weather prediction by numerical process*. Cambridge University Press, 1922.
- [83] A. Kolmogorov. The local structure of turbulence in incompressible viscous fluid for very large reynolds’ numbers. *Doklady Akademiia Nauk SSSR*, 30:301, 1941.

- [84] R. T. Cerbus, C.-c. Lui, G. Gioia, and P. Chakraborty. Small-scale universality in the spectral structure of transitional pipe flows. *Science Advances*, 6:eaaw6256, 2020.
- [85] S. A. Orszag. Analytical theories of turbulence. *Journal of Fluid Mechanics*, 41:363–386, 1970.
- [86] Y. Zhou. Turbulence theories and statistical closure approaches. *Physics Reports*, 935:1–117, 2022.
- [87] L. C. Andrews and R. L. Phillips. *Laser beam propagation through random media*. SPIE Press, 2005.
- [88] O. Korotkova, N. Farwell, and E. Shchepakina. Light scintillation in oceanic turbulence. *Waves in Random and Complex Media*, 22(2):260–266, 2012.
- [89] I. Toselli and S. Gladysz. On the general equivalence of the fried parameter and coherence radius for non-kolmogorov and oceanic turbulence. *OSA Continuum*, 2(1):43–48, 2019.
- [90] Y. Baykal. Expressing oceanic turbulence parameters by atmospheric turbulence structure constant. *Applied Optics*, 55(6):1228–1231, 2016.
- [91] F. Bouchard, A. Sit, F. Hufnagel, A. Abbas, Y. Zhang, R. Fickler, C. Marquardt, G. Leuchs, R. W. Boyd, and E. Karimi. Quantum cryptography with twisted photons through an outdoor underwater channel. *Optics Express*, 26(17):22563, 2018.
- [92] Yuan Chen, Wei-Guan Shen, Zhan-Ming Li, Cheng-Qiu Hu, Zeng-Quan Yan, Zhi-Qiang Jiao, Jun Gao, Ming-Ming Cao, Ke Sun, and Xian-Min Jin. Underwater transmission of high-dimensional twisted photons over 55 meters. *Photonix*, 1(1):1–11, 2020.
- [93] R. J. Noll. Zernike polynomials and atmospheric turbulence. *Journal of the Optical Society of America*, 66(3):207–211, 1976.
- [94] Ebrahim Karimi, Bruno Piccirillo, Eleonora Nagali, Lorenzo Marrucci, and Enrico Santamato. Efficient generation and sorting of orbital angular momentum eigenmodes of light by thermally tuned q-plates. *Applied Physics Letters*, 94(23), 2009.
- [95] L. D. Landau and E. M. Lifshitz. *Theory of elasticity*. London: Pergamon Press, 1959.

APPENDICES

Appendix A

Experimental Data

Here, I list the calculated Stokes parameters and uncertainties for the experimental data presented in Sec. 3.4. The Stokes parameters are taken as the average values over 101×101 pixels in each slice of the fabricated DP(0,1/2). The 16 slices represent twist angles from $\alpha = (-90^\circ, 90^\circ)$. The uncertainties for each slice are calculated as the standard deviations of the Stokes parameters, calculated as,

$$\Delta s_i = \sqrt{\frac{\sum_{j=1}^N (s_{ij} - \bar{s}_i)^2}{N - 1}}, \quad (\text{A.1})$$

where $i = 1, 2, 3$, $N = 10201$ is the sample size, s_{ij} is the i^{th} Stokes parameter of the j^{th} sample, and \bar{s}_i is the average value of the i^{th} Stokes parameter.

Table A.1: Average output Stokes parameters and uncertainties for H input on DP(0,1/2).

α ($^\circ$)	s_1	$\pm\Delta s_1$	s_2	$\pm\Delta s_2$	s_3	$\pm\Delta s_3$
-90	-0.94	0.05	0.03	0.4	0.0	0.3
-78.75	-0.88	0.03	-0.38	0.09	-0.01	0.09
-67.5	-0.67	0.07	-0.7	0.1	0.0	0.1
-56.25	-0.38	0.09	-0.9	0.1	0.0	0.1
-45	-0.02	0.09	-1.0	0.2	-0.05	0.09
-33.75	0.37	0.09	-1.0	0.1	-0.1	0.1
-22.5	0.69	0.07	-0.8	0.1	-0.1	0.1
-11.25	0.89	0.04	-0.5	0.1	0.0	0.1
0	0.96	0.02	-0.1	0.1	-0.09	0.09
11.25	0.89	0.03	0.25	0.08	-0.08	0.07
22.5	0.72	0.04	0.56	0.08	-0.08	0.07
33.75	0.41	0.06	0.8	0.1	-0.07	0.07
45	0.06	0.07	0.9	0.1	-0.07	0.07
56.25	-0.31	0.09	0.9	0.1	-0.07	0.07
67.5	-0.60	0.05	0.7	0.1	-0.07	0.06
78.75	-0.82	0.04	0.5	0.1	-0.09	0.08

Table A.2: Average output Stokes parameters and uncertainties for V input on DP(0,1/2).

α ($^\circ$)	s_1	$\pm\Delta s_1$	s_2	$\pm\Delta s_2$	s_3	$\pm\Delta s_3$
-90	0.93	0.06	0.0	0.3	0.0	0.1
-78.75	0.82	0.04	0.36	0.09	0.0	0.1
-67.5	0.61	0.07	0.6	0.1	0.0	0.1
-56.25	0.3	0.1	0.8	0.1	0.0	0.1
-45	0.0	0.1	0.9	0.2	0.0	0.1
-33.75	-0.35	0.09	0.8	0.1	0.0	0.1
-22.5	-0.63	0.07	0.7	0.1	0.1	0.1
-11.25	-0.83	0.06	0.4	0.1	0.1	0.1
0	-0.94	0.03	0.1	0.1	0.1	0.1
11.25	-0.91	0.03	-0.26	0.08	0.11	0.08
22.5	-0.73	0.05	-0.57	0.08	0.15	0.09
33.75	-0.43	0.07	-0.81	0.09	0.17	0.08
45	-0.05	0.06	-0.94	0.09	0.19	0.07
56.25	0.33	0.09	-0.9	0.1	0.18	0.07
67.5	0.64	0.05	-0.73	0.09	0.16	0.07
78.75	0.84	0.04	-0.45	0.09	0.13	0.09

Table A.3: Average output Stokes parameters and uncertainties for A input on DP(0,1/2).

α ($^\circ$)	s_1	$\pm\Delta s_1$	s_2	$\pm\Delta s_2$	s_3	$\pm\Delta s_3$
-90	0.08	0.07	0.2	0.4	-1.0	0.4
-78.75	-0.03	0.08	0.15	0.08	-1.0	0.1
-67.5	-0.08	0.07	0.13	0.10	-0.9	0.1
-56.25	-0.15	0.07	0.10	0.07	-0.9	0.1
-45	-0.10	0.07	-0.06	0.08	-1.0	0.1
-33.75	-0.02	0.08	-0.12	0.07	-1.0	0.1
-22.5	0.06	0.08	-0.1	0.1	-1.0	0.1
-11.25	0.10	0.07	-0.10	0.09	-1.0	0.1
0	0.12	0.07	-0.09	0.09	-0.98	0.09
11.25	0.06	0.07	-0.05	0.06	-0.98	0.08
22.5	0.06	0.06	-0.07	0.06	-0.98	0.09
33.75	0.07	0.07	-0.03	0.08	-1.0	0.1
45	0.05	0.07	-0.03	0.08	-1.0	0.1
56.25	0.02	0.07	-0.02	0.09	-1.0	0.1
67.5	0.00	0.06	-0.07	0.08	-0.96	0.09
78.75	0.12	0.08	0.14	0.08	-0.9	0.1

Table A.4: Average output Stokes parameters and uncertainties for D input on DP(0,1/2).

α ($^\circ$)	s_1	$\pm\Delta s_1$	s_2	$\pm\Delta s_2$	s_3	$\pm\Delta s_3$
-90	0.0	0.1	-0.1	0.2	1.0	0.4
-78.75	0.00	0.08	-0.09	0.07	0.9	0.1
-67.5	0.06	0.07	-0.08	0.08	0.9	0.1
-56.25	0.13	0.06	-0.05	0.07	0.9	0.1
-45	0.07	0.08	-0.07	0.07	0.9	0.1
-33.75	0.06	0.08	-0.06	0.07	0.9	0.1
-22.5	0.04	0.09	-0.06	0.09	0.9	0.1
-11.25	0.09	0.07	-0.01	0.07	0.9	0.1
0	0.08	0.07	0.03	0.08	0.9	0.1
11.25	0.00	0.07	0.05	0.06	0.93	0.09
22.5	-0.06	0.07	0.07	0.06	0.92	0.09
33.75	-0.06	0.08	0.09	0.07	0.9	0.1
45	-0.06	0.07	0.07	0.06	0.9	0.1
56.25	-0.06	0.07	0.14	0.08	0.9	0.1
67.5	-0.05	0.07	0.15	0.07	0.9	0.1
78.75	-0.20	0.07	-0.02	0.07	0.9	0.1

Table A.5: Average output Stokes parameters and uncertainties for R input on DP(0,1/2).

α ($^\circ$)	s_1	$\pm\Delta s_1$	s_2	$\pm\Delta s_2$	s_3	$\pm\Delta s_3$
-90	0.0	0.2	0.9	0.6	0.2	0.2
-78.75	-0.33	0.08	0.8	0.1	0.15	0.09
-67.5	-0.60	0.07	0.6	0.2	0.21	0.09
-56.25	-0.81	0.06	0.4	0.1	0.3	0.1
-45	-0.93	0.02	0.0	0.1	0.2	0.1
-33.75	-0.89	0.04	-0.4	0.1	0.2	0.1
-22.5	-0.71	0.07	-0.6	0.1	0.1	0.1
-11.25	-0.4	0.1	-0.9	0.1	0.1	0.1
0	0.0	0.1	-1.0	0.1	0.1	0.1
11.25	0.29	0.08	-0.94	0.09	0.08	0.08
22.5	0.59	0.06	-0.76	0.09	0.12	0.08
33.75	0.84	0.03	-0.45	0.08	0.07	0.09
45	0.94	0.03	-0.10	0.07	0.05	0.08
56.25	0.87	0.04	0.3	0.1	0.03	0.08
67.5	0.70	0.05	0.58	0.09	-0.04	0.07
78.75	0.37	0.08	0.8	0.1	0.14	0.09

Table A.6: Average output Stokes parameters and uncertainties for L input on DP(0,1/2).

α ($^\circ$)	s_1	$\pm\Delta s_1$	s_2	$\pm\Delta s_2$	s_3	$\pm\Delta s_3$
-90	0.0	0.1	-1.0	0.6	-0.2	0.2
-78.75	0.33	0.09	-1.0	0.1	-0.2	0.1
-67.5	0.63	0.08	-0.8	0.1	-0.3	0.1
-56.25	0.84	0.04	-0.5	0.1	-0.3	0.1
-45	0.93	0.02	-0.2	0.1	-0.3	0.1
-33.75	0.91	0.03	0.2	0.1	-0.2	0.1
-22.5	0.75	0.07	0.5	0.1	-0.2	0.1
-11.25	0.51	0.09	0.8	0.1	-0.2	0.1
0	0.2	0.1	0.9	0.1	-0.21	0.08
11.25	-0.20	0.08	0.9	0.1	-0.20	0.07
22.5	-0.52	0.06	0.8	0.1	-0.20	0.07
33.75	-0.79	0.04	0.5	0.1	-0.13	0.08
45	-0.93	0.03	0.20	0.08	-0.09	0.07
56.25	-0.92	0.03	-0.2	0.1	-0.08	0.07
67.5	-0.78	0.04	-0.53	0.08	-0.02	0.07
78.75	-0.51	0.07	-0.8	0.1	-0.2	0.1

Appendix B

Elastic continuum theory

B.1 Derivation of free-energy density distortion terms

This derivation follows that which is presented in [4]. Let $\mathbf{n}(\mathbf{r})$ describe the nematic director distribution, subject to the assumptions listed in Sec. 4.1.1, repeated here for convenience:

1. Since we are expanding around $\partial_i n_j = 0$, the lowest-order non-vanishing terms are quadratic, i.e., of the form $(\partial_i n_j) \cdot (\partial_i n_j)$.
2. The “head” and “tail” of the nematic director represent the same physical state; therefore, F_D should be even in n_j .
3. \mathcal{F}_D should be a scalar quantity by nature of it being energy.
4. We may discard any $\nabla \cdot \mathbf{u}(\mathbf{r})$, where $\mathbf{u}(\mathbf{r})$ is an arbitrary vector field, since they are surface contributions to f_D . These are assumed small by Gauss’ Theorem.

Consider its spatial derivative $\partial_i n_j$, which forms a rank two tensor. This tensor can be separated into a symmetric part,

$$s_{ij} = (\partial_i n_j + \partial_j n_i)/2, \tag{B.1}$$

and an anti-symmetric part,

$$(\nabla \times \mathbf{n}(\mathbf{r}))_k = \epsilon_{ijk} \partial_i n_j, \tag{B.2}$$

where ϵ_{ijk} is the Levi-Civita symbol. There are typically six independent components to s_{ij} , but this is further restricted by recalled that $\mathbf{n}(\mathbf{r})$ is a unit vector. If we allow the z -axis to be parallel to the local $\mathbf{n}(\mathbf{r})$ direction, then all gradients of n_z will vanish since,

$$0 = \nabla(n_x^2 + n_y^2 + n_z^2) = 2n_z \nabla n_z + 0 = 2\nabla n_z \implies \partial_i n_z = 0. \quad (\text{B.3})$$

Thus, we have that,

$$\begin{aligned} s_{zx} &= (\nabla \times \mathbf{n}(\mathbf{r}))_y / 2, \\ s_{zy} &= -(\nabla \times \mathbf{n}(\mathbf{r}))_x / 2, \\ s_{zz} &= 0. \end{aligned} \quad (\text{B.4})$$

The divergence is then $\nabla \cdot \mathbf{n}(\mathbf{r}) = \partial_i n_i = s_{ii} = s_{xx} + s_{yy}$. Since \mathcal{F}_D is quadratic in the derivatives of $\mathbf{n}(\mathbf{r})$, it is convenient to separate it as $\mathcal{F}_D = \mathcal{F}_s + \mathcal{F}_c + \mathcal{F}_{sc}$, where each term is quadratic in s_{ij} , $\nabla \times \mathbf{n}(\mathbf{r})$, and the crossterms, respectively.

Nematic liquid crystals exhibit C_∞ symmetry around the z -axis. Therefore, determining the number of independent terms of \mathcal{F}_s is allegedly equivalent to finding the number of elastic constants for a medium of such a symmetry, here equivalent to C_6 hexagonal crystals [95]. This gives the general form of \mathcal{F}_s to be,

$$\mathcal{F}_s = \lambda_1 s_{zz}^2 + \lambda_2 (s_{xx} + s_{yy})^2 + \lambda_3 s_{ij} s_{ij} + \lambda_4 s_{zz} (s_{xx} + s_{yy}) + \lambda_5 (s_{xz}^2 + s_{yz}^2), \quad (\text{B.5})$$

where λ_i are arbitrary constants, and summation is performed over like indices. By Eq. (B.4) and the full formulation of $s_{ij} s_{ij}$, this reduces to,

$$\mathcal{F}_s = \lambda_2 (\nabla \cdot \mathbf{n})^2 + \lambda_3 [(\nabla \cdot \mathbf{n})^2 + \cancel{\partial_i (n_j \partial_j n_i)} - \cancel{\partial_j (n_j \partial_i n_i)} + (\nabla \times \mathbf{n})^2 / 2] + \lambda_5 (\mathbf{n} \times \nabla \times \mathbf{n})^2 / 4. \quad (\text{B.6})$$

The third and fourth terms are dropped by assumption (4). Of course, $(\nabla \times \mathbf{n})^2 \equiv (\mathbf{n} \cdot \nabla \times \mathbf{n})^2 + (\mathbf{n} \times \nabla \times \mathbf{n})^2$. So overall, \mathcal{F}_s is the sum of three contributions: $(\nabla \cdot \mathbf{n})^2$, $(\mathbf{n} \cdot \nabla \times \mathbf{n})^2$, and $(\mathbf{n} \times \nabla \times \mathbf{n})^2$.

For \mathcal{F}_c and \mathcal{F}_{sc} , again according to the C_∞ symmetry,

$$\begin{aligned} \mathcal{F}_c &= \mu_1 (\nabla \times \mathbf{n})_z^2 + \mu_2 [(\nabla \times \mathbf{n})_x^2 + (\nabla \times \mathbf{n})_y^2] = \mu_1 (\mathbf{n} \cdot \nabla \times \mathbf{n})^2 + \mu_2 (\mathbf{n} \times \nabla \times \mathbf{n})^2, \\ \mathcal{F}_{sc} &= \nu (\mathbf{n} \times \nabla \times \mathbf{n})^2. \end{aligned} \quad (\text{B.7})$$

Across all three terms \mathcal{F}_s , \mathcal{F}_c , \mathcal{F}_{sc} , we only have the three contributions: $(\nabla \cdot \mathbf{n})^2$, $(\mathbf{n} \cdot \nabla \times \mathbf{n})^2$, and $(\mathbf{n} \times \nabla \times \mathbf{n})^2$. We are then free to regroup everything and absorb the various constants into the three elastic constants K_1, K_2, K_3 to get our fundamental distortion free-energy equation:

$$\mathcal{F}_D = \frac{1}{2} \{ K_1 (\nabla \cdot \mathbf{n})^2 + K_2 (\mathbf{n} \cdot \nabla \times \mathbf{n})^2 + K_3 (\mathbf{n} \times \nabla \times \mathbf{n})^3 \}. \quad (\text{B.8})$$